STABLE ISOTOPE SIGNATURES OF DIAGENESIS:

NATURAL AND EXPERIMENTAL STUDIES

By

Anthony Douglas Pollington

A dissertation submitted in partial fulfillment of the requirements for the degree of

Doctor of Philosophy

(Geoscience)

at the

UNIVERSITY OF WISCONSIN-MADISON

2013

Date of final oral examination: 07/25/13

The dissertation is approved by the following members of the Final Oral Committee:

John W. Valley, Professor, Geoscience (primary advisor)

Philip E. Brown, Professor, Geoscience

Alan R. Carroll, Professor, Geoscience

Herbert F. Wang, Professor, Geophysics

Shanan E. Peters, Associate Professor, Geoscience

Reinhard Kozdon, Assistant Scientist, Geoscience

1	

Dedicated to Ellen, my family, and my scientific mentors

Table of Contents

Dedication	i
Acknowledgements	
Publication Reference	
Supplemental Material Description	
Dissertation Abstract	
Introduction	1
	_
CHAPTER 1	4
Evolution of quartz cementation during burial of the Cambrian Mount Sim- Illinois Basin: In situ microanalysis of δ ¹⁸ O	on Sandstone,
ABSTRACT	5
INTRODUCTION	
GEOLOGICAL BACKGROUND	
METHODS	
Sample Preparation and Characterization	7
Isotope Analysis	
RESULTS	
DISCUSSION	10
CONCLUSIONS	14
ACKNOWLEDGEMENTS	15
REFERENCES CITED	16
Figures	19
Appendix A1	
MT. SIMON DIAGENESIS	24
METHODS	
Sample preparation	
Analytical conditions	
Factors influencing $\delta^{18}O(OQ)$	
ADDITIONAL REFERENCES NOT CITED IN MAIN TEXT	
Appendix Figures	
Data repository (DR1)	30
Chapter 2	31
A previously unrecognized episode of low temperature feldspar diagenesis in	
Mount Simon and Eau Claire formations revealed by <i>in situ</i> microan	
Abstract	•
Abbreviations	
Introduction	
Geologic setting and Samples	
Clastic samples	36
Methods	
Sample preparation and imaging	39

	iii
Feldspar standards	39
Oxygen isotope measurements	40
Electron microprobe	
Results	
Textural relationships	42
Mineral chemistry	
Oxygen isotope ratios Discussion	44
	47
Paragenesis.	
Source of diagenetic components	
Diagenetic temperatures	50
Quartz-feldspar disequilibrium	
Continent-scale fluid flow	
Conclusions	
Acknowledgements	
References	57
Figures	62
Tables	80
Appendix A2	
Feldspar standards	81
Feldspar bias calculation	
Additional references not cited in main text	83
Appendix Figures	
Appendix Tables	
Data repository (DR2)	
······································	
Chapter 3	
Silicon isotope composition of diagenetic quartz: A record of Precambria	n weathering 93
Acknowledgements	
	102
REFERENCES CITED	
REFERENCES CITEDFigures	
REFERENCES CITEDFigures Appendix A3	105
REFERENCES CITED Figures Appendix A3 METHODS	105
REFERENCES CITED Figures Appendix A3 METHODS Appendix Figures	105 109 110
REFERENCES CITED Figures Appendix A3 METHODS Appendix Figures Appendix Table	
REFERENCES CITED Figures Appendix A3 METHODS Appendix Figures Appendix Table	
REFERENCES CITED Figures Appendix A3 METHODS Appendix Figures Appendix Table Data repository (DR3)	
REFERENCES CITED Figures Appendix A3 METHODS Appendix Figures Appendix Table Data repository (DR3) CHAPTER 4 Experimental calibration of silicon and oxygen isotope fractionation between water at 250°C: A new method using in situ microanalysis of experimental calibration of silicon and oxygen isotope fractionation between the silicon and oxygen isotope fractionation and oxygen isotop	
REFERENCES CITED Figures Appendix A3 METHODS Appendix Figures Appendix Table Data repository (DR3) CHAPTER 4 Experimental calibration of silicon and oxygen isotope fractionation between water at 250°C: A new method using in situ microanalysis of experimentals.	
REFERENCES CITED Figures Appendix A3 METHODS Appendix Figures Appendix Table Data repository (DR3) CHAPTER 4 Experimental calibration of silicon and oxygen isotope fractionation between water at 250°C: A new method using in situ microanalysis of experimental calibration of silicon and oxygen isotope fractionation between the silicon and oxygen isotope fractionation and oxygen isotop	
REFERENCES CITED Figures Appendix A3 METHODS Appendix Figures Appendix Table Data repository (DR3) CHAPTER 4 Experimental calibration of silicon and oxygen isotope fractionation between water at 250°C: A new method using in situ microanalysis of experimentals.	
REFERENCES CITED Figures Appendix A3 METHODS Appendix Figures Appendix Table Data repository (DR3) CHAPTER 4 Experimental calibration of silicon and oxygen isotope fractionation betw water at 250°C: A new method using in situ microanalysis of experimental calibration of silicon and oxygen isotope fractionation betw water at 250°C: A new method using in situ microanalysis of experimental calibration of silicon and oxygen isotope fractionation betw water at 250°C: A new method using in situ microanalysis of experimental calibration of silicon and oxygen isotope fractionation betw water at 250°C: A new method using in situ microanalysis of experimental calibration of silicon and oxygen isotope fractionation betw	

	iv
Experimental product characterization	123
Isotope analysis of solid material	
Isotope analysis of fluids	
δ ¹⁸ O analysis of fluids	125
δ ³⁰ Si analysis of fluids	
Results	
Experimental growth	126
Isotope values of solid material	
δ^{18} O values of quartz overgrowth and powders	127
δ ³⁰ Si values of quartz overgrowth	
Isotope values of fluids	
δ^{18} O values of fluids	129
δ ³⁰ Si values of fluids	
Discussion	
Quartz growth rates	129
Recrystallization of powders	
δ ¹⁸ O values of powders	131
δ ¹⁸ O values of starting and ending fluids	
Quartz-water fractionation	
$\alpha^{18}O(Qtz-H_2O)$ calibration	
α^{30} Si(Qtz-fluid) calibration	
Conclusion	
Acknowledgements	
References Cited	
Figures	
Tables	154
Appendix A4	
Water fluorination method	158
Appendix Figure	159
Data repository (DR4).	160
Sample index and UW catalog numbers	161
bumple mack and on caused numbers	101

Acknowledgments

I would like to thank my primary advisor John Valley for his support over the past four years and for introducing me to the world of stable isotopes. His excitement about my results has been extremely encouraging, particularly during times of my own uncertainty about my projects. The patience with which he has brought me along my steep learning curve regarding stable isotopes has allowed me to grow in skill and confidence about my abilities as an isotope geochemist.

The research staff of the WiscSIMS lab, Drs. Noriko Kita, Takayuki Ushikubo and especially Reinhard Kozdon, have made possible the state-of-the-art analyses presented in this dissertation. Without their expertise in alignment, tuning and instrumental setup, none of the conclusions I have made would have been possible. Other postdocs and scientists in the lab who have helped me with analyses are appreciated; Drs. Anne-Sophie Bouvier, Craig Grimes, Kouki Kitajima, Daisuke Nakashima, and Ariel Strickland assisted me in analyses or discussions.

Thanks are due to my committee at UW-Madison, Profs Phil Brown, Alan Carroll, Shanan Peters, Herb Wang and Dr. Reinhard Kozdon, who have encouraged my projects with their questions and excitement. I have been the recipient of a wealth of knowledge and experience from the administrative and technical staff in the department of Geoscience. In particular, Mike Spicuzza, Brian Hess and Jim Kern have been extremely helpful and gracious with their time.

I would like to thank the faculty, postdocs and students of Weeks Hall for their friendship and encouragement during my time here. Especially of note are my fellow WiscSIMS Ph.D. students of the past four years Chloë Bonamici and Ian Orland, my office mate for the majority

of my tenure. They were always willing to discuss my ideas, however harebrained they may have been, and provided a vast amount of support during the hard times as well as the easy ones.

Funding came from DOE (93ER14389), the UW-Madison Department of Geoscience, the Geological Society of America (GSA), and the Mineralogy, Geochemistry, Petrology and Volcanology division of GSA. Wisc-SIMS is partially funded by NSF (EAR-0319230, 0744079, 1053466).

Finally, I would like to thank my family who have shown me extraordinary patience and support not only during my Ph.D. work but also throughout my life. Without the inspiration of my parents' doctorates and their willingness to let me try my hand at a wholly different line of work early on, I doubt I would have arrived at the point I am now. My brother and sister have always shown me kindness and been there for me; it has been a joy to grow into adults with them. I want to close by thanking my wife Ellen for being completely understanding and supportive of all my ideas and idiosyncrasies. She has given me a wealth of support scientifically and emotionally.

Publication Reference

The first chapter of this dissertation has been published in the journal *Geology*. The other three chapters are planned for submission. The citation for the published article is

Pollington, A.D., Kozdon, R., and Valley, J.W., 2011, Evolution of quartz cementation during burial of the Cambrian Mount Simon Sandstone, Illinois Basin: *In situ* microanalysis of δ¹⁸O: Geology, v. 39, p. 1119-1122.

Supplemental Material Description

Each chapter has associated appendices that describe material not covered in the main text, as well as data repository files that are included with the online version of this dissertation. The appendix and data repository files are numbered sequentially with each chapter. For example, appendix A1 and figure A1.1 are appendices for chapter 1 and are included in the print version; Tables DR1.1 and DR1.2 are data tables for chapter 1 included in the online version of the dissertation.

Chapter 1

Appendix A1

Figure A1.1

Samples cast in epoxy.

Table DR1.1

Oxygen isotope composition of detrital and diagenetic quartz measured on the WiscSIMS ims-1280 ion microprobe using a 15 µm spot size.

Table DR1.2

Oxygen isotope composition of detrital and diagenetic quartz measured on the WiscSIMS ims-1280 ion microprobe using a 5 µm spot size.

Figure DR1.1

SEM images and δ^{18} O vs. distance plots for every overgrowth analyzed with 5 µm spots.

Chapter 2

Appendix A2

Figure A2.1

Backscattered electron image of feldspar standard epoxy mount (WI-STD-79).

Figure A2.2

Measured SIMS bias relative to UWQ-1 as a function of Kfs percent.

Figure A2.3

Depth vs. Ca content of Kfs from the Mt Simon and Eau Claire formations.

Figure A2.4

Histograms of $\delta^{18}O(OK)$ in each rock studied.

Table A2.1

Summary of composition of potential feldspar standards

Table A2.2

 δ^{18} O values of feldspar standards measured by laser fluorination

Table A2.3

Analytical conditions used for electron probe microanalyses

Table DR2.1

Major element composition of potential feldspar standards measured by electron microprobe.

Table DR2.2

Oxygen isotope data for standards and clastic samples measured on the WiscSIMS ims-1280 ion microprobe.

Table DR2.3

Major element composition of clastic samples measured by electron microprobe.

Chapter 3

Appendix A3

Figure A3.1

Photomicrographs of sample 09WI-17, outcrop set A.

Figure A3.2

Crossplot of $\delta^{18}O$ and $\delta^{30}Si$ for quartz of individual samples from the Mt Simon Sandstone.

Figure A3.3

Crossplot of Δ^{18} O(early OQ-late OQ) vs. Δ^{30} Si(early OQ-late OQ) for individual samples.

Table A3.1

Locations of samples used in this study.

Table DR3.1

Oxygen isotope composition of detrital and diagenetic quartz from outcrop samples measured on the WiscSIMS ims-1280 ion microprobe.

Table DR3.2

Silicon isotope composition of detrital and diagenetic quartz measured on the WiscSIMS ims-1280 ion microprobe.

Table DR3.3

Paired oxygen and silicon isotope measurements of detrital and diagenetic quartz measured on the WiscSIMS ims-1280 ion microprobe.

Chapter 4

Appendix A4

Figure A4.1

Schematic diagram of water fluorination apparatus.

Table DR4.1

Oxygen isotope data for experimentally grown quartz measured on the WiscSIMS ims-1280 ion microprobe.

Table DR4.2

Silicon isotope data for experimentally grown quartz measured on the WiscSIMS ims-1280 ion microprobe.

Sample index and UW catalog numbers

Dissertation Abstract

Diagenesis is a broad term that covers the many physical and chemical processes that affect the properties of the rocks in a sedimentary basin, which may be recorded in mineralogical, chemical and textural changes including the stable isotope ratios of the minerals that precipitate in the pore spaces of a formation. By their nature, these cements are small, leading to challenges in the isotopic analysis of diagenetic minerals. The advent of high-precision *in situ* stable isotope analysis by secondary ion mass spectrometry has allowed the study of diagenesis at a resolution previously unattainable.

The $\delta^{18}O$ of quartz overgrowths from the Cambrian Mt. Simon and Eau Claire formations in the Illinois Basin cover a range from 17.5 to 28.5% VSMOW. Multiple analyses within single overgrowths show that individual overgrowths are consistently zoned throughout the formations with high values closest to detrital grains and lower values near the outer edge of the overgrowths. The consistent changes in $\delta^{18}O$ are interpreted to reflect quartz growth that began at relatively cool temperatures (~45°C) and continued during burial to temperatures as high as 110°C. Overgrowths of K-feldspar from the same samples have consistently lower $\delta^{18}O$ values than quartz overgrowths and are texturally constrained to have precipitated before the majority of the quartz. These results show that K-feldspar precipitation in these formations predates quartz precipitation and occurred at cooler temperatures (30-60°C).

Silicon isotope ratios (δ^{30} Si) of quartz overgrowths from deeply buried samples in the Illinois Basin and most outcrops from the Wisconsin Dome are close to 0% NBS-28, similar to detrital grains. However, in multiple samples from an outcrop in Wisconsin, the δ^{30} Si values are as low as -5.4%. These extremely low values are interpreted to reflect precipitation from silicon that was highly fractionated during chemical weathering of the Precambrian basement.

Quartz overgrowths 235 μm thick were experimentally precipitated in a silica-H₂O-NaOH-NaCl solution, at 250°C in 126 days to determine the silicon and oxygen isotope fractionation between quartz and fluid. At 250°C, Δ^{30} Si(Qtz-fluid)=0.55 \pm 0.10% and Δ^{18} O(Qtz-H₂O)=10.63 \pm 0.07%. This is the first experimentally determined silicon isotope fractionation value between quartz and fluid.

Introduction

Diagenesis is a broad term encompassing many processes that control the mechanical and reservoir properties of a sedimentary basin or formation. These processes range from chemical (e.g., mineral precipitation) to purely physical (e.g., compaction). Minerals that form during diagenesis can record chemical information about the temperature, time and chemical conditions at which they formed. In particular, the isotopic and trace element compositions of diagenetic minerals can be used to determine chemical and thermal conditions of formation as well as sources of material available for mineral growth. This dissertation consists of studies of diagenetic cements from Cambrian siliciclastic formations from the North American mid-continent as well as an experimental study to determine calibration factors for the isotope composition of quartz. These studies are made possible by the ability to measure isotope ratios with high spatial resolution and high precision using the secondary ion mass spectrometer in the WiscSIMS laboratory.

The dissertation is comprised of four chapters, written as manuscripts for journal publication. Each chapter is an independent study focusing on a separate topic, but all relating to the theme of isotopic studies of diagenesis. Chapter 1 has been published in the peer-reviewed journal *Geology* and chapters 2-4 are in various stages of preparation for submission to journals listed on each chapter's title page.

Chapter 1 describes high-resolution oxygen isotope compositions of quartz overgrowths from the Mt. Simon Sandstone in the Illinois Basin. These analyses revealed a basin-wide trend to decreasing oxygen isotope (δ^{18} O) values with progressively deeper burial in the basin. In

addition to the clear basin-wide trend observed, the high spatial resolution obtainable with the SIMS revealed systematic trends of decreasing $\delta^{18}O$ within individual overgrowths. These trends at the kilometer and micron scales are interpreted to reflect growth of quartz during increasing temperature due to burial.

Chapter 2 focuses on K-feldspar overgrowths from the Mt. Simon Sandstone and the overlying Eau Claire Formation. These cements are described both texturally and chemically in order to determine the chemical and thermal evolution of the formations. Based on textural observations, the K-feldspar cements precipitated relatively early in the basin history, prior to quartz cementation. The δ^{18} O of the K-feldspar cements is high, reflecting growth at relatively cool temperatures (20-60°C) and individual cements are not zoned, in contrast to the large zonation seen in quartz cements. Paired δ^{18} O analyses from adjacent quartz and K-feldspar cements are far from equilibrium values and show that these phases did not precipitate together. The analysis of multiple phases from the formations yields a more complete history of the formations than the study of just one diagenetic mineral.

Chapter 3 describes the first analyses of paired silicon isotope (δ^{30} Si) and oxygen isotope measurements from individual quartz overgrowths. The samples used in this study consist of the same Mt. Simon Sandstone samples measured in Chapter 1 for δ^{18} O, as well as samples of the Mt. Simon Sandstone from outcrops in central Wisconsin. The majority of overgrowths in this study have δ^{30} Si values similar to the igneous detrital grains nearby (\sim 0%), but one set of outcrops in Wisconsin has significantly fractionated δ^{30} Si and δ^{18} O values in the overgrowths. Overgrowths from this set of rocks have δ^{30} Si as low as -5.4%, as well as δ^{18} O \sim 20%. These δ^{30} Si values are among the lowest values measured for terrestrial rocks. The paired low δ^{30} Si

and $\delta^{18}O$ are interpreted to reflect growth from hydrothermal fluids dominated by silicon fractionated during weathering. These overgrowths potentially record a period of significant weathering of the Precambrian basement.

The final chapter focuses on an experimental calibration of the oxygen and silicon isotope fractionation between quartz and fluid. Previous efforts to calibrate oxygen isotope fractionation between quartz and water have relied on bulk analyses of fine powders, which may not have fully exchanged with the water isotopically during the experiment. This study describes a new method combining growth of quartz (as opposed to exchange) with *in situ* analyses of the experimentally precipitated quartz by SIMS rather than bulk analysis. This allows for confidence in the phase being analyzed and demonstrates this technique as useful for low-temperature experiments that may only produce small amounts of new material. In addition to the technique demonstration for oxygen isotopes, this is the first experimental study of silicon isotope fractionation between quartz and aqueous silicon. Previous estimates have been based on precipitated quartz. The value of silicon isotope fractionation between quartz and fluid measured in this experiment (Δ^{30} Si(Qtz-fluid) = +0.5‰) is distinctly different from all previous estimates (0 to -5‰).

CHAPTER 1

Evolution of quartz cementation during burial of the Cambrian Mount Simon Sandstone, $Illinois\ Basin:\ In\ situ\ microanalysis\ of\ \delta^{18}O$

Anthony D. Pollington, Reinhard Kozdon, and John W. Valley

WiscSIMS, Department of Geoscience, University of Wisconsin, Madison, Wisconsin 53706, USA

Pollington, A.D., Kozdon, R., and Valley, J.W., 2011, Evolution of quartz cementation during burial of the Cambrian Mount Simon Sandstone, Illinois Basin: *In situ* microanalysis of δ^{18} O: Geology, v. 39, p. 1119-1122.

ABSTRACT

The thermal, mechanical, and chemical evolution of a sedimentary basin exerts important controls on porosity and permeability of reservoir rocks. Oxygen isotope ratios of individual diagenetic cements record evidence of this history, but cannot be analyzed accurately by conventional techniques. Recent improvements for in situ analysis by ion microprobe provide high precision and accuracy at a scale of 5–10 μ m. In combination with cathodoluminescence imaging, in situ analysis of δ^{18} O(quartz) from the Cambrian Mount Simon Sandstone in the Illinois Basin (USA) reveals gradients within single overgrowths of as much as 7.7‰/50 μ m. While the inner portions of overgrowths remain approximately constant in δ^{18} O across the basin, the δ^{18} O of the rim becomes lower with depth. These data suggest that overgrowths formed during burial and heating, possibly with minimal changes in δ^{18} O of pore fluids. If δ^{18} O(H₂O) = -3‰, the highest temperature calculated for the rim of an overgrowth is 107°C at a paleodepth of 3.5 km. The variability both in average δ^{18} O of overgrowths and patterns from individual overgrowths corresponds with a geotherm of 30°C/km, and there is no evidence of quartz precipitation from higher temperature hydrothermal fluids.

INTRODUCTION

Diagenetic cements and compaction are the most important factors controlling porosity and permeability of a sedimentary rock. Thus, the compositions of diagenetic cements provide the opportunity to understand the thermal and fluid evolution of a basin. Stable isotope ratios preserve evidence of fluid/rock interactions, which can have a pronounced effect on the cementation of a rock. The oxygen isotope fractionation between quartz and water is large (~30% at 50 °C) and has been used to calculate temperatures of diagenesis and fluid compositions (e.g., Longstaffe and Ayalon, 1987; Hervig et al., 1995; Graham et al., 1996; Williams et al., 1997; Lyon et al., 2000; Macaulay et al., 2000; Marchand et al., 2002; Kelly et al. 2007; Harwood et al., 2009). If analyzed at an appropriate scale, the spatial and temporal distribution of isotopically distinct cements can be used to investigate whether the history of a basin was dominated by varying fluid composition or by burial heating, but most data have been measured at scales of millimeters to centimeters. Only one in situ study (Chen et al., 2001) of oxygen isotope ratios of diagenetic quartz and/or K-feldspar has investigated the fluid history of the Cambrian Mount Simon Sandstone (Illinois Basin, United States). Chen et al. (2001) made analyses of δ^{18} O in overgrowths from 11 samples of the Mount Simon Sandstone in and around the Illinois Basin using a 20 μ m spot size and precision of \pm 2‰ (2 standard deviations, SD); they detected a gradient in δ^{18} O from south to north over 700 km and concluded that individual overgrowths are homogeneous in δ^{18} O and that changing pore-fluid composition at constant temperature was responsible for the variability of overgrowth δ^{18} O from sample to sample. In this study we employ new instrumentation and procedures that yield significant improvements in accuracy, precision, and spot size (Kelly et al., 2007; Kita et al., 2009; Valley and Kita, 2009) and report gradients of δ^{18} O within single quartz overgrowths that could not be measured

previously. We evaluate the conclusions of Chen et al. (2001) and the competing hypothesis that the observed trends in δ^{18} O were caused by variable temperatures during burial.

GEOLOGICAL BACKGROUND

The Mount Simon Sandstone is the basal Cambrian sandstone in much of Illinois and Wisconsin (United States) and unconformably overlies the Precambrian basement except in paleotopographic highs (Templeton, 1951). The Mount Simon Sandstone is buried to a maximum depth of ~4250 m in southern Illinois (Fig. 1.1), ranges in thickness in the Illinois Basin from less than 91 m to 792 m (Hoholick et al., 1984), and crops out in central and western Wisconsin. Estimates based on vitrinite reflectance, fluid inclusion data and clay compaction suggest that the Illinois Basin was buried at most 1.2 km deeper than current depths (Altschaeffl and Harrison, 1959; Hoholick et al., 1984; Rowan et al., 2002).

The 19 samples in this study come from three cores in Illinois (Fig. 1.1) and were selected based on variation in depth (394–2581 m) and geographic distribution (430 km north-south). Most of the rocks are quartz arenites; some deep samples are subarkoses as K-feldspar content generally increases with depth. The dominant cements are quartz and K-feldspar overgrowths, with minor later cements (Hoholick et al., 1984). Evidence of detrital quartz pressure solution is observed in all rocks of this study regardless of depth.

METHODS

Sample Preparation and Characterization

Samples were cast in 25-mm-diameter epoxy rounds with the quartz standard UWQ-1 (Kelly et al., 2007), and imaged and analyzed at the University of Wisconsin-Madison (UW-

Madison) using a scanning electron microscope (SEM) with secondary electron (SE), backscattered electron (BSE), cathodoluminescence (CL), and energy dispersive spectrometry detectors, as well as optical microscopes. Overgrowth quartz cements (OQ) are commonly indistinguishable from the detrital quartz grains (DQ) by optical or SE microscopy, but are distinctly different by CL (Fig. 1.2). Areas for isotope analysis were selected based on size and abundance of overgrowths (see appendix A1).

Isotope Analysis

In situ oxygen isotope analyses were performed using a CAMECA IMS-1280 ion microprobe at WiscSIMS (Wisconsin Secondary Ion Mass-Spectrometer Laboratory), UW-Madison (Kita et al., 2009; Valley and Kita, 2009). Data were collected from spots ~15 μ m and ~5 μ m in diameter. During each session, four analyses of the UWQ-1 standard were made before and after each set of 10–15 sample measurements. Bracketing standards are used to calculate the instrumental bias in order to correct measured δ^{18} O values to the Vienna Standard Mean Ocean Water scale (Kita et al., 2009), as well as to evaluate the external reproducibility of the measurements. The spot-to-spot reproducibility or external precision of each set of bracketing standards averaged 0.26% (2SD) for 15 μ m spots and 0.66% (2SD) for 5 μ m spots. Detailed descriptions of the analytical conditions and the instrument setup have been published previously (Kelly et al., 2007; Page et al., 2007; Kita et al., 2009; Valley and Kita, 2009; see appendix A1).

Ion microprobe spots were targeted based on CL, SE, and BSE images (Fig. 1.2) taken before isotope analyses. After analysis, each spot was evaluated by SEM to determine (1) if it was located in the overgrowth, detrital grain, or mixed and (2) if any inclusions or irregularities were present in the ion microprobe pit. Spots that overlap the detrital/overgrowth boundary have

a mixed δ^{18} O value and are not considered in discussion of DQ and OQ. Data from spots that comprise two phases (e.g., quartz and epoxy) or feature irregularities (e.g., holes in pit surface) are inaccurate and were discarded. All data are reported in data repository Tables DR1.1 and DR1.2.

RESULTS

Detrital quartz grains from the Mount Simon Sandstone have an average $\delta^{18}O(DQ)$ value of 9.8% \pm 3.5% (2SD, n = 134 grains from 19 rocks; Figure 1.3A; range = 4.2%–14.9% with outliers at 1.1% and 16.6%). Values of $\delta^{18}O(OQ)$ are more variable than $\delta^{18}O(DQ)$ both for total range (12.6% to 28.2% for all samples, n = 593) as well as within individual overgrowths. Two rocks had one overgrowth each that was anomalous in $\delta^{18}O$, out of a total of 10 that were analyzed. These cements are interpreted as a later generation and are not considered further (Tables DR1.1 and DR1.2).

Multiple analyses were made with a 15 μ m spot in 78 individual overgrowths from 15 samples to investigate zoning of $\delta^{18}O(OQ)$ (Fig. 1.3B). Since spots were aimed as close as possible to the edges of the overgrowth, many spots were shown by post-analysis CL imaging to be mixed analyses of DQ and OQ. A total of 73 overgrowths have at least two good (not mixed) spots per overgrowth; many of these have multiple analyses. In general, early-grown cements have higher $\delta^{18}O(OQ)$ and vary toward lower values for later cements at the overgrowth rim. The difference between $\delta^{18}O(OQ)$ of the earliest cement and the latest $\delta^{18}O(OQ)$ value is calculated as $\Delta^{18}O(\text{early-late}) = \delta^{18}O(\text{early-OQ}) - \delta^{18}O(\text{late-OQ})$. The majority (85%) of $\Delta^{18}O(\text{early-late})$ values within the Illinois Basin are positive (Fig. 1.3C). The $\delta^{18}O(\text{early-OQ})$ values tend to

remain relatively constant with present depth (from 0.5 to 2.5 km) while the $\delta^{18}O(\text{late-OQ})$ values for individual overgrowths are lower in deeper samples, which leads to the observed pattern of $\Delta^{18}O(\text{early-late})$ magnitudes increasing with depth (Fig. 1.3C). Detailed traverses were measured on 11 overgrowths using a 5 μ m spot to investigate $\delta^{18}O$ patterns within the overgrowth. Nine of these overgrowths have $\delta^{18}O$ values that decrease from the earliest (high $\delta^{18}O$) to the latest (low $\delta^{18}O$) spots (Fig. 1.4; see data repository figure DR1.1); the other two have no clear trend.

DISCUSSION

Values of $\delta^{18}O(DQ)$ from the Mount Simon Sandstone (9.8‰ ± 3.5‰) are indicative of sources dominated by igneous material (e.g., Taylor, 1968). The distribution of $\delta^{18}O(DQ)$ values does not vary with location or depth. In contrast, rocks deeper in the basin have both a wider range of $\delta^{18}O(OQ)$ values as well as lower minimum $\delta^{18}O(OQ)$ values (Fig. 1.3). The highest $\delta^{18}O(OQ)$ value in each rock, regardless of depth is closest to the DQ boundary and relatively constant at ~26‰. The lowest value however varies significantly and correlates with the depth of the sample.

Two end-member models can be considered for genesis of the quartz cements that are variable in $\delta^{18}O$: (1) the temperature was constant and pore fluid $\delta^{18}O$ varied, or (2) pore fluid $\delta^{18}O$ was constant and temperature varied. We evaluate the extent to which each model can explain the observed trends in $\delta^{18}O$, both basin-wide and at the scale of single overgrowths.

For model 1, if temperature is held constant and fluid composition is varied, the most likely explanation for fluid variation is flow of systematically lower δ^{18} O fluids through buried

sandstones in the Illinois Basin. This is the model proposed by Chen et al. (2001) who concluded fluids would have varied from low to high δ^{18} O values, however the single overgrowth results of this study require that if fluids vary in δ^{18} O, they vary in the opposite direction. Limited fluid inclusion data within quartz overgrowths in the Mount Simon Sandstone give a homogenization temperature (T_h) range of 100–130 °C (average 115 °C) for OQ (Fishman, 1997); however, without more sampling, the timing of fluid inclusions is uncertain. If temperature is constant at 115 °C, then the initial $\delta^{18}O(H_2O)$ was ~+9% to precipitate the earliest overgrowths ($\delta^{18}O =$ +28.5%; Clayton et al., 1972; Friedman and O'Neil, 1977). Constant, elevated temperatures of 115 °C could have resulted from heated fluids flowing from deeper in the basin (late in the history, after burial); and in a fluid-dominated system, $\delta^{18}O(H_2O)$ would not be altered by precipitation of small amounts of cement. However, the monotonic variation of $\delta^{18}O(H_2O)$ from high early values to progressively lower values that is necessary to generate the observed $\delta^{18}O(OQ)$ trends would be fortuitous and unlikely. This is exactly the reverse of what is observed in basin brines; values shift toward higher δ^{18} O due to water-rock interactions (Clayton et al., 1966). In addition, the initial $\delta^{18}O(H_2O)$ values (+9% for assumed T = 115 °C) for model I are <10% higher than Early Paleozoic seawater (~-5 to -1%; Came et al., 2007; Jaffrés et al., 2007). For modern basins, values of $\delta^{18}O(H_2O)$ as high as +9% are only found in the most saline brines that are interpreted to be highly evolved remnants of formation fluids (Clayton et al., 1966).

If, as assumed in model 1, these overgrowths formed at a constant temperature in response to basin-wide fluid movement, then the oxygen isotope results require that the circulating fluids varied systematically across the Illinois Basin with $\delta^{18}O(H_2O)$ evolving

through time from high $\delta^{18}O$ to lower $\delta^{18}O$, and that this fluid evolution was more extreme in the deeper parts of the basin. Furthermore, since the predicted fluid flow in the Illinois Basin is updip toward our sample localities, it would require an unlikely coincidence for larger values of $\Delta^{18}O(\text{early-late})$ to be found only in the deepest parts of the basin where presumably less fluid alteration would have occurred relative to the shallow, northern samples. Thus model 1 cannot satisfactorily explain the observations.

For model 2, δ¹⁸O(H₂O) is constant and temperature increases in order to cause the observed trend to lower $\delta^{18}O(OQ)$. Such growth of overgrowths would be expected during burial and heating. In this situation, fluid flow is possible, but not required. The fluid flux could be nil if cementation is all facilitated by pressure solution. The observed patterns in $\delta^{18}O(OQ)$ values then provide constraints on changes in temperature. Using a constant $\delta^{18}O(H_2O)$ of -3% (approximately early Paleozoic seawater), a temperature of 40 °C would correspond to precipitation of the highest δ^{18} O(early-OQ) value of +28.5% and 107 °C would correspond to the lowest $\delta^{18}O(\text{late-OQ})$ value of +17.5%. If a constant $\delta^{18}O(\text{H}_2O)$ of -1% is used instead, the calculated precipitation temperatures range from 50 to 124 °C. The variability in temperature is ~70 °C regardless of fluid composition, consistent with growth during burial and increasing temperature. This range of temperatures corresponds to a geotherm of ~30 °C/km ("high-T" line in Fig. 1.3). While precipitation is slow below ~80 °C, thin syntaxial quartz overgrowths can precipitate at temperatures below 40 °C, especially in slowly cementing clean quartz arenites (Kelly et al., 2007). The quartz overgrowths show a consistent, basin-wide pattern where the earliest generation of quartz (adjacent to DQ) has similar high $\delta^{18}O(OQ)$ values, and overgrowths are zoned outward toward lower values. This pattern suggests that all quartz overgrowths started at the same conditions, that temperature and/or fluid composition varied systematically, and that growth stopped at different times for different samples, either when porosity is occluded or when burial ceased. Pressure solution can begin early in the burial history (Stone and Siever, 1996), and will provide a source of silica for overgrowth formation. This is consistent with the interpretation that overgrowth formation started relatively early in the burial history (ca. 400 Ma; Duffin et al., 1989; Fishman, 1997). The temperatures calculated from overgrowths in this study and the temperature-time curve used by Fishman (1997) suggest that quartz cementation occurred over a period of ~100 m.y.

The genesis of base-metal sulfide ores in the Upper Mississippi Valley Pb-Zn district is generally attributed to expulsion of metal-rich brines from sandstone aquifers deep in the Illinois basin northwards onto the Wisconsin Dome at ca. 270 Ma (Sverjensky, 1981 Duffin et al., 1989; Brannon et al., 1992). The results of this study suggest that quartz cements formed significantly before Mississippi Valley-type ores. The correlation of increasing magnitude of Δ^{18} O(early-late) with depth fits model 2 well, where temperature increased during quartz growth. This conclusion indicates that overgrowths started to form at shallow depths in all rocks at relatively low temperatures and continued to grow during burial and heating, with little to no variation in δ¹⁸O(H₂O). Both pressure solution and fluid flow are permitted and likely in this model, but temperature exerts the dominant control of $\delta^{18}O(OO)$. The fact that quartz overgrowths are zoned both in $\delta^{18}O$ and CL response suggests a protracted growth history. The detailed shapes of $\delta^{18}O(OQ)$ versus distance plots are interesting and qualitatively correspond with CL zonation. It is possible that quartz precipitation was not a long continuous process, but rather occurred in a series of punctuated events. However, the details of this zonation are beyond the scope of this study and invite future investigation.

CONCLUSIONS

Oxygen isotope variability in diagenetic quartz provides a useful tool for investigating the thermal and fluid evolution of the Illinois Basin. High precision ion microprobe analyses with 5- and 15- μ m spots reveal consistent trends in diagenetic quartz δ^{18} O values, both regionally in the Illinois Basin and within single quartz overgrowths. These trends represent continued, though possibly punctuated, quartz growth with increasing temperatures during burial. If quartz precipitated from fluids similar to Paleozoic seawater, then measured values indicate precipitation from fluids that initially were relatively cool but increased by ~70 °C over the duration of burial and quartz growth. The fluids that formed the cements in these rocks are not related to the Mississippi Valley Type deposits in Wisconsin. The growth of quartz cements in the Mount Simon Sandstone track the burial of the Illinois Basin and further study will provide useful constraints for basin evolution models. The new ability to study isotope zoning within single quartz overgrowths should prove useful in many diagenetic settings.

ACKNOWLEDGMENTS

Sample mounts were made by B. Hess. J. Kern assisted with sample preparation. N. Kita and T. Ushikubo assisted with ion microprobe alignment. Core samples were provided by the Illinois State Geological Survey with the help of R. Mumm and J. Freiburg. R. Dott Jr. and D. Morse assisted with conversations and sample collection. J. Fournelle and P. Gopon assisted with SEM imaging. We thank M. Chan, F. Longstaffe, and an anonymous reviewer for helpful comments. This project was funded by the U.S. Department of Energy (93ER14389), University of Wisconsin–Madison Department of Geoscience, and ExxonMobil Corporation. The WiscSIMS Laboratory (Wisconsin Secondary Ion Mass Spectrometer) is partially funded by National Science Foundation grants EAR-0319230, EAR-0744079, and EAR-1053466.

REFERENCES CITED

- Altschaeffl, A.G., and Harrison, W., 1959, Estimation of a minimum depth of burial for a Pennsylvanian underclay: Journal of Sedimentary Petrology, v. 29, p. 178–185.
- Brannon, J.C., Podosek, F.A., and Mclimans, R.K., 1992, Alleghenian age of the Upper Mississippi Valley zinc lead deposit determined by Rb-Sr dating of sphalerite: Nature, v. 356, p. 509–511, doi:10.1038/356509a0.
- Came, R.E., Eiler, J.M., Veizer, J., Azmy, K., Brand, U., and Weidman, C.R., 2007, Coupling of surface temperatures and atmospheric CO₂ concentrations during the Palaeozoic era: Nature, v. 449, p. 198–201, doi:10.1038/nature06085.
- Chen, Z.S., Riciputi, L.R., Mora, C.I., and Fishman, N.S., 2001, Regional fluid migration in the Illinois Basin: Evidence from in situ oxygen isotope analysis of authigenic K-feldspar and quartz from the Mount Simon Sandstone: Geology, v. 29, p. 1067–1070, doi:10.1130/0091-7613(2001)029<1067:RFMITI>2.0.CO;2.
- Clayton, R.N., Mayeda, T.K., and O'Neil, J.R., 1972, Oxygen isotope-exchange between quartz and water: Journal of Geophysical Research, v. 77, p. 3057–3067, doi:10.1029/JB077i017p03057.
- Clayton, R.N., Friedman, I., Graf, D.L., Mayeda, T.K., Meents, W.F., and Shimp, N.F., 1966, Origin of saline formation waters. 1. Isotopic composition: Journal of Geophysical Research, v. 71, p. 3869–3882.
- Duffin, M.E., Lee, M.C., Klein, G.D., and Hay, R.L., 1989, Potassic diagenesis of Cambrian sandstones and Precambrian granitic basement in UPH-3 deep hole, Upper Mississippi Valley, USA: Journal of Sedimentary Petrology, v. 59, p. 848–861.
- Fishman, N.S., 1997, Basin-wide fluid movement in a Cambrian paleoaquifer: Evidence from the Mount Simon Sandstone, Illinois and Indiana, *in* Montañez, I.P., Gregg, J. M., and Shelton, S.L., eds., Basin-wide diagenetic patterns: Integrated petrologic, geochemical, and hydrologic considerations: Society for Sedimentary Geology Special Paper 57, p. 221–234.
- Friedman, I., and O'Neil, J.R., 1977, Compilation of stable isotope fractionation factors of geochemical interest: Washington, D.C., U.S. Geological Survey Professional Paper 440-KK, 67 p.
- Graham, C.M., Valley, J.W., and Winter, B.L., 1996, Ion microprobe analysis of ¹⁸O/¹⁶O in authigenic and detrital quartz in the St Peter Sandstone, Michigan Basin and Wisconsin Arch, USA: Contrasting diagenetic histories: Geochimica et Cosmochimica Acta, v. 60, p. 5101–5116, doi:10.1016/S0016-7037(96)00286-4.
- Harwood, J., Aplin, A.C., Fialips, C.I.M., Iliffe, J.E., Kozdon, R., and Valley, J.W., 2009, New constraints on quartz cementation histories with oxygen isotope stratigraphies derived from high precision SIMS: AAPG annual convention program, p. 88–89.
- Hervig, R.L., Williams, L.B., Kirkland, I.K., and Longstaffe, F.J., 1995, Oxygen isotope microanalyses of diagenetic quartz: Possible low temperature occlusion of pores:

- Geochimica et Cosmochimica Acta, v. 59, p. 2537–2543, doi:10.1016/0016-7037(95)00148-4
- Hoholick, J.D., Metarko, T., and Potter, P.E., 1984, Regional variations of porosity and cement; St. Peter and Mount Simon Sandstones in Illinois Basin: The American Association of Petroleum Geologists Bulletin, v. 68, p. 753–764.
- Jaffrés, J.B.D., Shields, G.A., and Wallmann, K., 2007, The oxygen isotope evolution of seawater: A critical review of a long-standing controversy and an improved geological water cycle model for the past 3.4 billion years: Earth-Science Reviews, v. 83, p. 83–122, doi:10.1016/j.earscirev.2007.04.002.
- Kelly, J.L., Fu, B., Kita, N.T., and Valley, J.W., 2007, Optically continuous silcrete quartz cements of the St. Peter Sandstone: High precision oxygen isotope analysis by ion microprobe: Geochimica et Cosmochimica Acta, v. 71, p. 3812–3832, doi:10.1016/j.gca.2007.05.014.
- Kita, N.T., Ushikubo, T., Fu, B., and Valley, J.W., 2009, High precision SIMS oxygen isotope analysis and the effect of sample topography: Chemical Geology, v. 264, p. 43–57, doi:10.1016/j.chemgeo.2009.02.012.
- Kolata, D.R., compiler, 2005, Bedrock geology of Illinois: Illinois State Geological Survey, Illinois Map 14, scale 1:500,000.
- Longstaffe, F.J., and Ayalon, A., 1987, Oxygen-isotope studies of clastic diagenesis in the Lower Cretaceous Viking Formation, Alberta: Implications for the role of meteoric water, *in* Marshall, J.D., ed., Diagenesis of Sedimentary Sequences: Geological Society [London] Special Publication 36, p. 277–296.
- Lyon, I.C., Burley, S.D., McKeever, P.J., Saxton, J.M., and Macaulay, C., 2000, Oxygen isotope analysis of authigenic quartz in sandstones: A comparison of ion microprobe and conventional analytical techniques, *in* Worden, R., and Morad, S., eds., Quartz cementation in sandstones: International Association of Sedimentologists Special Publication 29: Malden, Massachusetts, Blackwell Science, p. 299–316.
- Macaulay, C.I., Fallick, A.E., Haszeldine, R.S., and Graham, C.M., 2000, Methods of laser-based stable isotope measurement applied to diagenetic cements and hydrocarbon reservoir quality: Clay Minerals, v. 35, p. 313–322, doi:10.1180/000985500546684.
- Marchand, A.M.E., Macaulay, C.I., Haszeldine, R.S., and Fallick, A.E., 2002, Pore water evolution in oilfield sandstones: Constraints from oxygen isotope microanalyses of quartz cement: Chemical Geology, v. 191, p. 285–304, doi:10.1016/S0009-2541(02)00137-7.
- Page, F.Z., Ushikubo, T., Kita, N.T., Riciputi, L.R., and Valley, J.W., 2007, High-precision oxygen isotope analysis of picogram samples reveals 2 μm gradients and slow diffusion in zircon: The American Mineralogist, v. 92, p. 1772–1775, doi:10.2138/am.2007.2697.
- Rowan, E.L., Goldhaber, M.B., and Hatch, J.R., 2002, Regional fluid flow as a factor in the thermal history of the Illinois basin: Constraints from fluid inclusions and the maturity of Pennsylvanian coals: The American Association of Petroleum Geologists Bulletin, v. 86, p. 257–277.

- Stone, W.N., and Siever, R., 1996, Quantifying compaction, pressure solution and quartz cementation in moderately- and deeply-buried quartzose sandstones from the Greater Green River Basin, Wyoming, *in* Crossey, L.J., Loucks, R. and Totten, M.W., eds., Siliciclastic diagenesis and fluid flow: Concepts and applications: Society for Sedimentary Geology Special Publication 55, p. 129–150.
- Sverjensky, D.A., 1981, Isotopic alteration of carbonate host rocks as a function of water to rock ratio; an example from the Upper Mississippi Valley zinc-lead district: Economic Geology and the Bulletin of the Society of Economic Geologists, v. 76, p. 154–157, doi:10.2113/gsecongeo.76.1.154.
- Taylor, H.P., Jr., 1968, The oxygen isotope geochemistry of igneous rocks: Contributions to Mineralogy and Petrology, v. 19, p. 1–71.
- Templeton, J.S., Jr., 1951, The Mount Simon Sandstone in Northern Illinois, *in* Short papers on geologic subjects: Illinois Geological Survey Circular 170, p. 151–159.
- Valley, J.W., and Kita, N.T., 2009, *In situ* oxygen isotope geochemistry by ion microprobe, *in* Fayek, M., ed., Secondary Ion Mass Spectrometry in the Earth Sciences: Gleaning the big picture from a small spot: Short Course Series 41, Mineralogical Association of Canada, p. 19–63.
- Williams, L.B., Hervig, R.L., and Bjorlykke, K., 1997, New evidence for the origin of quartz cements in hydrocarbon reservoirs revealed by oxygen isotope microanalyses: Geochimica et Cosmochimica Acta, v. 61, p. 2529–2538, doi:10.1016/S0016-7037(97)00111-7.

Figures

Figure 1.1. Cross section of Illinois Basin (United States). Vertical lines represent core locations, squares represent depths of samples analyzed. The shaded unit is the Eau Claire Formation, which confines the Mount Simon Sandstone aquifer. Vertical exaggeration is 73×. Inset shows locations of core and cross section line (gray) in Illinois. Modified from Kolata (2005).

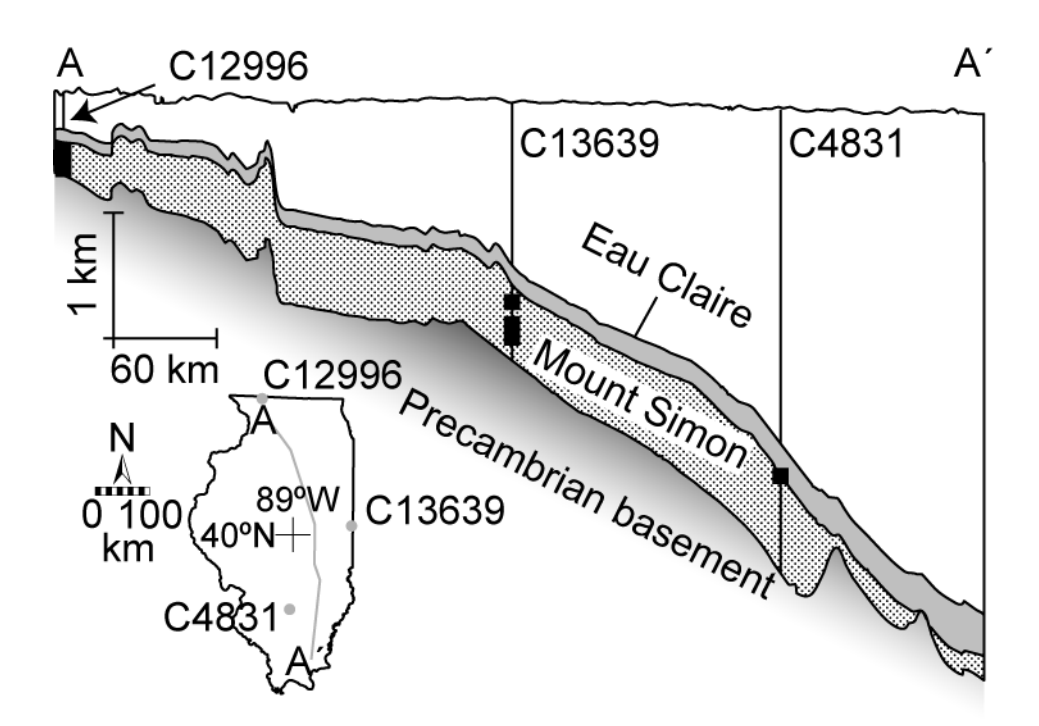


Figure 1.2. Scanning electron microscope images of Mount Simon Sandstone (09IL-41, 1982 m). A: Backscattered electron microscope image. Quartz and K-feldspar are clearly distinguishable. White rectangle represents the area shown in Figure 1.4. B: Cathodoluminescence(CL) image of the same area. Detrital and diagenetic minerals can be distinguished by CL response. This image also shows diagenetic and detrital K-feldspar.

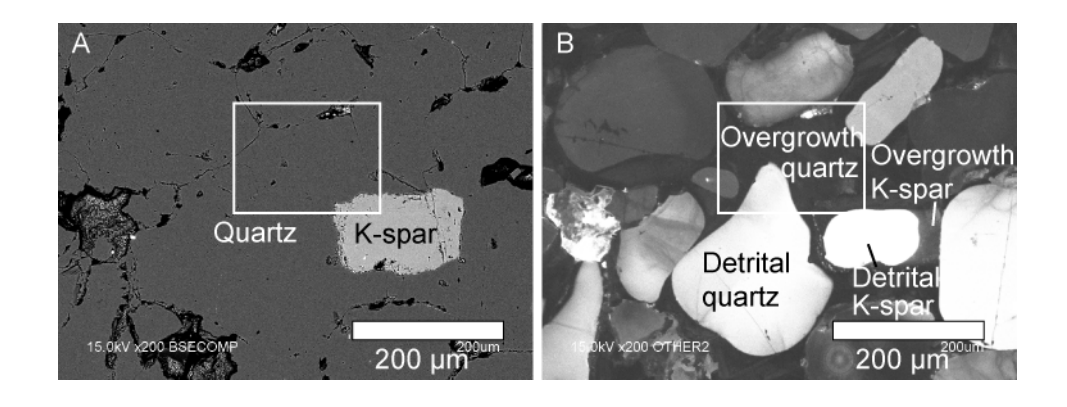


Figure 1.3 (next page). Depth versus δ^{18} O(quartz) from 19 samples of Mount Simon Sandstone in drill core from the Illinois Basin, measured in this study. VSMOW = Vienna Standard Mean Ocean Water. A: The vertical line is the average value of all analyzed detrital grains from the Mount Simon Sandstone. Each cross represents a single detrital grain of quartz (DQ). B: Values of δ^{18} O(OQ), overgrowth quartz, show a trend to lower values and greater range in progressively deeper samples. The High-temperature (*T*) line shows δ^{18} O(OQ) calculated for quartz in equilibrium with a fluid of constant δ^{18} O(H₂O) = -3‰, assuming a paleogeothermal gradient of 30 °C/km, 1 km of uplift and 20 °C at the surface. The Low-*T* line fits the highest values of δ^{18} O(OQ) and does not vary with depth. C: Values of Δ^{18} O(early-late) indicate that the individual OQs are consistently zoned in δ^{18} O; early-formed OQ (adjacent to DQ) versus late-formed OQ (nearest grain boundary). Positive Δ^{18} O indicates individual overgrowths that have highest δ^{18} O(OQ) near DQ. The increase in the magnitude of Δ^{18} O(early-late) indicates that there is a greater gradient in δ^{18} O(OQ) values in samples deeper than 1.5 km. Each triangle represents a single overgrowth with at least two ion microprobe analyses.

Figure 1.3

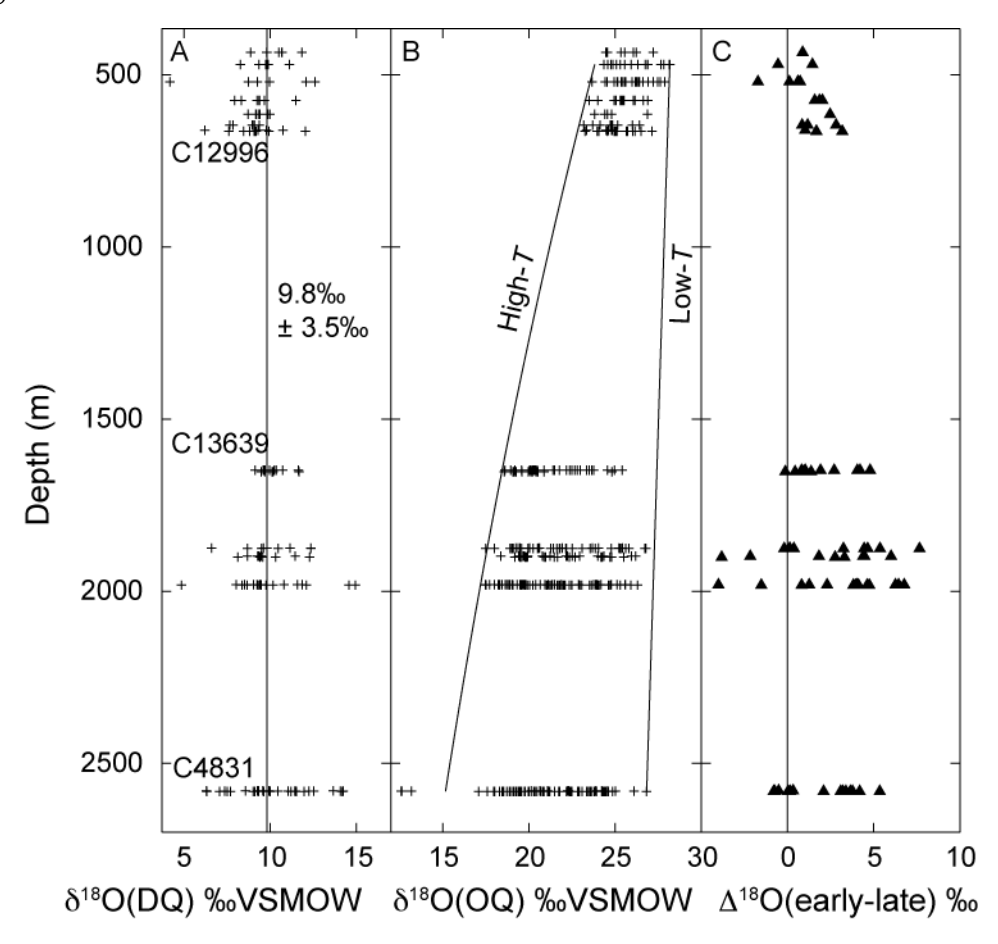
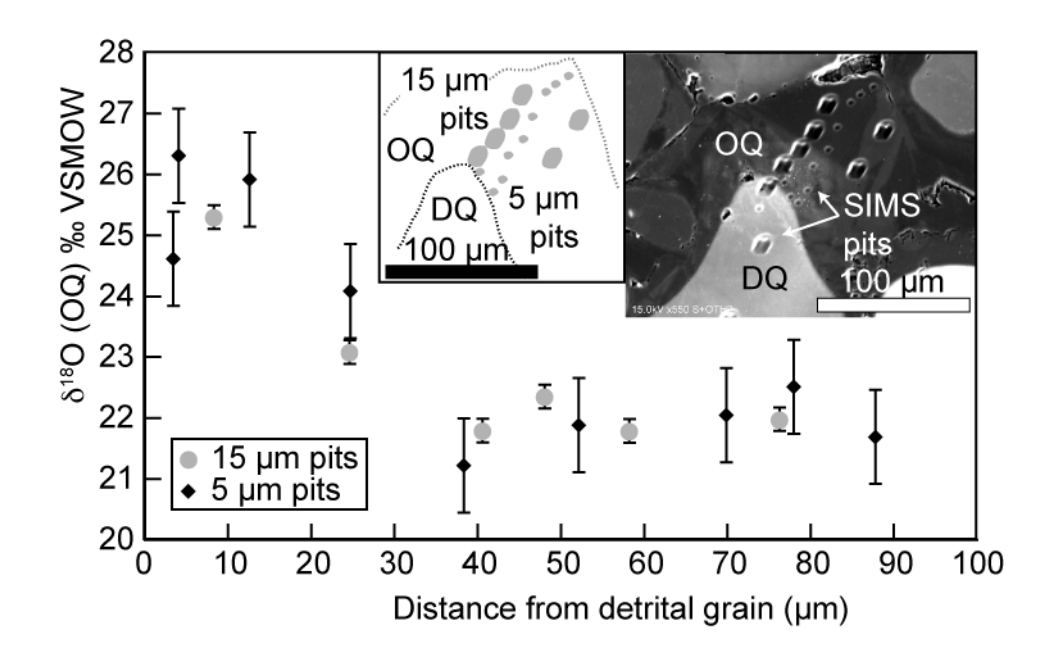


Figure 1.4. Oxygen isotope ratios measured in this study and projected in a traverse of a single quartz overgrowth (OQ) shown in Figure 1.2. The scanning electron microscope image is combined secondary electron and cathodoluminescence. The diagram shows the boundaries of the detrital grain (DQ) and locations of ion microprobe (SIMS, secondary ion mass spectrometer) pits. Distance is calculated from the center of each pit to the boundary of the detrital grain. The data show an overall decrease in $\delta^{18}O(OQ)$ with distance away from the detrital boundary and $\Delta^{18}O(\text{early-late}) = 4.6\%$. The detrital grain averages $\delta^{18}O(DQ) = 4.9\%$. Data from spots that overlap the detrital-overgrowth boundary are not plotted. Error bars are 2 standard deviations. VSMOW = Vienna Standard Mean Ocean Water.



Appendix A1

MT. SIMON DIAGENESIS

The distribution and composition of diagenetic material has been described both modally (e.g., Templeton, 1951; Hoholick et al., 1984; Duffin et al., 1989) and chemically (e.g., Duffin et al., 1989; Chen et al., 2001). Hoholick et al. (1984) mapped the distribution of dominant cement and porosity types in the Mt. Simon in Illinois based on descriptions of core samples from the basin. The cements are dominantly quartz and K-feldspar and minor amounts of hematite, kaolinite, chlorite, microquartz and carbonate (Hoholick et al., 1984).

METHODS

Sample preparation

Each rock was cut into blocks of $\sim 1~\rm cm^3$ and cast in 2.5 cm epoxy rounds with 4 pieces of the quartz standard UWQ-1 (δ^{18} O=12.33‰ VSMOW; Kelly et al., 2007) and one other rock (Fig. A1.1). Epoxy rounds were prepared with two samples per mount in order to minimize the time required for sample change and re-standardization. Epoxy mounts have sequential numbering based on when they were prepared (i.e., MSim-1, MSim-2, etc.). Prior to imaging and isotope analysis all samples were cleaned in deionized water and ethyl alcohol and stored in a vacuum desiccator. All analyses are within 5 mm of the center of the mount in order to prevent instrument bias related to position (Kita et al., 2009; Valley and Kita, 2009).

Analytical conditions

Data were collected from spots $\sim 15~\mu m$ in diameter during seven sessions between July and December 2009 and from spots $\sim 5~\mu m$ in diameter during three sessions between November 2009 and February 2010. A total of 1179 spot analyses (727 sample, 452 standard) were analyzed during the ten sessions.

Two different analytical settings were used: (I) a \sim 15 μ m diameter 133 Cs⁺ primary beam with an intensity of 2.1 nA, (II) a \sim 30 pA 133 Cs⁺ primary beam with a beam spot size of \sim 5 μ m. "Normal" spot size varied from 10 μ m to 20 μ m and small spot size varied from 5 μ m to 6 μ m due to slight variability in the primary beam. For clarity in the text, we call these spots 15 μ m and 5 μ m respectively.

In both settings, the mass resolving power (MRP, M/ΔM), measured at 10% peak height, was set at 2200. The magnetic field strength was held at a constant stable value using a nuclear magnetic resonance (NMR) probe, which is readjusted every 12 hours. For 15 μm spot analyses, two Faraday cup detectors were used to simultaneously collect sputtered ¹⁶O⁻ and ¹⁸O⁻ ions with an average ¹⁶O⁻ intensity of 2.6x10⁹ cps. Each spot analysis took about ~4 minutes, which includes 10s of presputtering to penetrate the carbon coat, ~60s to automatically center the secondary ions in the field aperture using high voltage deflectors and 80s (20 cycles of 4s each) of integrating secondary ions.

For small spot analysis, the typical secondary ¹⁶O⁻ ion intensity was 2.3x10⁷ cps. The ¹⁶O⁻ ions were collected with a Faraday cup while ¹⁸O⁻ ions were collected with an electron multiplier in pulse counting mode. A single small spot analysis took ~6 minutes which includes ~60s presputtering, ~60s centering of the secondary ions in the field aperture, and ~200s (25 cycles of 8s each) integration of secondary ions. Detailed descriptions of these analytical

conditions and the instrument setup have been published previously (Kelly et al., 2007; Page et al., 2007; Kita et al., 2009; Valley and Kita, 2009).

For quartz analyzed during this study the bias varied, session-to-session, depending on instrument conditions from -4.5% to -6.6% (average=-5.8%, n=614) for 15 μ m spots and from -11.3% to -13.6% (average=-12.2%, n=113) for 5 μ m spots. The precision of each bracket is taken as the reproducibility of a set of individual standard analyses (Valley and Kita, 2009).

Factors influencing $\delta^{18}O(OQ)$

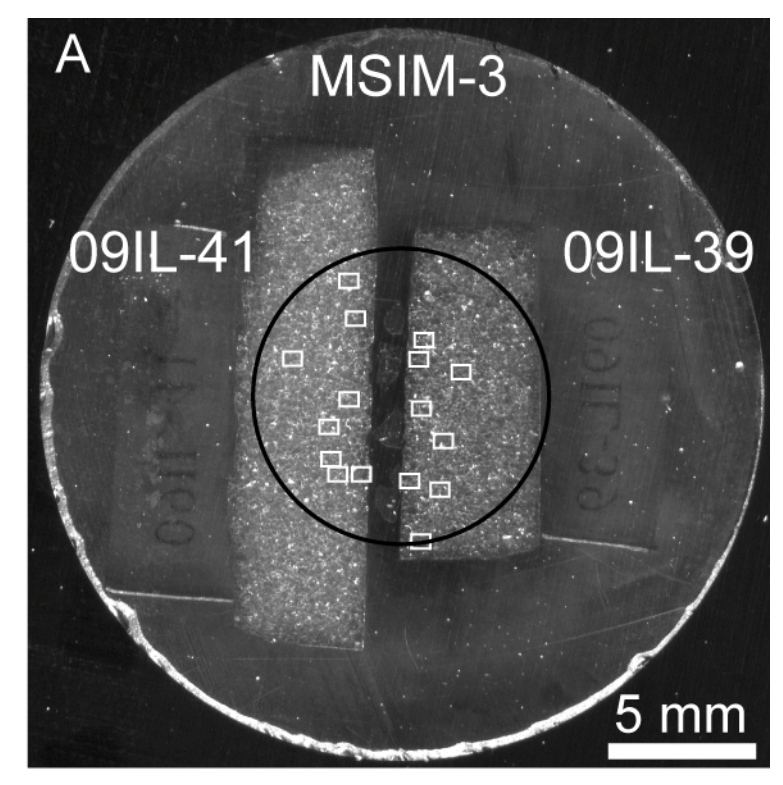
In detail the δ^{18} O(fluid) can vary with temperature, composition, and water/rock (W/R) ratio or flux (e.g., Dickinson, 1987), and the composition of the fluid is influenced by pH, other gas species, and dissolved solids (Horita et al., 1995; Marchand et al., 2002; Hu and Clayton, 2003; Beck et al., 2005). The fractionation of δ^{18} O between quartz and water in equilibrium is experimentally calibrated at temperatures down to 200°C [Δ^{18} O(quartz-fluid) = δ^{18} O(quartz)- δ^{18} O(fluid) $\approx 3.38(10^6/T^2)$ -2.90; Clayton et al. (1972) (Friedman and O'Neil, 1977)] where T is the temperature in Kelvin; These experiments were performed at temperatures closest to basin temperatures, and are in good agreement with results of Hu and Clayton (2003) at higher temperatures.

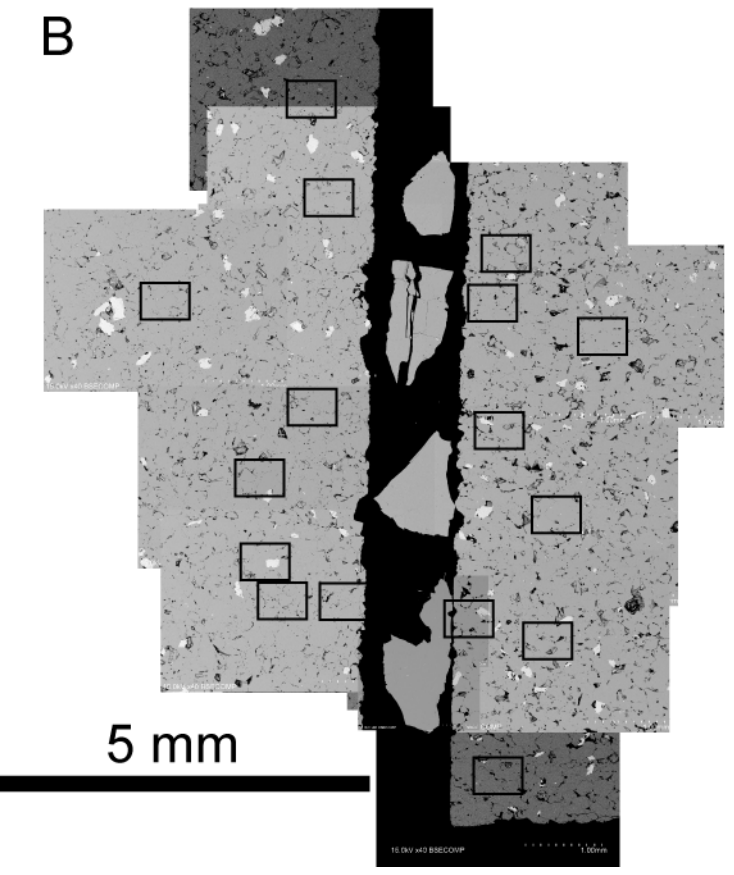
ADDITIONAL REFERENCES NOT CITED IN MAIN TEXT

- Beck, W.C., Grossman, E.L., and Morse, J.W., 2005, Experimental studies of oxygen isotope fractionation in the carbonic acid system at 15°, 25°, and 40°C: Geochimica Et Cosmochimica Acta, v. 69, p. 3493-3503.
- Dickinson, W.W., 1987, An Oxygen Isotope Model for Interpreting Carbonate Diagenesis in Nonmarine Rocks (Green River Basin, Wyoming, USA): Chemical Geology, v. 65, p. 103-116.
- Friedman, I., O'Neil, J.R., 1977. Compilation of stable isotope fractionation factors of geochemical interest. United States Geological Survey professional paper 440-KK, Washington, D.C., 67 p.
- Hu, G.X., and Clayton, R.N., 2003, Oxygen isotope salt effects at high pressure and high temperature and the calibration of oxygen isotope geothermometers: Geochimica Et Cosmochimica Acta, v. 67, p. 3227-3246.

Appendix Figures

Figure A1.1 (next page). Samples cast in epoxy. a) Photograph of two rock chips (09IL-39, 09IL-41) cast in 25 mm diameter epoxy mount MSim-3. White rectangles represent areas selected for detailed imaging preparatory to ion microprobe analysis. Black circle represents the inner 10 mm, where analyses can be made without machine-induced position bias. Area 15, which is outside the 10 mm circle was not analyzed. b) BSE map of MSim-3. Grayscale in BSE images is proportional to the mean atomic weight of the material; in this image black is epoxy, white is K-feldspar and light gray is quartz. Four grains of the standard UWQ-1 are mounted between the rock chips. Black rectangles represent areas selected for ion microprobe analysis.





Data repository (DR1)

Large data tables and figures for individual chapters are included in the supplementary files available with the online version of this dissertation.

Table DR1.1. Oxygen isotope composition of detrital and diagenetic quartz measured on the WiscSIMS ims-1280 ion microprobe using a 15 μm spot size.

Table DR1.2. Oxygen isotope composition of detrital and diagenetic quartz measured on the WiscSIMS ims-1280 ion microprobe using a 5 μm spot size.

Figure DR1.1. SEM images and δ^{18} O vs. distance plots for every overgrowth analyzed with 5 μ m spots. The first two overgrowths show no clear trend, whereas the other 9 all have overall decreasing trends. Overgrowths are plotted in depth order with the shallowest at the top.

CHAPTER 2

A previously unrecognized episode of low temperature feldspar diagenesis in Cambrian Mount Simon and Eau Claire formations revealed by in situ microanalysis of $\delta^{18}O$

Planned for submission with the following authors: Anthony D. Pollington, Ayumi Hyodo, Reinhard Kozdon, John W. Valley

Abstract

Oxygen isotope ratios of diagenetic cements in sedimentary rocks record evidence of the thermal, fluid, and chemical history of a formation. *In situ* analyses of quartz and feldspar overgrowths from the Cambrian Mt. Simon Sandstone and Eau Claire Formation provide evidence of a diagenetic history dominated by increasing temperature during burial. The δ^{18} O values and textural relations of diagenetic feldspar from the two formations indicate growth at low temperatures, relatively early in the burial history. Individual quartz overgrowths are consistently zoned with declining δ^{18} O towards grain boundaries by as much as 9% due to growth over a prolonged period, while individual feldspar overgrowths show little to no isotopic zonation suggesting growth over a shorter time frame at relatively constant temperature. The δ^{18} O values for feldspar overgrowths are 15-25% VSMOW. Modeled temperatures for feldspar precipitation are 20-60°C assuming δ^{18} O(H₂O) = -3%. Feldspar overgrowths are interpreted to have precipitated early in the diagenetic history at relatively low temperature, reflecting a previously undescribed period of feldspar diagenesis.

Abbreviations

VSMOW Vienna Standard Mean Ocean Water

Qz Quartz

DQ Detrital quartz

OQ Overgrowth quartz

Kfs K-feldspar

DK Detrital K-feldspar

OK Overgrowth K-feldspar

SEM Scanning electron microscope

SE Secondary electron

BSE Backscattered electron

CL Cathodoluminescence

EDS Energy dispersive spectrometry

SIMS Secondary ion mass spectrometer

UWQ-1 University of Wisconsin quartz standard

MRP Mass resolving power

Introduction

Diagenesis is an important factor in controlling the porosity and permeability of reservoir and cap-rock formations. Pore-reducing cements may form at any time post-deposition, and the timing of cementation can have a large impact on the flow regimes and storage capacity of hydrocarbon reservoirs, aquifers, and importantly on the sealing properties of formations above reservoirs.

The study of diagenesis has evolved from a description-based approach to incorporating geochemical datasets and modeling past conditions (cf., Worden and Burley, 2003 and references therein). Recently, advances in analytical techniques have made possible the in situ investigation of oxygen isotope (δ^{18} O) variability in quartz cements from sedimentary rocks (e.g., Hervig et al., 1995; Graham et al., 1996; Williams et al., 1997; Lyon et al., 2000; Macaulay et al., 2000; Chen et al., 2001; Marchand et al., 2002; Kelly et al., 2007; Pollington et al., 2011; Harwood et al., 2013; Hyodo et al., 2013). Whereas many studies have focused on the $\delta^{18}O$ values of quartz cements, relatively few have focused on the *in situ* variability of δ^{18} O in feldspar cements. Bulk values for physically separated feldspar cements have been used to calculate temperatures and pore water $\delta^{18}O$ compositions (Savin and Epstein, 1970; Lawrence and Kastner, 1975; Kastner and Siever, 1979; Land and Milliken, 1981; Shieh, 1983; Hay et al., 1988; Duffin, 1989; Stallard and Boles, 1989) but to our knowledge only one study has reported in situ measurements of δ^{18} O in diagenetic feldspar (Chen et al., 2001) and none have attained the high accuracy and precision, or the small spot size possible with a newer multi-collector ion microprobe.

Quartz-feldspar isotope thermometry has been proposed as a means for measuring diagenetic temperatures in sandstones (e.g., Kastner and Siever, 1979; Chen et al., 2001).

However, this requires that the two phases are coeval and were in isotopic equilibrium at the time of precipitation. In many formations, this assumption is not be valid where diagenetic phases may have precipitated at different times in the burial history and were therefore not in thermal or isotopic equilibrium at the time of formation. While paired measurements of $\delta^{18}O$ in diagenetic quartz and feldspar yield meaningless mineral-mineral temperatures if the minerals precipitated at different times, the opportunity exists to study a broader period of the burial and diagenetic history of a formation by analyzing a sequence of diagenetic phases as opposed to measuring only a single mineral.

Brine migration associated with flow from tectonic belts has formed economic ore deposits across the continental interior of North America (see review in Bethke and Marshak, 1990). Fluids leached metals from Precambrian basement rocks to make sulfide deposits and were also responsible for regional illitization and precipitation of diagenetic K-feldspar. Feldspar cement and authigenic sericite from the middle Cambrian Mt. Simon Sandstone (Ss) in northern Illinois have been linked temporally to periods of mountain building east and south of the Illinois Basin, relatively late in the formation's burial history. The dated K-feldspar (~395 Ma) and sericite (~270-214 Ma) correspond to uplift of the Findlay-Algonquin and Pascola arches respectively (Duffin et al., 1989).

In this study we present the first high-resolution dataset of *in situ* δ^{18} O measurements for diagenetic feldspar along with descriptions of textural relationships between quartz and feldspar, which are the major diagenetic minerals. We interpret the δ^{18} O values of diagenetic feldspar from the Cambrian Mt. Simon and Eau Claire formations in the context of textural evidence and δ^{18} O measurements of diagenetic quartz as reflecting growth at low temperatures early in the history of the two formations. Low-temperature, early growth is inconsistent with the regional

scale brine migration inferred for ore deposits and K-metasomatism, which is proposed to occur late in the burial history at relatively high temperatures (up to 150°C; Sverjensky, 1986), and we therefore propose a previously unrecognized period of feldspar overgrowth formation that is unrelated to the regional K-metasomatism and brine migration described by previous authors (e.g., Bethke and Marshak, 1990).

Geologic setting and Samples

Clastic samples

The Mt. Simon Sandstone is a quartz arenite with minor lithologic and mineralogic variability that has been described by previous authors (Templeton, 1951; Willman et al., 1975; Hoholick et al., 1984; Duffin et al., 1989; Chen et al., 2001; Bowen et al., 2011; Pollington et al., 2011). The formation is the basal Cambrian formation and unconformably overlies the Precambrian basement in much of Illinois and neighboring states, with the exception of nondeposition on paleotopographic highs (Templeton, 1951; Leetaru and McBride, 2009). The majority of the Mt. Simon Ss was deposited in a marine setting, although some sections, particularly in the lower units, also contain evidence of tidal, coastal, alluvial, eolian and possibly sabkha deposition (Willman et al., 1975; Driese et al., 1981; Hoholick et al., 1984; Hagadorn et al., 2002; Fischietto, 2009; Bowen et al., 2011). While the dominant mineralogy is quartz, there is also a significant amount of detrital K-feldspar in some samples (5-40%), particularly in the lower-most parts of the formation (Driese et al., 1981; Hoholick et al., 1984; Duffin et al., 1989; Bowen et al., 2011). This may be due to reworking of the feldspar-rich Precambrian basement (e.g., Odom, 1975). The porosity of the sandstone ranges from ~25% in outcrops and shallow samples to less than 2% in deeply buried samples (Driese et al., 1981;

Hoholick et al., 1984; Bowen et al., 2011). The trend of decreasing porosity with depth in the formation was described by Hoholick et al. (1984) and interpreted as being due to compaction and cementation during burial and less secondary porosity in deeper samples. However Bowen et al. (2011) pointed out that while this trend holds true for the highest porosities, there is significant variability at any given depth suggesting that cementation can significantly occlude porosity even in shallowly buried samples. The diagenetic history of the formation has been previously studied with a range of techniques. Diagenetic textures of minor cements have been interpreted to vary spatially across the Illinois Basin, while the major cements (quartz and feldspar overgrowths) are present in almost all samples from the basin (Hoholick et al., 1984; Bowen et al., 2011) and that quartz cements predate large-scale compaction and brittle grain deformation (Makowitz et al., 2006). The major cements have been investigated chemically and interpreted to represent growth in either changing fluid conditions (Chen et al., 2001) or changing temperature conditions (Pollington et al., 2011). The ambiguity between these two interpretations was related to previous technical limitations of cement analysis and was removed by Pollington et al. (2011) who used high-resolution isotope measurements to show that individual quartz overgrowths are zoned in δ^{18} O, reflecting increases in temperature during precipitation.

The Eau Claire Formation (Fm) grades into and conformably overlies the Mt. Simon Ss. The formation was originally described wholly as a shaly sandstone (Walcott, 1914) but has since been subdivided into five lithofacies based on mineralogy and grain size (Aswasereelert et al., 2008; Neufelder et al., 2012). The Eau Claire Fm was deposited as part of the Sauk sequence (Sloss, 1963) in varying water depths as evidenced by the small scale variability of grain size and mineralogy (Morrison, 1968; Distefano, 1973; Aswasereelert et al., 2008). Lenses of sand within

a finer-grained matrix, as well as small-scale (mm to cm) layer-to-layer variability in grain size exists throughout the formation. Quartz and feldspar cementation has occurred in the Eau Claire Fm and has been described in detail both texturally and chemically. Fabrics in the formation show that there have been multiple episodes of dissolution and precipitation of minerals over the burial history (Neufelder et al., 2012). The earliest cements observed are syntaxial overgrowths of quartz and feldspar on detrital grains, followed by euhedral carbonate cements that grew in pore spaces. The oxygen isotope record of diagenetic quartz in the Eau Claire Fm is interpreted to reflect a similar burial and heating history as the underlying Mt. Simon Ss (Hyodo et al., 2013). While it is not surprising that adjacent formations experienced largely the same thermal history, the similar record recorded in oxygen isotopes is particularly interesting because it suggests a similarity between the fluid histories of two formations with significantly different hydraulic properties.

The samples in this study come from drill cores in the Illinois Basin and on the transitional section between the Basin and the Wisconsin Arch (Fig. 1, table 1, Pollington et al., 2011; Hyodo et al., 2013) and were selected to cover a range of depths (85-2581 m) and wide geographic distribution (>500 km north to south). Samples of the Eau Claire Fm used in this study are generally from sand lenses within finer grained layers. As described previously (Pollington et al., 2011; Hyodo et al., 2013) the diagenetic minerals in samples used in this study consist largely of syntaxial quartz and feldspar overgrowths. Fine-grained interstitial cements such as illite and smectite have been described from other samples by other authors (e.g., Neufelder et al., 2012). Samples studied by other authors as well as some of the samples in this study also have abundant pore-filling carbonate cements. Both the clay and carbonate cements

are more common in the more chemically immature Eau Claire, but are not discussed further in this study.

Methods

Sample preparation and imaging

Samples were prepared as thin sections or as 1 cm³ rock chips cast in 25-mm round epoxy mounts with the quartz standard UWQ-1 (δ^{18} O=12.33‰ VSMOW; Kelly et al., 2007). Samples were ground and polished with polycrystalline diamond suspension and colloidal alumina for flatness and to minimize relief (Kita et al., 2009). Prior to isotope analyses, all samples were imaged and documented in detail by optical microscope and on a Hitachi 3400 scanning electron microscope (SEM) at the University of Wisconsin-Madison with secondary electron (SE), backscattered electron (BSE), cathodoluminescence (CL) and energy dispersive spectroscopy (EDS) detectors. Overgrowth cements of both quartz (OQ) and K-feldspar (OK) are commonly difficult or impossible to distinguish from their respective detrital quartz (DQ) or feldspar (DK) grains using optical, SE or BSE microscopy. Cements however are easily distinguished from detrital grains by CL (Fig. 2.2).

Feldspar standards

Four feldspar samples with a range of major element chemistry were evaluated as potential SIMS standards. They consist of two geochronology sanidine standards (Fish Canyon Tuff, Renne et al., 1998; Melilla-Nador basin tephra, Kuiper et al., 2008), a K-feldspar from the University of Wisconsin mineral collection, and a plagioclase purchased online. The major-element and isotopic compositions of the four samples were characterized by electron

microprobe, laser fluorination, and ion microprobe. Of the samples analyzed for potential K-feldspar ion microprobe standards, the Fish Canyon Sanidine is the most homogenous in δ^{18} O (δ^{18} O=7.06±0.17‰) and will be a useful standard for the microanalysis of oxygen isotopes in alkali feldspar. Details of all samples considered as potential standards are summarized in appendix A2.

Oxygen isotope measurements

Oxygen isotope ratios of detrital and diagenetic minerals were analyzed *in situ* on a CAMECA ims-1280 ion microprobe at WiscSIMS (Kita et al., 2009; Valley and Kita, 2009) on carbon coated samples with a ¹³³Cs⁺ primary beam focused to either ~15 μm or ~5 μm diameter. A total of 811 spot analyses (394 sample, 93 feldspar standard, 324 quartz standard) were performed during the four analytical sessions. The total number of spots on clastic samples from this study as well as previously published data used in this compilation is 1036 (636 OQ, 122 OK, 306 DQ, 83 DK).

Two different analytical settings were used: (I) a 2.1 nA 133 Cs⁺ primary beam with a spot size of ~15 µm, (II) a ~30 pA 133 Cs⁺ primary beam with a spot size of ~5 µm. The mass resolving power (MRP, M/ Δ M), measured at 10% peak height, for both analytical conditions was set at 2200. The magnetic field strength was held at a constant stable value using a nuclear magnetic resonance (NMR) probe, which is readjusted every 12 hours. For 15 µm spot analyses, 16 O⁻ and 18 O⁻ ions were simultaneously collected in two Faraday cup detectors with an average 16 O⁻ intensity of 2.5x10⁹ cps. Each spot analysis took about ~4 minutes, which includes 10s of presputtering to penetrate the carbon coat, ~60s to stabilize sputtering and automatically center

the secondary ions in the field aperture and 80s (20 cycles of 4s each) of integrating secondary ions.

For small spot analysis, ¹⁶O ions were collected with a Faraday cup while ¹⁸O ions were collected with an electron multiplier in pulse-counting mode. The average secondary ¹⁶O ion intensity was 3.2×10^7 cps. A single small spot analysis took ~6 minutes which includes ~60s presputtering, ~60s centering of the secondary ions in the field aperture, and ~200s (25 cycles of 8s each) integration of secondary ions. Detailed descriptions of these analytical conditions and the instrument setup at WiscSIMS have been published previously (Kelly et al., 2007; Page et al., 2007; Kita et al., 2009; Valley and Kita, 2009).

All data were collected with a standard-sample-standard bracketing procedure of four UWQ-1 standard measurements, 3-20 sample measurements and four UWQ-1 standard measurements. Bracketing standards are used to evaluate the reproducibility of a series of measurements as well as to correct for the instrumental bias. The external spot-to-spot reproducibility of bracketing standards averaged $\pm 0.27\%$ (2SD) for 15 μ m spots and $\pm 0.89\%$ (2SD) for 5 μ m spots. Raw values of δ^{18} O measured by SIMS are corrected to the VSMOW scale based on values measured for the UWQ-1 bracketing standards and feldspar standards (appendix A2; Kita et al., 2009). Minerals that have solid solution (such as feldspars) have instrumental mass biases, which differ as a function of mineral chemistry and crystal structure. These biases are corrected for by analyzing standards with a range of major element composition, from which a calibration curve is constructed during each analysis session. Details of this method and calculation are described for alkali feldspars in appendix A2, and by previous authors for other mineral families (Valley and Kita, 2009; Page et al., 2010).

Locations for ion microprobe analyses were selected based on CL, SE and BSE images (Fig. 2.2). After each analysis session, SIMS pits were investigated by SEM to verify their location in overgrowths, detrital grains, or mixtures and to check for inclusions or pit irregularities. Spots that overlap the detrital/overgrowth boundary have a mixture of oxygen from the two different sources and are not considered further. Spots that are a mixture of two phases (e.g., quartz and feldspar, or quartz and epoxy) or have irregularities (e.g., holes or inclusions) are inaccurate and were discarded. All data are included in data repository Table DR2.2.

Electron microprobe

Major element chemistry (K, Al, Si, Na, Ca, Ba, Fe) for feldspar standards and samples was measured on a CAMECA SX51 in the Eugene Cameron Electron Microprobe Laboratory at UW-Madison. Samples were sputter coated with ~250Å of carbon. Measurements were made using a 10 nA electron beam and an accelerating voltage of 15 kV with a 10 μm spot size. Counting times, diffraction crystals and standards used during electron probe microanalysis (EPMA) are summarized in appendix Table A2.3. Measured values for unknowns were standardized to in-house and international standards. Elemental percentages were calculated using the Probe For EPMA software.

Results

Textural relationships

The dominant cement types in the Mt. Simon Ss and the Eau Claire Fm are quartz and feldspar overgrowths. Determining the order of mineralization is important in interpreting the chemical changes that led to precipitation of these phases. By comparing CL and BSE images it

is possible to determine a clear order of diagenesis in many samples. For most of the samples used in this study, feldspar overgrowths predate quartz overgrowths. This is evidenced by euhedral and subhedral feldspar morphologies (Fig. 2.3 A, B), subhedral quartz overgrowths that grew to impingement against euhedral feldspar overgrowths, and feldspar overgrowths abutting detrital quartz (Fig. 2.3 A, B). While most of the quartz-feldspar relations in the study samples have feldspar overgrowths that predate quartz overgrowths, there are a few examples that deviate from this. In some samples there appear to be cogenetic quartz and feldspar overgrowths, as seen by the interfingering of the two diagenetic phases (Fig. 2.3 C, D). However, this feature is not definitive and could also be fine-scale terminations of early precipitated K-feldspar, which did not reach full euhedral crystals (Stablein and Dapples, 1977), where quartz later precipitated and filled in. A previous study that used samples from the same drill core and approximate depth as this study showed small amounts of quartz overgrowth that appear to predate feldspar overgrowth (figure 3D from Duffin et al., 1989). This relation has also been seen in some samples from the current study, with very thin quartz overgrowths (Fig. 2.3 E, F), although this texture is ambiguous in these samples and may actually be thin quartz overgrowths that postdate K-feldspar. Pressure solution of detrital quartz has been observed in all samples regardless of depth (Fig. 3 E-H; Pollington et al., 2011; Hyodo et al., 2013) and of detrital feldspar grains in some samples (Fig. 2.3 G, H).

Mineral chemistry

Detrital feldspar grains from the Mt. Simon Ss were analyzed by EPMA and range from 91.4 to 100% K-feldspar (Kfs) and have an average mol% Kfs (formula atoms K/Na+Ca+K) of $95.9 \pm 3.3\%$ (2SD, n=97, Fig. 2.4). Feldspar overgrowths are slightly more potassium rich with

an average of 99.3 \pm 1.9 mol% Kfs (2SD, n=133, range=94.7 to 100%, Fig. 2.4). Detrital feldspar grains from the Eau Claire Fm have a similar average composition (95.0 \pm 4.4 mol% Kfs, 2SD, n=221) to detrital grains from the Mt. Simon Ss, but a wider range (87.4 to 99.6%). Similar to the Mt. Simon Ss, feldspar overgrowths from the Eau Claire Fm are higher in average mol% Kfs (99.1 \pm 1.9%, 2SD, n=183, range=92.9 to 100%) than the corresponding detrital grains. Detrital grains from the Eau Claire Fm also have slightly higher mol% anorthite (An) $(0.14 \pm 0.63\%, 2SD, n=221, range=0 \text{ to } 3.8\%)$ compared to Mt. Simon Ss detrital grains $(0.04 \pm 0.63\%, 2SD, n=221, range=0 \text{ to } 3.8\%)$ 0.14%, 2SD, n=97, range=0 to 0.27%). Overgrowths of feldspars from both formations have similar average mol% An to the detrital grains from the respective formations (Eau Claire Fm average mol% An = $0.16 \pm 0.56\%$, 2SD, n=183, range=0 to 1.6%; Mt. Simon Ss average mol% An = $0.01 \pm 0.06\%$, 2SD, n=133, range=0 to 0.21%). The data for major element composition of both formations are summarized in Figure 2.4 and data repository Table DR2.3. Calcium concentration correlates between detrital grains and overgrowths, particularly in the Eau Claire Fm (Fig. 2.5 and appendix Fig. A2.3); in rocks where concentrations of Ca are high in detrital grains, they are correspondingly high in overgrowths.

Oxygen isotope ratios

Detrital quartz grains of the Mt. Simon Ss and Eau Claire Fm from this study, taken together with those published in Pollington et al. (2011) and Hyodo et al. (2013), have an average $\delta^{18}O(DQ)$ value of $9.9 \pm 3.8\%$ (2SD, n = 306 grains from 31 rocks, range = 0.7 to 16.6%, Fig. 2.6A). Quartz overgrowths from Illinois Basin samples in this study and those reported in Pollington et al. (2011) and Hyodo et al. (2013) have a total range of 12.6 to 31.9 % (n=636).

Detrital feldspar grains have an average $\delta^{18}O(DK)$ of 8.2±3.4‰ (2SD, n = 83 grains from 17 rocks; range = 3.5 to 15.5‰, Fig. 2.6A). Feldspar overgrowths from the Mt. Simon and Eau Claire formations in the Illinois Basin have similar $\delta^{18}O$ values (Mt. Simon Ss average = 18.4 ± 5.2‰ 2SD, n=46, range=14.2 to 24.7‰; Eau Claire Fm average = 19.9 ± 3.6‰ 2SD, n=76, range=15.5 to 23.5‰, Fig. 2.6B). The total range in any rock is less than 3.5‰, when outliers are excluded (appendix Fig. A2.4). Feldspar overgrowths from the Wisconsin Arch (Eau Claire sample WI84.7) as well as the transitional area between the Illinois Basin and the Wisconsin Arch (Mt. Simon and Eau Claire from UPH-3 drill core) have higher $\delta^{18}O$ values (average = 21.1 ± 2.9‰ 2SD, n = 60, range=17.8 to 24.7‰) than samples from deeper in the basin. There is an overall trend of average $\delta^{18}O(OK)$ decreasing with increasing depth (Fig. 2.6B), although this is not nearly as pronounced as the trend in $\delta^{18}O(OQ)$.

Multiple overgrowths were analyzed with traverses of two or more spots in order to investigate zonation of $\delta^{18}O$ (Fig. 2.6C). The quartz overgrowths in both formations are systematically zoned in $\delta^{18}O(OQ)$ with the $\delta^{18}O$ values of the innermost cement near the detrital grain (early growth) in each overgrowth higher than later values (Pollington et al., 2011; Hyodo et al., 2013). The zonation within single overgrowths can be described by:

$$\Delta^{18}O(\text{early-late-OQ}) = \delta^{18}O(\text{OQ-earliest spot}) - \delta^{18}O(\text{OQ-latest spot})$$
 (1)

and similarly for $\Delta^{18}O(\text{early-late-OK})$. In this scheme, overgrowths that have late cements that are lower in $\delta^{18}O(\text{early-late})$ values. Whereas the $\Delta^{18}O(\text{early-late-OQ})$ values varied with depth and were as high as ~9‰, the feldspar overgrowths are nearly homogeneous. Values of $\Delta^{18}O(\text{early-late-OK})$ are constant with depth,

and are very close to zero (no zonation). Of the 25 feldspar overgrowths with more than one measured spot, 17 have Δ^{18} O(early-late) values that are within analytical uncertainty of zero.

As discussed previously, δ^{18} O values from spots that are mixtures of overgrowths and detrital grains are not considered in the discussion of individual spots. However, they may be used in calculations of Δ^{18} O(early-late). Since the detrital K-feldspar grains have average δ^{18} O values of ~8‰ and the early overgrowths are above 20‰, an "overgrowth" spot that is a mixture of the two phases will have an apparent $\delta^{18}\mathrm{O}$ value lower than the true value. Because mixed spots of this kind are exclusively early spots, this leads to a minimum estimate for Δ^{18} O. Due to the tendency of smaller overgrowths in the Eau Claire Fm compared to the Mt. Simon Ss, all of the overgrowths that have mixed early spots are from that formation (7 of 12 Δ^{18} O measurements in the Eau Claire). Additionally, by necessity of positioning the SIMS beam to try to avoid mixed analyses, "early" spots are always a small distance into the overgrowth from the detrital boundary and "late" spots are always a small distance into the overgrowth from the edge of the overgrowth. Thus the full range of δ^{18} O values is not captured. The location of these spots has a larger effect on the early value where growth rates are slower due to lower temperatures and less pressure solution, and changes in δ^{18} O can be large over small distances (Harwood et al., 2013; Hyodo et al., 2013).

In addition to $\Delta^{18}O(\text{early-late})$ values for single overgrowths, the differences between coexisting quartz and feldspar are calculated. Since the textural relations indicate feldspar precipitated first in most samples, the difference is calculated as $\Delta^{18}O(\text{OQ-OK}) = \delta^{18}O(\text{early})$ $O(\text{OQ-OK}) = \delta^{18}O(\text{late OK})$ for overgrowths that are within ~200 µm of each other. In cases where $\Delta^{18}O(\text{OQ-OK})$ values are calculated using overgrowths that contain only one analysis (29 out of 39 total overgrowth pairs), quartz overgrowths with only one spot are classified as early OQ and

feldspar overgrowths with only one spot are classified as late OK for the purposes of $\Delta^{18}O(OQ-OK)$ calculation. There is no systematic trend in $\Delta^{18}O(OQ-OK)$ with depth or rock unit with values ranging from 1.4 to 12 % (Fig. 2.7).

Discussion

Paragenesis

The textural relations for diagenetic quartz and feldspar described above indicate that feldspar predates or is contemporaneous with quartz in almost all samples studied. Early feldspar overgrowths tend to be thinner than quartz overgrowths from the same sample. Although growth rates of quartz and feldspar will be different and temperature has a large effect (Walderhaug, 1994), the thinner feldspar overgrowths qualitatively suggest that while feldspar grew first, the diagenetic feldspar period may have been relatively short lived compared to quartz. There was then a change in either dissolved components in the fluid or temperature that led to a change in dominant mineralization. This could be controlled by decreasing activity of aK/aH or aSiO_{2(aq)}, which may occur during early diagenesis (figure 3 of Worden and Burley, 2003), or an increase in aSiO_{2(aq)} as the degree of pressure solution increases.

After feldspar diagenesis, the consistent zoning seen with declining values of δ^{18} O in quartz overgrowths indicates that there was a prolonged period of punctuated or sustained quartz diagenesis. The duration of quartz cementation in sedimentary formations is a question that has been the subject of much study and disagreement (see discussion in Worden and Morad, 2000). Arguments have been made both for long-lived, continuous growth at slow rates (e.g., Walderhaug, 1990) and for pulsed or episodic rapid growth (e.g., Grant and Oxtoby, 1992). Studies of cementation in the Mt. Simon Ss of the Illinois Basin concluded that multiple episodes

of quartz precipitation over a relatively long period are responsible for the large overgrowths present (Fishman, 1997) and that cementation occurred early in the burial history, affecting the rock strength and brittle deformation potential of the unit (Makowitz et al., 2006). Geochemical studies of quartz overgrowths in the Mt. Simon Ss and Eau Claire Fm confirm that the period of quartz cementation in these units was prolonged, but cannot necessarily distinguish between a long, slow process or punctuated history (Pollington et al., 2011; Hyodo et al., 2013); Hyodo et al. (2013) show that there is at least qualitative evidence of episodes of growth. While previous studies have suggested a prolonged duration of quartz cementation based on textural relations, the combined textural and geochemical measurements of this and previous studies suggests that the total duration of quartz growth may have lasted as long as 200 million years (Fig. 2.8; Pollington et al., 2011; Hyodo et al., 2013). The feldspar and quartz diagenetic periods may overlap as seen by interfingering of the two phases (Fig. 2.3 C,D).

Previous studies have concluded that K-feldspar diagenesis throughout the Mt. Simon Ss was related to large-scale brine migration at elevated temperatures at ~400 Ma and that quartz diagenesis postdates this event (Duffin et al., 1989; Bethke and Marshak, 1990; Fishman, 1997; Chen et al., 2001). However, there is one sample in which diagenetic feldspar appears to postdate diagenetic quartz (Fig. 2.9). This sample is from the same core and depth as one that yielded a K-Ar age of 400 Ma (Duffin et al., 1989). Based on this single geochronologic measurement, and the textures seen for the majority of samples (OK before OQ), the sample that was used for geochronology is texturally distinctly different from the majority of samples described both in this study and by previous authors. In addition to these samples having diagenetic feldspar that postdates quartz diagenesis, there is no detrital feldspar; all the feldspar in rocks of this depth is diagenetic. This may be either be due to complete dissolution of all previous detrital Kfs, or that

all the potassium in this system was introduced to the rock. Either of these processes could have occurred in a localized hydrothermal system not seen in other rocks. The lack of detrital feldspar enabled measurements of Kfs age in bulk sample without mixing in detrital components, but may represent an age of diagenesis unrelated to that seen in the rest of the unit. We therefore propose that the 400 Ma age of Kfs diagenesis measured in the basal Mt. Simon Ss from a single sample is a separate mineralization event, possibly related to hydrothermal fluids, from that which formed the majority of the Kfs throughout the formation, which we interpret as occurring early in the burial history (Fig. 2.8).

Source of diagenetic components

Dissolution of detrital quartz either by pressure solution or by changes in fluid chemistry is a major source for silica in diagenetic quartz, even at relatively shallow burial depths (Stone and Siever, 1996; Pollington et al., 2011); similar processes may be responsible for the source of K and Al of diagenetic feldspar. Pressure solution of K-feldspar, particularly as a source of components for diagenetic mineralization, has been described from a location in Sweden (Friese et al., 2011). Pressure solution of detrital feldspars has also been observed in some samples of Mt. Simon in this study (Fig. 2.3 G, H).

The mineral chemistry of diagenetic feldspar, compared to that of adjacent detrital grains, has been used as an indicator of the localized source of dissolved cations (e.g., Kastner and Siever, 1979; Morad et al., 1989). The chemical compositions of both detrital grains and overgrowths from this study show that the feldspars in the Mt. Simon and Eau Claire formations are dominated by potassium-rich feldspar (Fig. 2.4, data repository Table DR2.3). Very little detrital plagioclase, and no diagenetic plagioclase, have been observed in this or previous studies

(cf., Odom, 1975). In terms of alkali component, the overgrowths have a composition of almost end-member potassium feldspar, while the detrital grains tend to have higher Na/K ratios (Fig. 2.4, Fig. 2.10B). Although the An content in all feldspars in this study is low,the correlation of Ca concentration between detrital grains and overgrowths (Fig. 2.5) is consistent with a local source of components for overgrowths. The highest Ca concentrations in detrital grains and correspondingly in overgrowths are in sandstone lenses within the fine-grained sediments of the Eau Claire Fm. One interpretation of this is that these lenses have remained as semi-isolated closed systems with no major input or removal of dissolved components. This would be expected hydrologically based on the very fine grain size of the surrounding mudstone. The similarity in chemistry between the detrital grains and overgrowths is consistent with the conclusion that the components necessary for the formation of the overgrowths were sourced by dissolution of the detrital grains.

Diagenetic temperatures

The majority of δ^{18} O values of detrital quartz and feldspar from both the Mt. Simon and Eau Claire formations are consistent with primary igneous source rocks (e.g., Taylor and Sheppard, 1986). The average detrital δ^{18} O of both minerals (Qz = 9.9‰, Kfs = 8.2‰) are similar in all the rocks studied regardless of location, depth or lithology. The range and pattern of δ^{18} O values in the quartz overgrowths from these two formations are interpreted as recording growth during heating due to burial, possibly with little to no change in δ^{18} O of the pore fluids (Pollington et al., 2011; Hyodo et al., 2013, this study). The systematic isotope zonation of single quartz overgrowths (Δ^{18} O(early-late-OQ)) was the critical evidence to interpret the changing temperature regime in which quartz precipitated. However, there is no distinguishable zonation

in feldspar overgrowths from the same samples (Δ^{18} O(early-late-OK) = 0‰), suggesting that individual feldspar overgrowths formed with no changes in either fluid chemistry or temperature, possibly over a shorter time frame.

Two end-member models can be constructed for interpreting the $\delta^{18}O$ values of feldspar overgrowths from the Mt. Simon and Eau Claire formations. Model (1) uses a constant temperature and calculates $\delta^{18}O(H_2O)$ values. Model (2) uses a constant $\delta^{18}O(H_2O)$ value of -3‰ (similar to early Paleozoic seawater; Came et al., 2007; Jaffres et al., 2007), and calculates diagenetic temperatures from measured $\delta^{18}O(OK)$. The models derived here for Kfs overgrowths are separate from, but must work in conjunction with, the quartz overgrowth models previously calculated for these formations (Pollington et al., 2011; Hyodo et al., 2013), in that textural evidence shows that feldspar predates or is contemporaneous with quartz, limiting the feldspar precipitation temperatures to equal to or lower than those of the quartz. Feldspar-quartz fractionation factors are calculated by combining fractionation factors of feldspar-quartz (Clayton et al., 1989) and quartz-water (Clayton et al., 1972, recalculated by Friedman and O'Neil, 1977). This same calibration is used in both models.

For model (1) the temperature is held constant and $\delta^{18}O(H_2O)$ is calculated from measured values of $\delta^{18}O$ for quartz and feldspar (Fig. 2.11A). This model was proposed by Chen et al. (2001) who concluded that feldspar and quartz overgrowths in the Mt. Simon Ss formed at 115°C and that pore fluids increased in $\delta^{18}O(H_2O)$ from the south to the north of the basin. As described in Pollington et al. (2011), the systematic trends in single overgrowths of quartz cannot be explained solely due to changing fluid composition and are more likely caused by changes in temperature. For model (1) if the feldspar precipitated at temperatures between 100 and 130°C as calculated from fluid inclusions in quartz (Fishman, 1997; Chen et al., 2001), and quartz

precipitated over a temperature range of >70°C as evidenced by systematic trends in single overgrowths (Pollington et al., 2011), then given the textural evidence of feldspar precipitating first, the temperatures of quartz precipitation would have reached values close to 200°C, which is considerably warmer than has been proposed for the central and northern Illinois Basin based on thermal modeling (Fishman, 1997; Rowan et al., 2002; Makowitz et al., 2006). Further, the values of $\delta^{18}O(H_2O)$ calculated for growth at a constant temperature of 115°C (as proposed by Chen et al., 2001) or even at 45°C (the lowest temperature calculated for quartz overgrowths in these samples, Pollington et al., 2011; Hyodo et al., 2013) are up to 15% higher than early Paleozoic seawater (\sim -5% to -1% Came et al., 2007; Jaffres et al., 2007). Such high $\delta^{18}O(H_2O)$ values in modern basins are interpreted to be remnants of formation fluids (Clayton et al., 1966) or to have been modified by reaction with overlying rocks along a flow path. Neither of these scenarios are likely to have been present early enough in the history of the rocks to have formed the feldspar overgrowths. The localized source of chemical components, along with the wide range of required $\delta^{18}O(H_2O)$ values suggest minimal fluid flow occurred in these samples. Model (1), therefore, cannot fully explain the observed $\delta^{18}O(OK)$ values.

For model (2) $\delta^{18}O(H_2O)$ is a constant value, and temperature is calculated from the measured $\delta^{18}O$ values of quartz and feldspar overgrowths. This model was proposed by Pollington et al. (2011) and Hyodo et al. (2013) for quartz overgrowths in the Illinois Basin who concluded that isotopic zonation of single overgrowths indicates long-lived growth during burial, pressure solution, and heating. The assumptions for thermal conditions of this model are that surface temperature was 20°C, burial proceeded in a geothermal gradient of 30°C/km and that there has been 1 km of uplift since the time of maximum burial. Using a $\delta^{18}O(H_2O)$ value of -3‰, average temperatures calculated from measured $\delta^{18}O(OK)$ values range from 20 to 60°C

and increase with depth (Fig. 2.11B). Although these temperatures are quite low, diagenetic feldspar precipitation has been reported at near-surface conditions of pressure and temperature (Stablein and Dapples, 1977; Waugh, 1978; Kastner and Siever, 1979; Ali and Turner, 1982). The highest temperature calculated for feldspar overgrowths at each depth is slightly higher than the lowest temperature calculated for diagenetic quartz (Pollington et al., 2011; Hyodo et al., 2013) in the same rock. The proposed history of mineralization in the samples studied is that feldspar overgrowths precipitated between 20 and 60°C, early in the burial history and that quartz overgrowths formed between 45 and 110°C (Pollington et al., 2011; Hyodo et al., 2013), partially overlapping temporally and thermally with feldspar precipitation.

Quartz-feldspar disequilibrium

The fractionation of $\delta^{18}O$ between quartz and K-feldspar ($\Delta^{18}O(Qz\text{-}Kfs)$) is a function of temperature if these minerals represent equilibrium. Equilibration could result if minerals precipitated from the same fluid at the same temperature. However, if the phases are not cogenetic, then the temperature is erroneous. Values of $\Delta^{18}O(OQ\text{-}OK)$ for the Mt. Simon and Eau Claire formations show that the two minerals are not in isotopic equilibrium with each other (Fig. 2.7). If we assume they may have been in equilibrium and calculate temperatures using the same feldspar-quartz fractionation used above (Clayton et al., 1989), the temperatures calculated range from 9° to 740°C with an average value of 230°C, which is higher than even the maximum temperature modeled for the hottest part of the basin (Makowitz et al., 2006). If the fluid composition over time was relatively constant as assumed in model (2) of the previous section, and quartz and feldspar precipitated at different temperatures, then the two phases precipitated in equilibrium with fluid of the same isotopic composition, but not in equilibrium with each other.

This is to be expected, given the textural relations indicating different generations of the two phases. The large discrepancy between equilibrium and measured $\Delta^{18}O(OQ-OK)$ is consistent with the Kfs precipitating early and Qz precipitating later at a higher temperature.

Continent-scale fluid flow

Flow of warm fluids through rocks across large sections of the mid-continent has been proposed as the cause of the Mississippi Valley Type (MVT) ore deposits, resetting of paleomagnetism, petroleum migration and K-metasomatism that are observed throughout central North America (e.g., Bethke and Marshak, 1990). These fluid flow regimes are interpreted to be dominated by topographically driven flow of fluids, from uplifting tectonic belts through sedimentary basins. In this study we have shown that the majority of feldspar in the lowest Cambrian sediments of the Illinois Basin precipitated early in the burial history, possibly soon after deposition. Temperatures of formation for the majority of diagenetic feldspar in these units reflect growth at temperatures much lower than those proposed for ore-forming fluids (75-150°C Sverjensky, 1986). These two results suggest that most of the diagenetic feldspar in the Mt. Simon Ss and the Eau Claire Fm is unrelated to topographically driven fluid flow and we propose an earlier, previously undescribed, period of K-feldspar precipitation.

Conclusions

1. Textural relations show euhedral and subhedral feldspar overgrowths with abutting quartz overgrowths. Quartz and feldspar overgrowths formed at different times in the history of the Mt. Simon and Eau Claire formations, with feldspar predating quartz in most samples studied.

- 2. Average $\delta^{18}O$ values of detrital feldspar (8.2‰) and quartz (9.9‰) grains are consistent with dominantly igneous source rocks. The $\delta^{18}O$ values of both detrital phases are independent of lithology or burial depth.
- 3. In situ microanalysis of δ^{18} O of diagenetic feldspar reveals low temperature mineralization conditions early in the burial history of the Illinois Basin and the integrated feldspar and quartz overgrowth records provide a more complete history of diagenesis in the Illinois Basin than study of either phase individually, particularly early in the burial history of the two formations.
- 4. If fluids were similar in $\delta^{18}O$ to Cambrian seawater ($\delta^{18}O = -3\%$) then the $\delta^{18}O$ values of feldspar overgrowths from the Mt. Simon and Eau Claire formations represent growth at relatively low temperatures (20-60°C) before quartz that formed between 45 and 110°C.
- 5. Modeled low temperature precipitation and early textures of diagenetic feldspar show that the majority of feldspar diagenesis in the Mt. Simon and Eau Claire formations is unrelated to continent-scale fluid flow and resulted from an earlier period of K-feldspar diagenesis in these rocks.

Acknowledgements

The WiscSIMS laboratory is supervised by Noriko Kita and maintained by Jim Kern. Brian Hess prepared sample mounts. Mike Spicuzza assisted in analyses of feldspar standards. Ellen Syracuse assisted in drafting figures. Dave Morse, Sallie Greenberg, Jared Freiburg, and Robert Mumm of the Illinois Geological Survey provided Illinois samples; Dave Hart of the Wisconsin Geological and Natural History Survey and Wasinee Aswasereelert provided Wisconsin samples. Samples ADM CCS #1 were supplied by the Midwest Geological Sequestration Consortium. This project was funded by DOE (93ER14389) and University of Wisconsin-Madison Department of Geoscience. The WiscSIMS laboratory is partially funded by NSF (EAR-0319230, 1053466).

References

- Ali, A.D., and Turner, P., 1982, Authigenic K-Feldspar in the Bromsgrove Sandstone Formation (Triassic) of Central England: Journal of Sedimentary Petrology, v. 52, p. 187-198.
- Aswasereelert, W., Simo, J.A., and LePain, D.L., 2008, Deposition of the Cambrian Eau Claire Formation, Wisconsin: Hydrostratigraphic implications of fine-grained cratonic sandstones: Geoscience Wisconsin, v. 19, p. 1-21.
- Bethke, C.M., and Marshak, S., 1990, Brine Migrations across North-America the Plate-Tectonics of Groundwater: Annual Review of Earth and Planetary Sciences, v. 18, p. 287-315.
- Bowen, B.B., Ochoa, R.I., Wilkens, N.D., Brophy, J., Lovell, T.R., Fischietto, N., Medina, C.R., and Rupp, J.A., 2011, Depositional and diagenetic variability within the Cambrian Mount Simon Sandstone; implications for carbon dioxide sequestration: Environmental Geosciences, v. 18, p. 69-89.
- Buschbach, T.C., and Kolata, D.R., 1990, Regional setting of the Illinois Basin, *in* Leighton, M.W., Kolata, D.R., Oltz, D.F., and Eidel, J.J., eds., Interior cratonic basins: AAPG Memoir 51 51: Tulsa, OK, American Association of Petroleum Geologists, p. 29-55.
- Came, R.E., Eiler, J.M., Veizer, J., Azmy, K., Brand, U., and Weidman, C.R., 2007, Coupling of surface temperatures and atmospheric CO₂ concentrations during the Palaeozoic era: Nature, v. 449, p. 198-201.
- Chen, Z.S., Riciputi, L.R., Mora, C.I., and Fishman, N.S., 2001, Regional fluid migration in the Illinois Basin: Evidence from *in situ* oxygen isotope analysis of authigenic K-feldspar and quartz from the Mount Simon Sandstone: Geology, v. 29, p. 1067-1070.
- Clayton, R.N., Friedman, I., Graf, D.L., Mayeda, T.K., Meents, W.F., and Shimp, N.F., 1966, Origin of Saline Formation Waters .1. Isotopic Composition: Journal of Geophysical Research, v. 71, p. 3869-3882.
- Clayton, R.N., Mayeda, T.K., and O'Neil, J.R., 1972, Oxygen Isotope-Exchange between Quartz and Water: Journal of Geophysical Research, v. 77, p. 3057-3067.
- Clayton, R.N., Goldsmith, J.R., and Mayeda, T.K., 1989, Oxygen Isotope Fractionation in Quartz, Albite, Anorthite and Calcite: Geochimica et Cosmochimica Acta, v. 53, p. 725-733.
- Distefano, M., 1973, The mineralogy and petrology of the Eau Claire Formation, west-central Wisconsin [M. S. thesis]: De Kalb, IL, Northern Illinois University.
- Driese, S.G., Byers, C.W., and Dott, R.H., 1981, Tidal Deposition in the Basal Upper Cambrian Mt Simon Formation in Wisconsin: Journal of Sedimentary Petrology, v. 51, p. 367-381.
- Duffin, M.E., 1989, Nature and Origin of Authigenic K-Feldspar in Precambrian Basement Rocks of the North-American Midcontinent: Geology, v. 17, p. 765-768.
- Duffin, M.E., Lee, M.C., Klein, G.D., and Hay, R.L., 1989, Potassic Diagenesis of Cambrian Sandstones and Precambrian Granitic Basement in UPH-3 Deep Hole, Upper Mississippi Valley, USA: Journal of Sedimentary Petrology, v. 59, p. 848-861.

- Fischietto, N.E., 2009, Lithofacies and depositional environments of the Cambrian Mount Simon Sandstone in the northern Illinois Basin: Implications for carbon dioxide sequestration [M. S. thesis]: United States -- Indiana, Purdue University.
- Fishman, N.S., 1997, Basin-wide fluid movement in a Cambrian paleoaquifer: evidence from the Mt. Simon Sandstone, Illinois and Indiana, *in* Montañez, I.P., Gregg, J.M., and Shelton, K.L., eds., Basin-wide diagenetic patterns; integrated petrologic, geochemical, and hydrologic consideration, Volume 57: SEPM Special Publications Journal Article: United States (USA), SEPM (Society for Sedimentary Geology), Tulsa, OK, United States (USA), p. 221-234.
- Friedman, I., and O'Neil, J.R., 1977, Compilation of stable isotope fractionation factors of geochemical interest: United States Geological Survey professional paper 440-KK, Washington, D.C., 67 p.
- Friese, N., Vollbrecht, A., Leiss, B., and Jacke, O., 2011, Cambrian sedimentary dykes in the Proterozoic basement of the Vastervik area (southeast Sweden): episodic formation inferred from macro- and microfabrics: International Journal of Earth Sciences, v. 100, p. 741-752.
- Graham, C.M., Valley, J.W., and Winter, B.L., 1996, Ion microprobe analysis of ¹⁸O/¹⁶O in authigenic and detrital quartz in the St Peter Sandstone, Michigan Basin and Wisconsin Arch, USA: Contrasting diagenetic histories: Geochimica et Cosmochimica Acta, v. 60, p. 5101-5116.
- Grant, S.M., and Oxtoby, N.H., 1992, The Timing of Quartz Cementation in Mesozoic Sandstones from Haltenbanken, Offshore Mid-Norway Fluid Inclusion Evidence: Journal of the Geological Society, v. 149, p. 479-482.
- Hagadorn, J.W., Dott, R.H., and Damrow, D., 2002, Stranded on a Late Cambrian shoreline: Medusae from central Wisconsin: Geology, v. 30, p. 147-150.
- Harwood, J., Aplin, A.C., Fialips, C.I.M., Iliffe, J.E., Kozdon, R., Ushikubo, T., and Valley, J.W., 2013, Quartz cementation history of sandstones revealed by high resolution SIMS oxygen isotope analysis: Journal of Sedimentary Research, v. 83, p. 522-530.
- Hay, R.L., Lee, M.C., Kolata, D.R., Matthews, J.C., and Morton, J.P., 1988, Episodic Potassic Diagenesis of Ordovician Tuffs in the Mississippi Valley Area: Geology, v. 16, p. 743-747.
- Hervig, R.L., Williams, L.B., Kirkland, I.K., and Longstaffe, F.J., 1995, Oxygen isotope microanalyses of diagenetic quartz: Possible low temperature occlusion of pores: Geochimica et Cosmochimica Acta, v. 59, p. 2537-2543.
- Hoholick, J.D., Metarko, T., and Potter, P.E., 1984, Regional Variations of Porosity and Cement St-Peter and Mount Simon Sandstones in Illinois Basin: AAPG Bulletin, v. 68, p. 753-764.
- Hyodo, A., Kozdon, R., Pollington, A.D., and Valley, J.W., in prep., Evolution of quartz cementation and burial history of the Eau Claire Formation based on *in situ* oxygen isotope analysis of quartz overgrowths.

- Jaffres, J.B.D., Shields, G.A., and Wallmann, K., 2007, The oxygen isotope evolution of seawater: A critical review of a long-standing controversy and an improved geological water cycle model for the past 3.4 billion years: Earth-Science Reviews, v. 83, p. 83-122.
- Kastner, M., and Siever, R., 1979, Low Temperature Feldspars in Sedimentary Rocks: American Journal of Science, v. 279, p. 435-479.
- Kelly, J.L., Fu, B., Kita, N.T., and Valley, J.W., 2007, Optically continuous silcrete quartz cements of the St. Peter Sandstone: High precision oxygen isotope analysis by ion microprobe: Geochimica et Cosmochimica Acta, v. 71, p. 3812-3832.
- Kita, N.T., Ushikubo, T., Fu, B., and Valley, J.W., 2009, High precision SIMS oxygen isotope analysis and the effect of sample topography: Chemical Geology, v. 264, p. 43-57.
- Kuiper, K.F., Deino, A., Hilgen, F.J., Krijgsman, W., Renne, P.R., and Wijbrans, J.R., 2008, Synchronizing rock clocks of Earth history: Science, v. 320, p. 500-504.
- Land, L.S., and Milliken, K.L., 1981, Feldspar Diagenesis in the Frio Formation, Brazoria County, Texas Gulf-Coast: Geology, v. 9, p. 314-318.
- Lawrence, J.R., and Kastner, M., 1975, O¹⁸/O¹⁶ of Feldspars in Carbonate Rocks: Geochimica et Cosmochimica Acta, v. 39, p. 97-102.
- Leetaru, H.E., and McBride, J.H., 2009, Reservoir uncertainty, Precambrian topography, and carbon sequestration in the Mt. Simon Sandstone, Illinois Basin: Environmental Geosciences, v. 16, p. 235-243.
- Lyon, I.C., Burley, S.D., McKeever, P.J., Saxton, J.M., and Macaulay, C., 2000, Oxygen isotope analysis of authigenic quartz in sandstones: a comparison of ion microprobe and conventional analytical techniques, *in* Worden, R., and Morad, S., eds., Quartz cemenation in sandstones: International Association of Sedimentologists Special publication 29: Malden, MA, Blackwell Science, p. 299-316.
- Macaulay, C.I., Fallick, A.E., Haszeldine, R.S., and Graham, C.M., 2000, Methods of laser-based stable isotope measurement applied to diagenetic cements and hydrocarbon reservoir quality: Clay Minerals, v. 35, p. 313-322.
- Mai, H., and Dott, J., R. H., 1985, A subsurface study of the St. Peter Sandstone in southern and eastern Wisconsin: Wisconsin Geological and Natural History Survey Information Circular 47, 26 p.
- Makowitz, A., Lander, R.H., and Milliken, K.L., 2006, Diagenetic modeling to assess the relative timing of quartz cementation and brittle grain process during compaction: AAPG Bulletin, v. 90, p. 873-885.
- Marchand, A.M.E., Macaulay, C.I., Haszeldine, R.S., and Fallick, A.E., 2002, Pore water evolution in oilfield sandstones: constraints from oxygen isotope microanalyses of quartz cement: Chemical Geology, v. 191, p. 285-304.
- Morad, S., Marfil, R., and Delapena, J.A., 1989, Diagenetic K-Feldspar Pseudomorphs in the Triassic Buntsandstein Sandstones of the Iberian Range, Spain: Sedimentology, v. 36, p. 635-650.

- Morrison, B.C., 1968, Stratigraphy of the Eau Claire Formation (Upper Cambrian) of west-central Wisconsin [M. S. thesis]: Madison, WI, University of Wisconsin-Madison.
- Neufelder, R.J., Bowen, B.B., Lahann, R.W., and Rupp, J.A., 2012, Lithologic, mineralogical, and petrophysical characteristics of the Eau Claire Formation: Complexities of a carbon storage system seal: Environmental Geosciences, v. 19, p. 81-104.
- Odom, I.E., 1975, Feldspar-grain size relations in Cambrian arenites, upper Mississippi Valley: Journal of Sedimentary Research, v. 45, p. 636-650.
- Page, F.Z., Ushikubo, T., Kita, N.T., Riciputi, L.R., and Valley, J.W., 2007, High-precision oxygen isotope analysis of picogram samples reveals 2 μm gradients and slow diffusion in zircon: American Mineralogist, v. 92, p. 1772-1775.
- Page, F.Z., Kita, N.T., and Valley, J.W., 2010, Ion microprobe analysis of oxygen isotopes in garnets of complex chemistry: Chemical Geology, v. 270, p. 9-19.
- Pollington, A.D., Kozdon, R., and Valley, J.W., 2011, Evolution of quartz cementation during burial of the Cambrian Mount Simon Sandstone, Illinois Basin: *In situ* microanalysis of δ^{18} O: Geology, v. 39, p. 1119-1122.
- Renne, P.R., Swisher, C.C., Deino, A.L., Karner, D.B., Owens, T.L., and DePaolo, D.J., 1998, Intercalibration of standards, absolute ages and uncertainties in Ar-40/Ar-39 dating: Chemical Geology, v. 145, p. 117-152.
- Rowan, E.L., Goldhaber, M.B., and Hatch, J.R., 2002, Regional fluid flow as a factor in the thermal history of the Illinois basin: Constraints from fluid inclusions and the maturity of Pennsylvanian coals: AAPG Bulletin, v. 86, p. 257-277.
- Savin, S.M., and Epstein, S., 1970, Oxygen Isotopic Compositions of Coarse Grained Sedimentary Rocks and Minerals: Geochimica et Cosmochimica Acta, v. 34, p. 323-329.
- Shieh, Y.N., 1983, Oxygen Isotope Study of Precambrian Granites from the Illinois-Deep-Hole-Project: Journal of Geophysical Research, v. 88, p. 7300-7304.
- Sloss, L.L., 1963, Sequences in the Cratonic Interior of North America: Geological Society of America Bulletin, v. 74, p. 93-114.
- Stablein, N.K., and Dapples, E.C., 1977, Feldspars of Tunnel City Group (Cambrian), Western Wisconsin: Journal of Sedimentary Petrology, v. 47, p. 1512-1538.
- Stallard, M.L., and Boles, J.R., 1989, Oxygen Isotope Measurements of Albite-Quartz-Zeolite Mineral Assemblages, Hokonui Hills, Southland, New-Zealand: Clays and Clay Minerals, v. 37, p. 409-418.
- Stone, W.N., and Siever, R., 1996, Quantifying compaction, pressure solution and quartz cementation in moderately- and deeply-buried quartzose sandstones from the Greater Green River Basin, Wyoming, *in* Crossey, L.J., Loucks, R., and Totten, M.W., eds., Siliciclastic diagenesis and fluid flow: Concepts and applications: SEPM Special Publication 55, SEPM (Society for Sedimentary Geology), p. 129-150.
- Sverjensky, D.A., 1986, Genesis of Mississippi Valley Type Lead-Zinc Deposits: Annual Review of Earth and Planetary Sciences, v. 14, p. 177-199.

- Taylor, H.P., and Sheppard, S.M.F., 1986, Igneous rocks: 1. Processes of isotopic fractionation and isotope systematics, *in* Valley, J.W., Taylor, H.P., Jr., and O'Neil, J.R., eds., Stable isotopes in high temperature geological processes, Volume 16: Reviews in Mineralogy, p. 227-271.
- Templeton, J.S., Jr., 1951, The Mt. Simon Sandstone in Northern Illinois: Illinois Geological Survey Circular, v. 170, p. 151-159.
- Valley, J.W., and Kita, N.T., 2009, *In situ* oxygen isotope geochemistry by ion microprobe, *in* Fayek, M., ed., Secondary Ion Mass Spectrometry in the Earth Sciences: Gleaning the big picture from a small spot: Short Course Series 41, Mineralogical Association of Canada, p. 19-63.
- Walcott, C.D., 1914, Cambrian geology and paleontology: Smithsonian Miscellaneous Collection, City of Washington, Smithsonian Institution, 412 p.
- Walderhaug, O., 1990, A Fluid Inclusion Study of Quartz-Cemented Sandstones from Offshore Mid-Norway Possible Evidence for Continued Quartz Cementation during Oil Emplacement: Journal of Sedimentary Petrology, v. 60, p. 203-210.
- Walderhaug, O., 1994, Precipitation Rates for Quartz Cement in Sandstones Determined by Fluid-Inclusion Microthermometry and Temperature-History Modeling: Journal of Sedimentary Research Section a-Sedimentary Petrology and Processes, v. 64, p. 324-333.
- Waugh, B., 1978, Authigenic K-feldspar in British Permo-Triassic sandstones: Journal of the Geological Society of London, v. 135, Part 1, p. 51-56.
- Williams, L.B., Hervig, R.L., and Bjorlykke, K., 1997, New evidence for the origin of quartz cements in hydrocarbon reservoirs revealed by oxygen isotope microanalyses: Geochimica et Cosmochimica Acta, v. 61, p. 2529-2538.
- Willman, H.B., Atherton, E., Buschbach, T.C., Collinson, C., Frye, J.C., Hopkins, M.E., Lineback, J.A., and Simon, J.A., 1975, Handbook of Illinois stratigraphy: Illinois State Geological Survey Bulletin, 261 p.
- Worden, R.H., and Morad, S., 2000, Quartz cementation in oil field sandstones: a review of the key controversies, *in* Worden, R., and Morad, S., eds., Quartz cementation in sandstones: International Association of Sedimentologists Special publication 29: Malden, MA, Blackwell Science, p. 1-20.
- Worden, R.H., and Burley, S.D., 2003, Sandstone diagenesis: the evolution of sand to stone, *in* Burley, S.D., and Worden, R.H., eds., Sandstone Diagenesis: Recent and Ancient: Reprint series of the International Association of Sedimentologists 4, Blackwell Publishing, p. 3-44.

Figures

Figure 2.1. Location map of samples used in this study. Sample locations are labeled with core ID numbers (Table 2.1). Dashed lines represent approximate boundaries of Illinois and Michigan Basins; locations of structural features are from Buschbach and Kolata (1990).

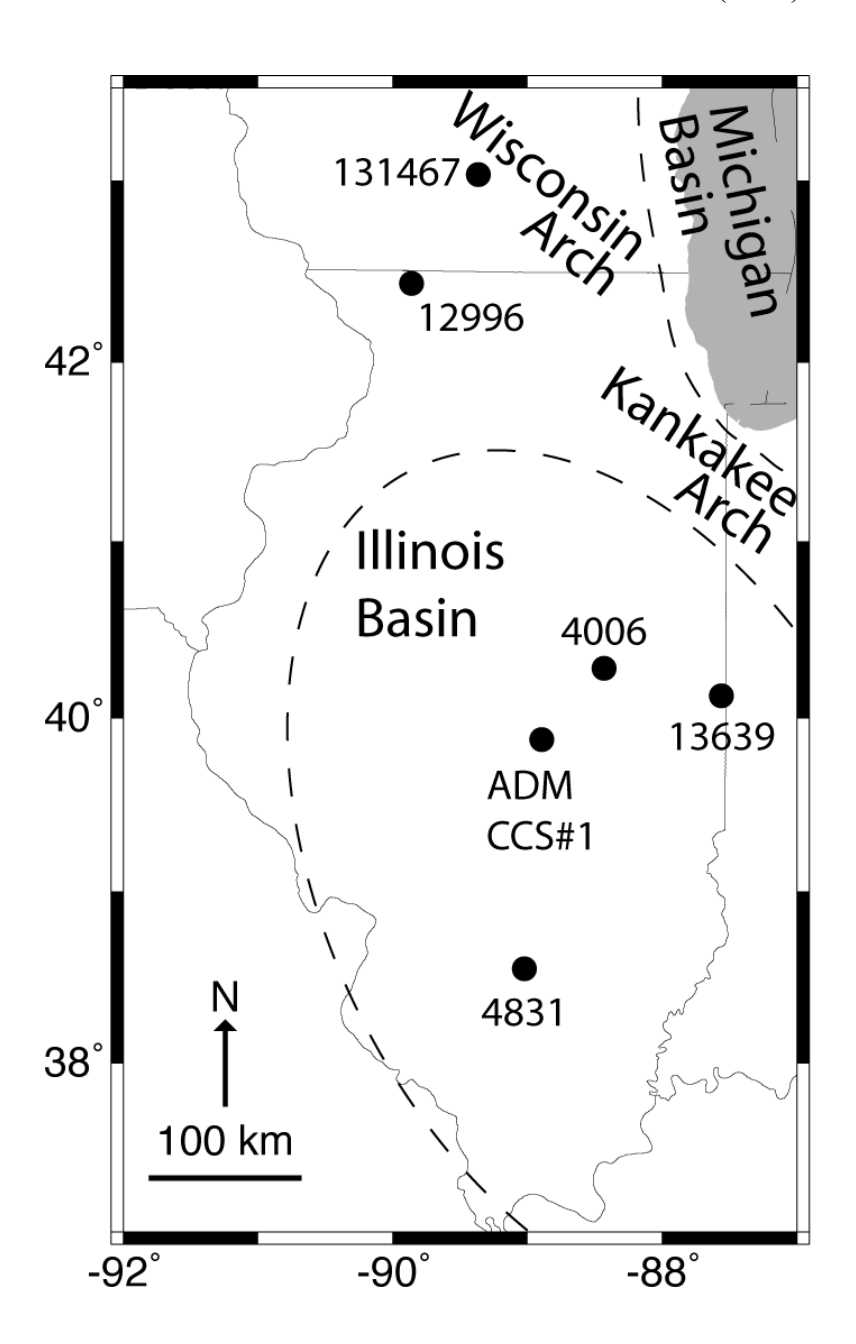
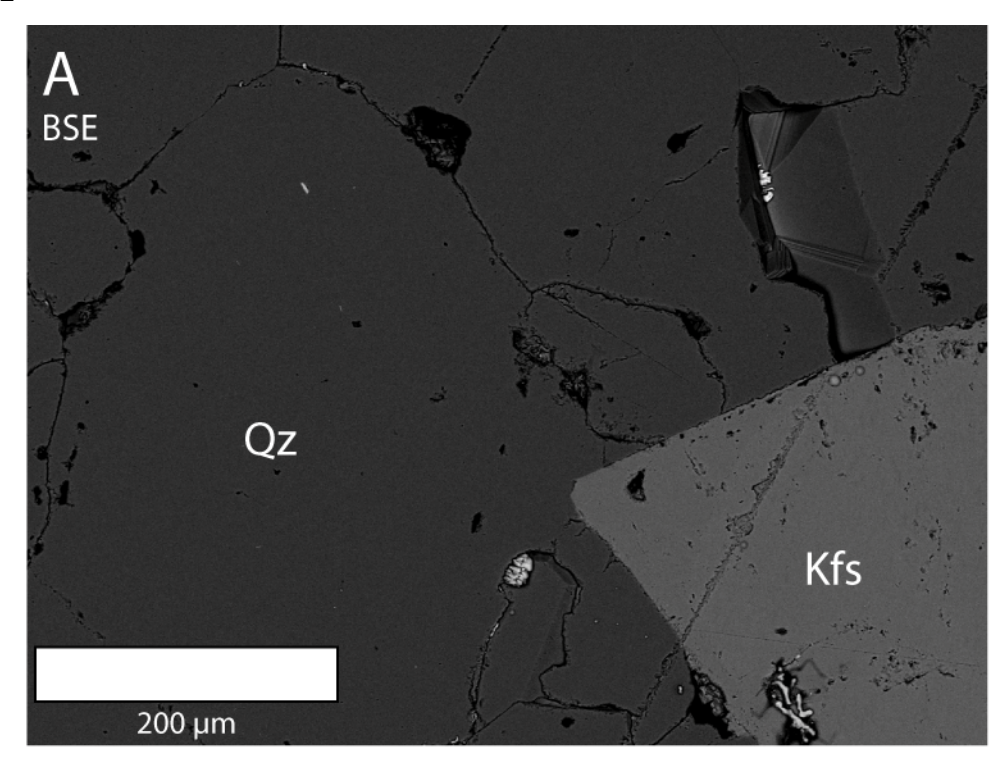


Figure 2.2 (next page). SEM photomicrographs showing differences between detrital and diagenetic phases; 09IL-35; 1876 m; Mt. Simon Ss. Abbreviations: Qz = quartz; Kfs = K-feldspar; DQ = detrital quartz; OQ = overgrowth quartz; OK = overgrowth K-feldspar; DK = detrital K-feldspar. (A) Backscattered electron (BSE) image; quartz and feldspar are distinct in backscattered response. (B) Cathodoluminescence (CL) image of same area; overgrowths can be distinguished from rounded, detrital grains. Differences in CL response in overgrowths reflect slight changes in trace element chemistry.

Figure 2.2



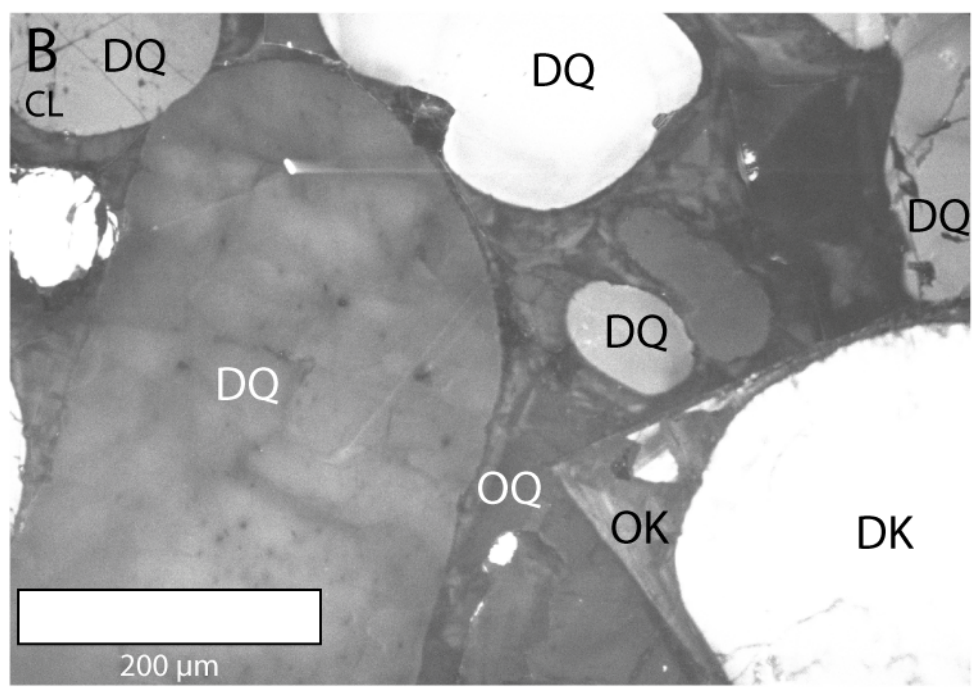


Figure 2.3 (next page). SEM photomicrographs of diagenetic textures in the Mt. Simon Ss. Abbreviations: Qz = quartz; Kfs = K-feldspar; DQ = detrital quartz; QQ = overgrowth quartz; OK = overgrowth K-feldspar; DK = detrital K-feldspar; P = pore space. (A, C, E, G) Backscattered electron images. (B, D, F, H) Cathodoluminescence images. (A, B) Euhedral overgrowth of feldspar with later overgrowth quartz terminating against feldspar (open arrows); feldspar overgrowth abutting detrital quartz grain indicating early timing of feldspar growth with respect to quartz (filled arrow); since the feldspar overgrowth abuts the detrital quartz grain, it must have formed before the quartz overgrowth formed. Note crystallographically oriented dissolution of detrital feldspar grain but not of overgrowth feldspar; 09IL-35; 1876 m. (C, D) Interfingering of overgrowths of quartz and feldspar possibly showing cogenetic growth of diagenetic phases, or possible early growth of feldspar with later quartz infilling (arrow); 09IL-6; 434 m. (E, F) Thin overgrowth of quartz with abutting feldspar overgrowth indicating short duration of early quartz growth (open arrow); grain-to-grain contacts indicative of quartz pressure solution (solid arrows); 09IL-39; 1981 m. (G, H) Grain-to-grain pressure solution along detrital grain contacts between two detrital quartz grains (open arrow); flat line contact between detrital quartz and detrital feldspar (filled arrow); 09IL-41; 1982 m.

Figure 2.3

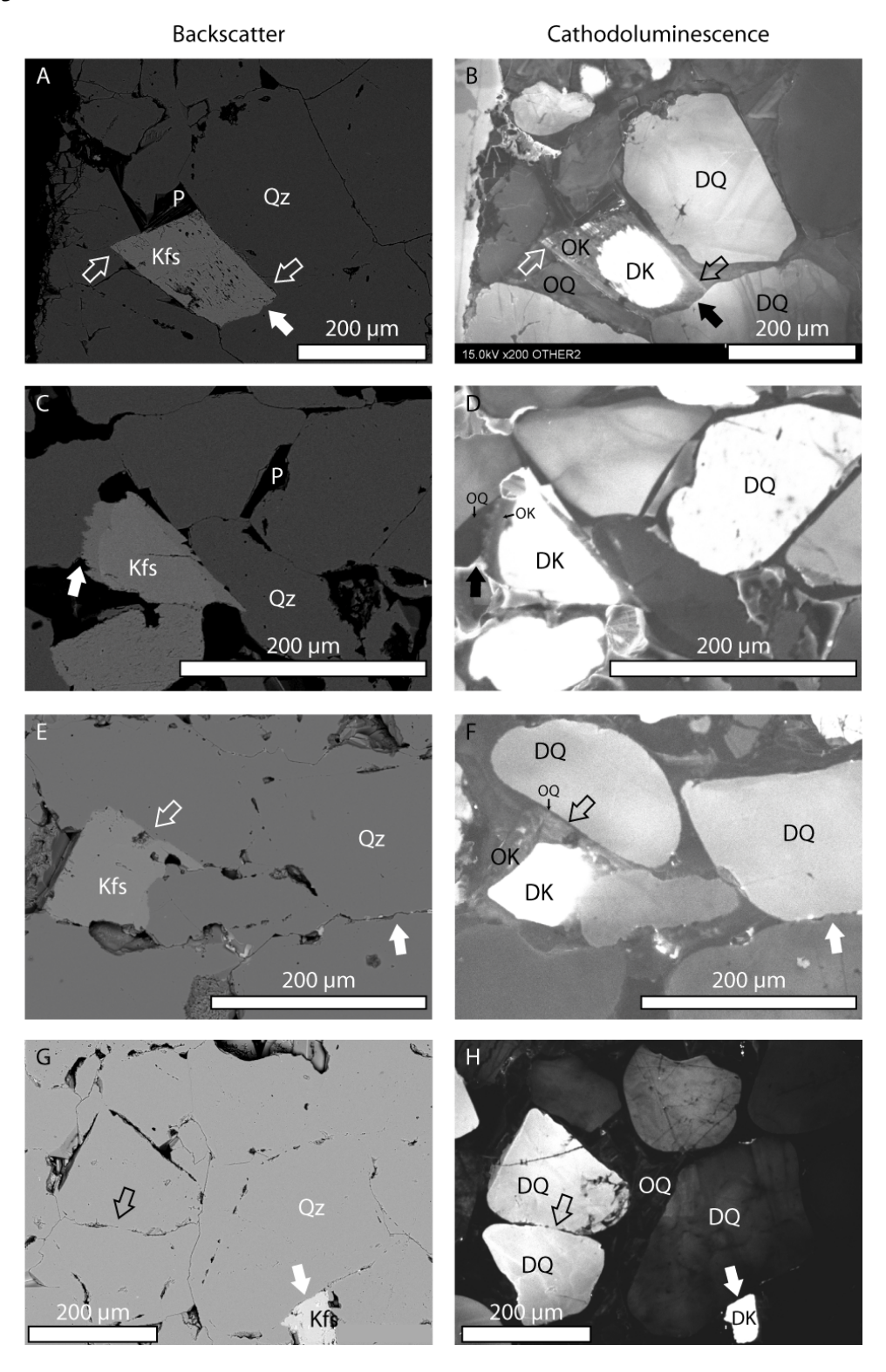


Figure 2.4. Ternary diagrams of clastic and diagenetic feldspar compositions for each formation and sample type. Abbreviations: Kfs = K-feldspar; Ab = albite; An = anorthite; EC = Eau Claire; MS = Mt. Simon; DK = detrital Kfs; OK = overgrowth Kfs. Note scale is 80 to 100% Kfs mol% on all diagrams. Inset shows full ternary diagram with area plotted in sample ternary diagrams shaded. Overgrowths from a given formation are more Kfs rich than the detrital grains from that formation; overgrowths from the Eau Claire Fm are more An rich than those from the Mt. Simon Ss.

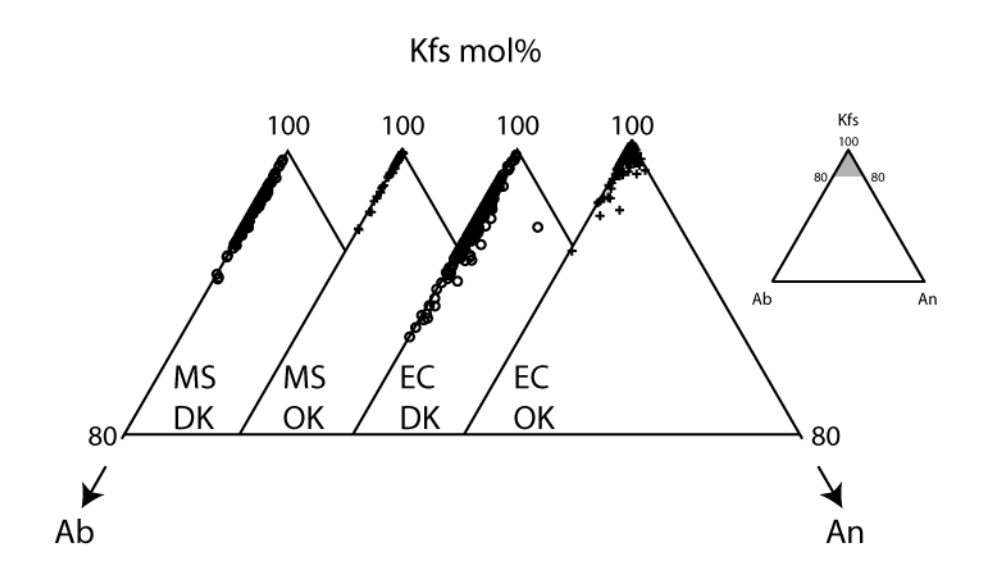


Figure 2.5. Crossplot of maximum anorthite content per rock between detrital and diagenetic feldspar. Abbreviations: EC = Eau Claire Fm; MS = Mt. Simon Ss; An=anorthite. While An is a minor component of these feldspars, strong positive correlation, particularly in samples of the Eau Claire Fm, suggests that the components of the overgrowths are locally derived from solution of detrital grains. See also appendix Figure A2.3.

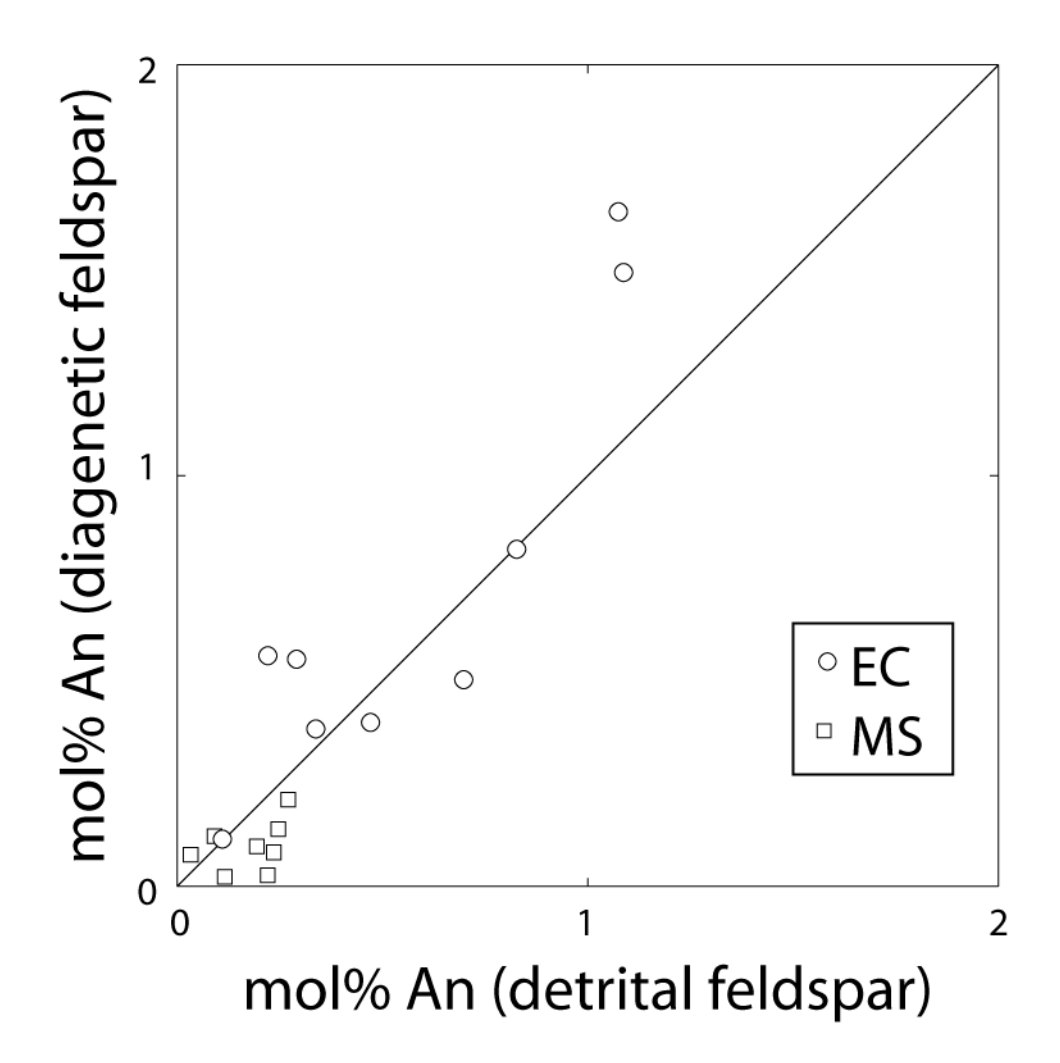


Figure 2.6 (next page). Depth vs. δ^{18} O of quartz and feldspar from 17 samples of the Mt. Simon and Eau Claire formations in the Illinois Basin. Quartz data (grey crosses) are from Pollington et al. (2011), Hyodo et al. (2013) and this study; feldspar data (black circles) are from this study. Abbreviations: Kfs=K-feldspar; Qz = quartz. (A) Detrital grains average $\delta^{18}O(Qz) = 9.9$ % and $\delta^{18}O(Kfs) = 8.2$ %, consistent with a dominantly igneous origin. (B) Diagenetic values; $\delta^{18}O$ values from quartz overgrowths in both the Mt. Simon and Eau Claire formations show a trend to lower values and wider ranges with increasing depth in the basin; diagenetic feldspar δ^{18} O values also decrease with increasing depth but have a narrower range. Grey dashed lines are calculated for quartz in equilibrium with $\delta^{18}O(H_2O) = -3\%$: The straight dashed line is for a constant temperature of 45°C and the curved line is for varying temperature. The curved grey line represents the $\delta^{18}O(OO)$ value for quartz precipitated in a geothermal gradient of 30°C/km. assuming 1 km of late uplift and 20°C surface temperature (see text). These curves encompass the range of $\delta^{18}O(OQ)$ values measured. The black lines are calculated values of $\delta^{18}O(OK)$ in equilibrium with $\delta^{18}O(H_2O) = -3\%$; the vertical black line is calculated for 20°C and the curved line assumes the same model geotherm (30°C/km) as the curved grey line for quartz. Note that the measured $\delta^{18}O(OK)$ values do not fit the curves calculated for feldspar in equilibrium with quartz in this model. This suggests that OK precipitated at cooler temperatures than OO in these samples (see text). (C) Δ^{18} O(early-late) values for traverses of individual quartz and feldspar overgrowths. The wide range of Δ^{18} O(early-late-Qz) values reflects growth during burial and heating. The Δ^{18} O(early-late-Kfs) values are almost all within error of 0% indicating no zonation and consequently no change in temperature or fluid composition. See text for discussion.

Figure 2.6

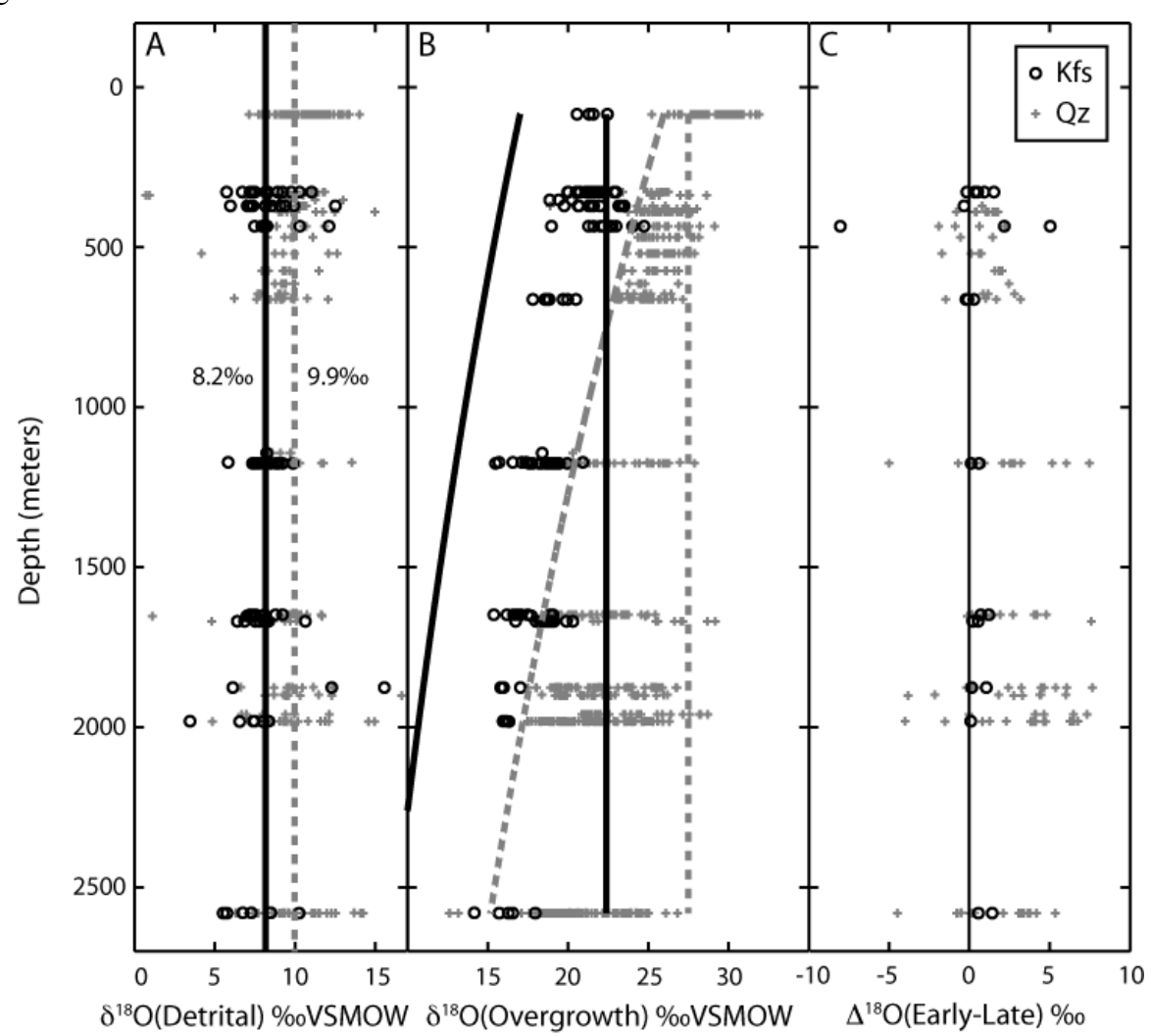


Figure 2.7 (next page). Depth vs. $\Delta^{18}O(\text{quartz-feldspar})$. (A) measured $\Delta^{18}O(\text{OQ-OK})$ values from analyses of earliest domains of touching quartz and feldspar overgrowths. See text for discussion of $\Delta^{18}O(\text{OQ-OK})$ calculation. EC=Eau Claire Fm, MS= Mt. Simon Ss. Curved line represents the equilibrium fractionation (Clayton et al., 1989) between the two phases in the same temperature vs. depth model as Figure 2.6B. The majority of measured $\Delta^{18}O(\text{OQ-OK})$ values are smaller than the equilibrium value (29 of 39 measured pairs). This is consistent with the interpretation that quartz precipitated later, at higher temperatures, than feldspar.

Figure 2.7

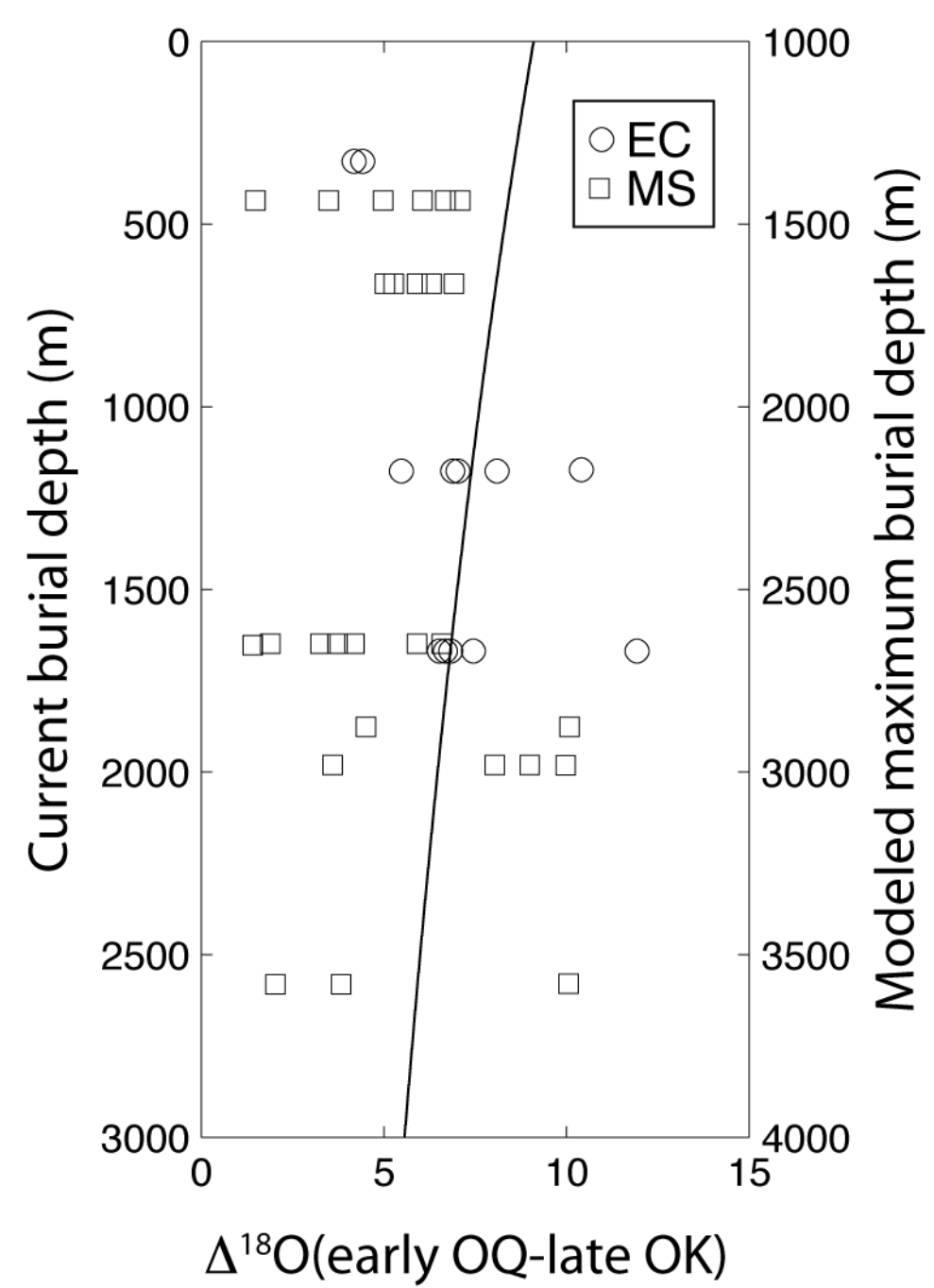
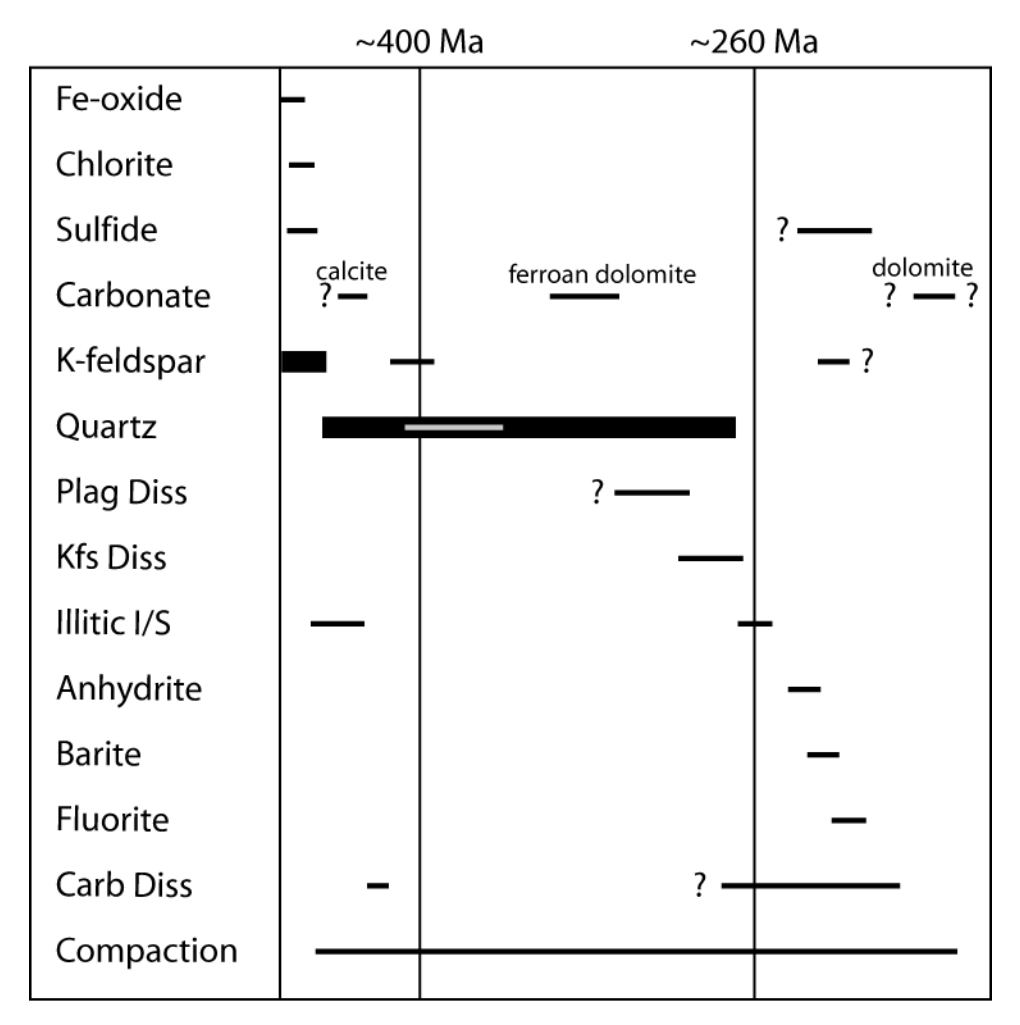


Figure 2.8 (next page). Relative timing of diagenetic events in the Mt. Simon Ss. Plag=plagioclase; Kfs=K-feldspar; Diss=dissolution; Carb=carbonate. Events are precipitation of a given mineral unless noted. Ages of Kfs and illitic I/S (illite/smectite) are from Duffin et al. (1989); quartz precipitation is interpreted to begin at ~450 Ma by Hyodo et al. (2013). Thick lines are from this study, thin lines and phase identifications are from Fishman (1997). The timing and duration of Kfs and Qz precipitation was largely constrained by a single 400 Ma age on diagenetic feldspar and textural relationships from other rocks. However, the sample from which this age is derived has a distinctly different textural relationship between OK and OQ than other rocks described in this and other studies (see text). The long duration of quartz precipitation presented in this Figure is based on discussion in Hyodo et al. (2013). Diagram modified from Fishman (1997).

Figure 2.8



Time —

Figure 2.9 (next page). Photomicrographs showing late K-feldspar of an anomalous sample; 09IL-29; 663 m; Mt. Simon Ss. Abbreviations: Kfs=K-feldspar; P=porosity; D=quartz dissolution; Qz=quartz; OK=overgrowth K-feldspar; OQ=overgrowth quartz; DQ=detrital quartz. (A) Backscattered electron (BSE) image. K-feldspar, quartz and porosity (epoxy) are easily distinguishable in BSE. (B) Cathodoluminescence (CL) image of same area shown in (A). Detrital and diagenetic phases are distinguishable by CL response. Diagenetic quartz is euhedral, with diagenetic Kfs apparently precipitating later and growing to termination against OQ (solid arrow in both panels). Overgrowth quartz in this area is precipitated on a rounded detrital grain, whereas there is no visible detrital Kfs. Porosity at the DQ-OQ boundary is not generally observed in other samples; perhaps this is related to leaching during hydrothermal precipitation of Kfs. Dissolution of quartz along the pore wall (secondary porosity) is also present in this image; dissolution crosscuts the OQ-DQ boundary (dashed arrow in both panels). Two five-μm SIMS pits are visible in OQ and OK in both panels (right of solid arrow).

Figure 2.9

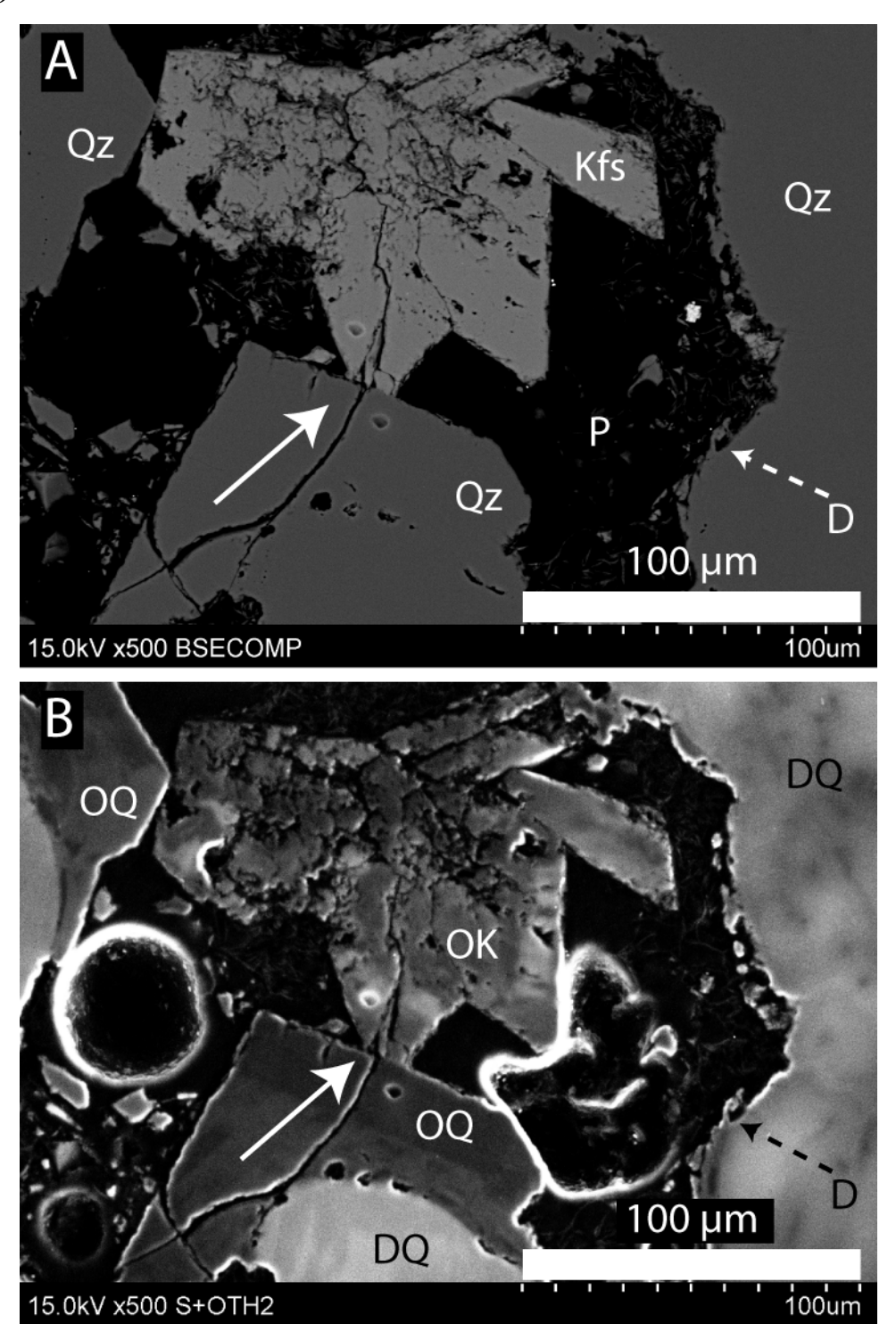


Figure 2.10. Crossplot of Na/K ratio based on formula atoms between paired detrital and overgrowth feldspars. EC=Eau Claire Fm, MS=Mt. Simon Ss. The line is a 1:1 line; points below the line indicate that the detrital grain has a higher ratio of given elements than the adjoining overgrowth, points above the line indicate that the overgrowth has a higher ratio of those elements than the detrital grain on which it grew. Most of the grains studied have more K in the overgrowths than in the detrital grains. This is reflected in higher Na/K values in detrital grains.

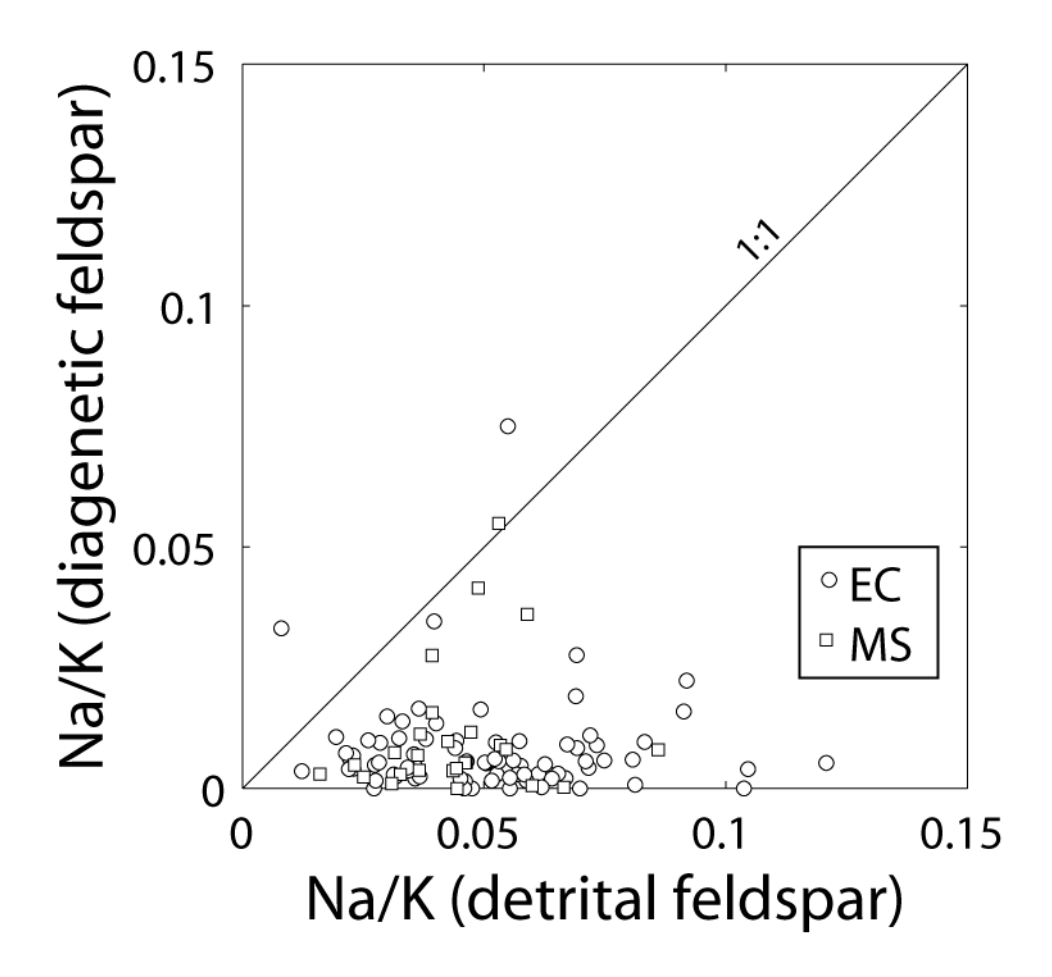
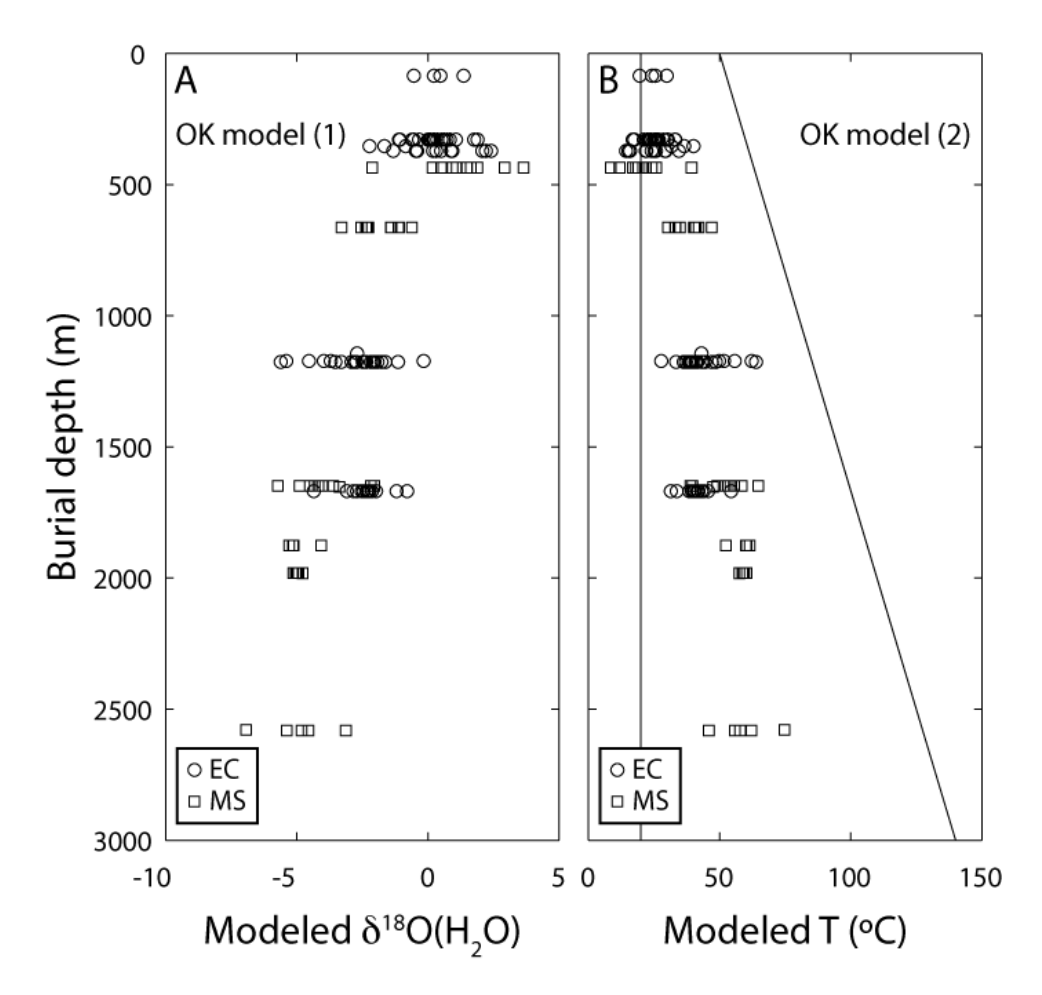


Figure 2.11 (next page). Modeled $\delta^{18}O(H_2O)$ (A) and temperature (B) for OK from the Mt. Simon and Eau Claire formations. Abbreviations: EC = Eau Claire; MS = Mt. Simon. (A) $\delta^{18}O(H_2O)$ values calculated for each $\delta^{18}O(OK)$ analysis as described in model (1) in text using T=45°C, the lowest temperature calculated for OO (Pollington et al., 2011; Hyodo et al., 2013). The wide range of values at each depth and variation with depth in the basin are inconsistent with the early growth and short time frame required by the textural relations observed. (B) temperature calculated for each $\delta^{18}O(OK)$ analysis as described in model (2) in text using $\delta^{18}O(H_2O) = -3\%$. Temperature varies with depth, but remains below a maximum of ~70°C, consistent with early, low temperature growth. Reference lines are shown at 20°C (straight line) and in the same geothermal model described in the text (curved line); these lines are consistent with those plotted in Figure 2.6B. Three samples from the Illinois Basin (depth ~400 m) yield temperatures that are more consistent with those measured from the Wisconsin Arch (Eau Claire sample from 85 m depth and St. Peter samples from Kelly et al., 2007). This may be related to a transitional area between the Illinois Basin and the Wisconsin Arch, where the assumption of 1km exhumation may be an overestimate (Mai and Dott, 1985). The textural relations in these three samples all indicate early precipitation of Kfs relative to other phases. The sample at 663 m, which is from the same drill core as these three samples, is the sample with late Kfs.

Figure 2.11



Tables

Table 2.1. Locations of drill core samples used in this study.

Sample ID	Drill core number*	Current burial depth (m)	Formation [†]	Average δ ¹⁸ O(OK)	N [§] δ ¹⁸ O(OK)	Latitude	Longitude
WI84.7	131467	84.70	EC	21.48	4	43.032947	-89.361297
IL328	12996	328.09	EC	21.36	21	42.437308	-89.857855
IL353	12996	352.65	EC	19.52	3	42.437308	-89.857855
IL371	12996	371.03	EC	21.76	11	42.437308	-89.857855
09IL-6	12996	434.52	MS	22.31	10	42.437308	-89.857855
09IL-29	12996	663.42	MS	19.22	11	42.437308	-89.857855
IL1143	4006	1143.30	EC	18.39	1	40.281809	-88.427412
IL1173	4006	1172.57	EC	17.54	5	40.281809	-88.427412
IL1176	4006	1175.61	EC	18.58	18	40.281809	-88.427412
09IL-31	13639	1648.36	MS	17.15	9	40.127100	-87.559575
09IL-33	13639	1652.63	MS	17.72	1	40.127100	-87.559575
IL1669	ADM	1669.08	EC	18.72	13	39.876500	-88.893700
	CCS#1						
09IL-35	13639	1875.89	MS	16.19	4	40.127100	-87.559575
09IL-39	13639	1980.90	MS	16.07	4	40.127100	-87.559575
09IL-41	13639	1982.11	MS	16.32	1	40.127100	-87.559575
09IL-46	4831	2579.37	MS	14.16	1	38.552155	-89.022456
09IL-50	4831	2581.28	MS	16.44	5	38.552155	-89.022456

^{*}All drill core numbers are Illinois State Geological Survey core ID numbers, except 131467, which is from the Wisconsin Geological and Natural History Survey, and ADM CCS#1, which is from the Midwest Geological Sequestration Consortium. [†]EC=Eau Claire, MS = Mt. Simon. [§]Number of SIMS measurements in Kfs overgrowths per rock.

Appendix A2

Feldspar standards

Five samples of feldspar with a range of compositions were evaluated as potential ion microprobe standards. Grains of each feldspar sample were cast in a one-inch round epoxy mount with UWQ-1 (Fig. A2.1). Four samples are alkali feldspars and include the Fish Canyon Sanidine (FCS, Whitney and Stormer, 1985; Renne et al., 1998), a tephra from the Melilla-Nador basin in Morocco (MES-4, Kuiper et al., 2008), sanidine from the Taylor Creek Rhyolite (TC-2, Renne et al., 1998), and a Kfs sample from the UW-Madison gem collection, originally from the Fianarantsoa province of Madagascar (Gem 28). A purchased plagioclase (ADPPlag) of intermediate composition was also analyzed. Each sample was tested for homogeneity of cations, δ^{18} O and lack of inclusions. Each sample was analyzed for δ^{18} O by laser fluorination (Spicuzza et al., 1998) and secondary ion mass spectrometry (SIMS) and compositionally by electron probe microanalysis (EPMA) (Table A2.1). Our sample of TC-2 was found to be a mixture of plagioclase, Kfs, quartz and oxides and was therefore not evaluated further.

The three alkali feldspars considered for use as new standard materials range from Kfs mol%=69.6% to 94.2%. The plagioclase has an average An mol%=65.1%. These data are summarized in Figure A2.1 and Table A2.2. The δ^{18} O values of each sample were measured by laser fluorination to determine δ^{18} O_{VSMOW} values and by SIMS to determine instrumental biases. This data are summarized in appendix Table A2.2 and data repository Table DR2.2. The Fish Canyon Sanidine is homogenous in δ^{18} O (7.06 \pm 0.17% VSMOW) and will be a useful standard for microanalysis of alkali feldspar. The other two alkali feldspar standards are not as homogenous in δ^{18} O, but cover a different range of chemical composition. Their use as standards

must be evaluated by researchers who should balance the tradeoffs between having a standard that is closer to their samples compositionally, but is not as isotopically homogenous.

Feldspar bias calculation

The instrumental bias on SIMS measurements is dependent on the chemical composition and crystal structure of the phase being analyzed (cf., Eiler et al., 1997; Riciputi et al., 1998; Kita et al., 2009; Valley and Kita, 2009; Page et al., 2010; Kita et al., 2011). It is especially important for minerals that exhibit solid solution (such as feldspars) that the chemical composition of standards used is close to that of the unknowns being analyzed, otherwise an extrapolation or interpolation must be made to account for the bias difference for different chemistries. The three alkali feldspar standards (FCS, MES-4, Gem28) were measured in the same SIMS session to determine the bias as a function of major element chemistry (Figure A2.2). Because we use UWQ-1 as a bracketing standard, all calculations use the difference in the biases of quartz and feldspar to calculate VSMOW values of feldspar. The average of the biases for the three potential standards is statistically indistinguishable from the extrapolation to 100% end member K-feldspar. This shows that in the range of 70-100% K-feldspar, the bias is constant; because of this we use only the Fish Canyon Sanidine (FCS) standard as a normalizing standard and UWQ-1 for a bracketing standard for feldspar unknowns. The difference between the average bias relative to UWQ-1 of the three alkali feldspar standards (5.03‰) and the FCS bias from the same session (4.82‰) is 0.21‰ (Fig. A2.2).

Additional references not cited in main text

- Eiler, J.M., Graham, C., and Valley, J.W., 1997, SIMS analysis of oxygen isotopes: Matrix effects in complex minerals and glasses: Chemical Geology, v. 138, p. 221-244.
- Kita, N.T., Huberty, J.M., Kozdon, R., Beard, B.L., and Valley, J.W., 2011, High-precision SIMS oxygen, sulfur and iron stable isotope analyses of geological materials: accuracy, surface topography and crystal orientation: Surface and Interface Analysis, v. 43, p. 427-431.
- Riciputi, L.R., Paterson, B.A., and Ripperdan, R.L., 1998, Measurement of light stable isotope ratios by SIMS: Matrix effects for oxygen, carbon, and sulfur isotopes in minerals: International Journal of Mass Spectrometry, v. 178, p. 81-112.
- Spicuzza, M.J., Valley, J.W., and McConnell, V.S., 1998, Oxygen isotope analysis of whole rock via laser fluorination; an air-lock approach: Abstracts with Programs Geological Society of America, v. 30, p. 80.
- Whitney, J.A., and Stormer, J.C., 1985, Mineralogy, Petrology, and Magmatic Conditions from the Fish-Canyon Tuff, Central San-Juan Volcanic Field, Colorado: Journal of Petrology, v. 26, p. 726-762.

Appendix Figures

Figure A2.1 (next page). Backscattered electron image of feldspar standard epoxy mount (WI-STD-79). Each sample is labeled with its sample name, average chemical composition, average δ^{18} O by laser fluorination and where the sample was acquired. Inset ternary diagrams show the composition of each sample. Taylor Creek Sanidine was found to be a mixture of different minerals and so was not considered further. Cation and δ^{18} O values of each grain are summarized in data repository Tables DR2.1 and DR2.2.

Figure A2.1

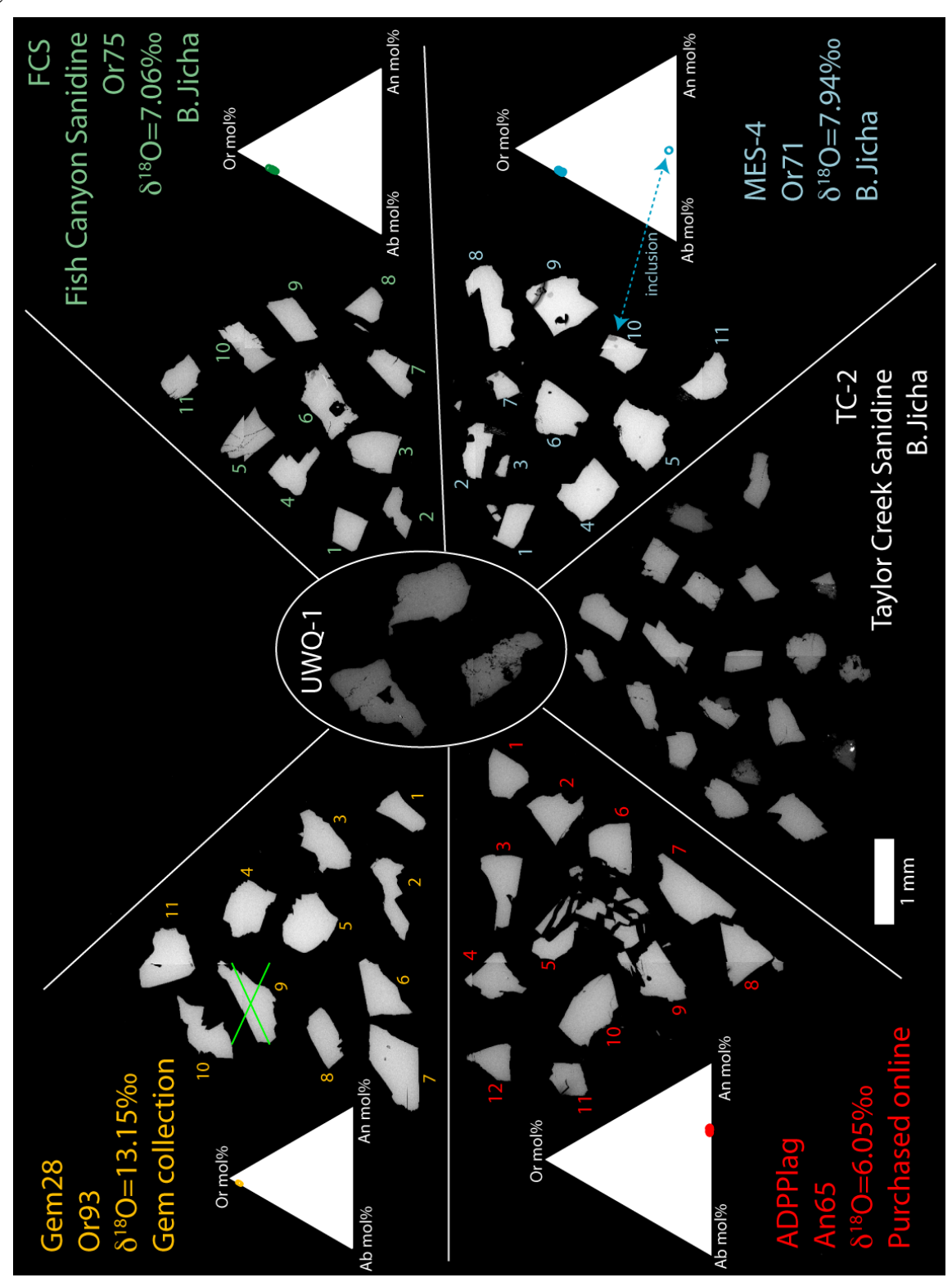


Figure A2.2. Measured SIMS bias relative to UWQ-1 as a function of Kfs percent. Circles represent new standards developed in this study (Gem28, FCS, MES-4).

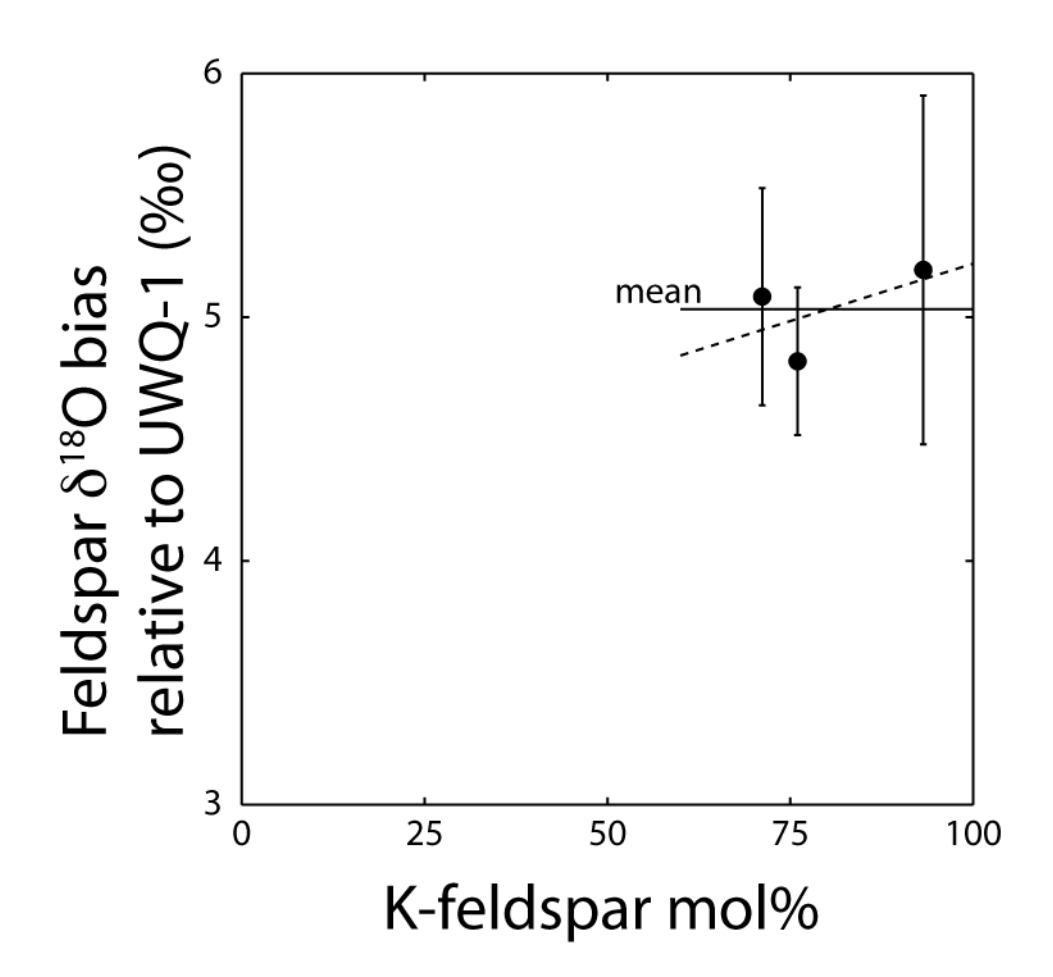


Figure A2.3. Depth vs. Ca content of Kfs from the Mt Simon and Eau Claire formations. Abbreviations: EC = Eau Claire; MS = Mt. Simon. (A) Detrital grains. (B) Overgrowths. Note correlation between [Ca] in overgrowths with the [Ca] in detrital grains from the same depths, particularly at 371 m. This suggests that the components of the overgrowths are locally derived from solution of detrital grains.

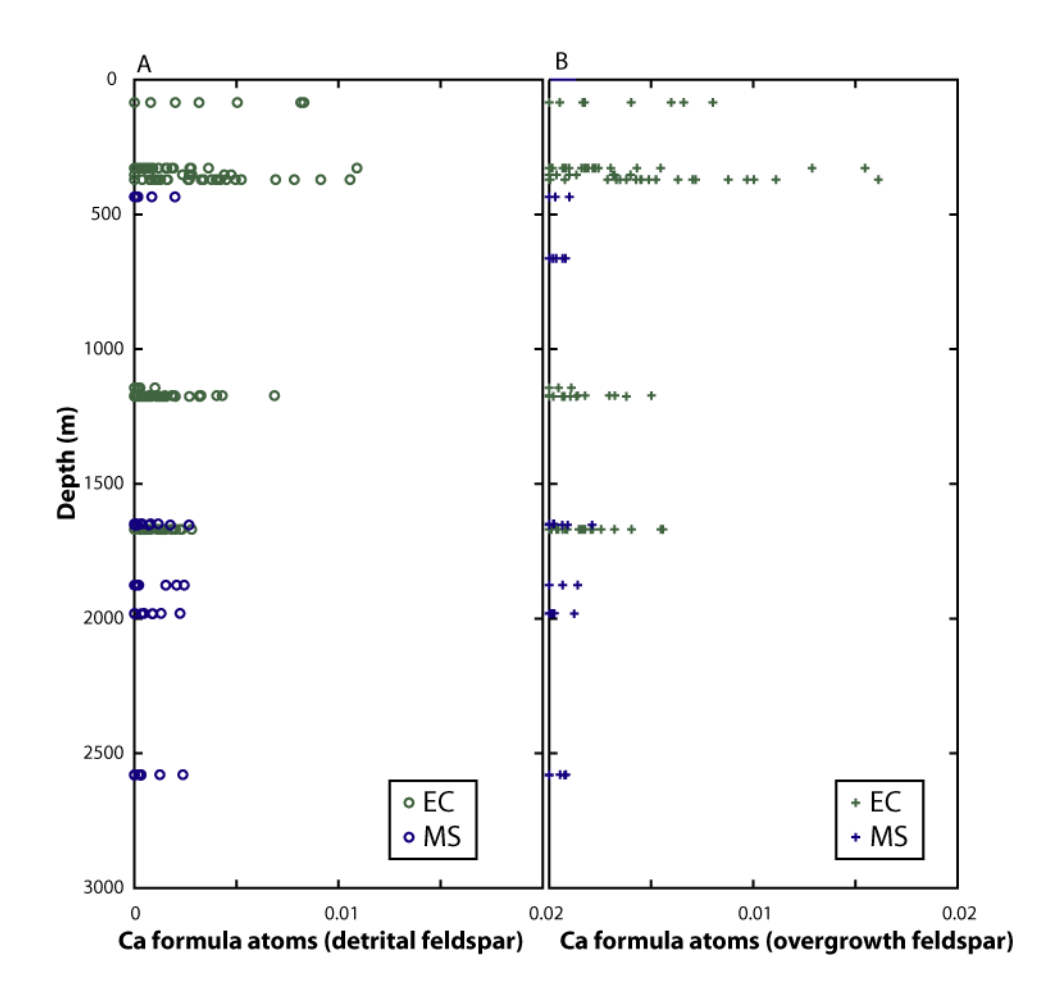
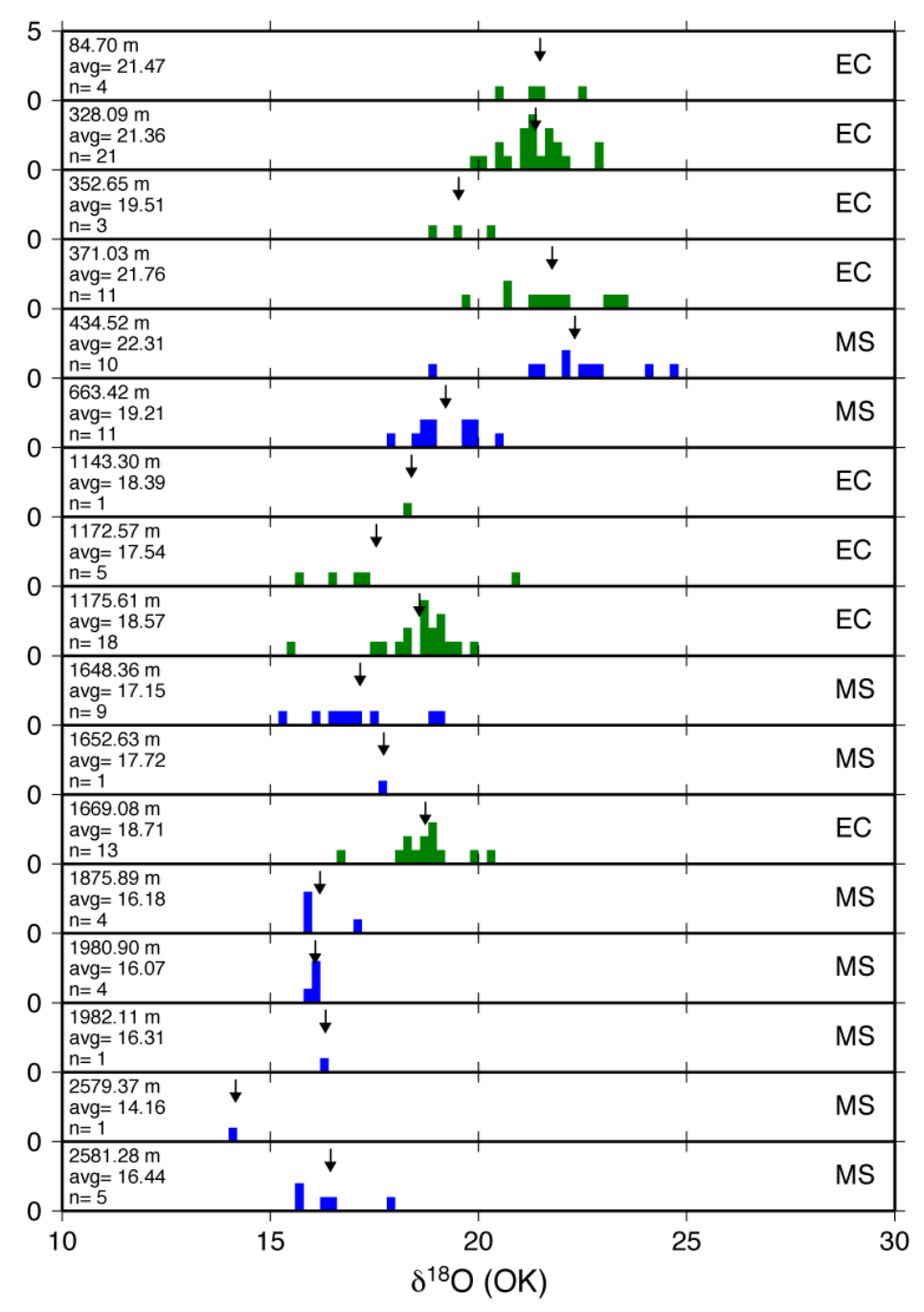


Figure A2.4. Histograms of $\delta^{18}O(OK)$ in each rock studied. Plots are organized by depth. Blue bars are Mt. Simon (MS) samples; green bars are Eau Claire (EC) samples. Arrows indicate average $\delta^{18}O(OK)$ for each rock. Vertical scale in each plot is from 0 to 5. Apparent trend to lower values in deeper samples is dominated by high values in samples from the transitional area between the Illinois Basin and the Wisconsin Arch (328 to 435 m).



Appendix Tables

 Table A2.1. Summary of composition of potential feldspar standards

Sample	Average Kfs mol%	Average Ab mol%	Average An mol%	Average laser $\delta^{18}O$ (% VSMOW)	Laser δ ¹⁸ O 2SD	Average SIMS δ ¹⁸ O raw*	SIMS δ ¹⁸ O raw 2SD
FCS	76	23	1	7.06	0.17	7.14	0.27
MES-4	66	28	6	7.94	0.24	8.35	0.45
Gem28	93	7	0	13.15	0.29	13.84	0.83
ADPPlag	1	34	65	6.05	0.09	9.39	0.13

^{*}Raw SIMS values are from a single session March 10-11, 2011.

Table A2.2. $\delta^{18}\mathrm{O}$ values of feldspar standards measured by laser fluorination

Book #*	Sample name	δ ¹⁸ O (‰ SMOW)	Data not used [†]	Date analyzed	Book #*	Sample name	δ ¹⁸ Ο (‰ SMOW)	Data not used [†]	Date analyzed
L21-10-6	Gem28	13.25	uscu	2/4/11	L21-10-12	ADPPlag	6.08	useu	2/4/11
L21-10-0	Gem28	13.28		2/4/11	L21-10-13	ADPPlag	6.08		2/4/11
L21-10-8	Gem28	15.20	13.58	2/4/11	L21-10-14	ADPPlag	6.11		2/4/11
L21-10-0	Gem28	13.35	13.50	2/4/11	L21-10-15	ADPPlag	5.97		2/4/11
L21-30-9	Gem28	12.96		4/15/11	L21-30-14	ADPPlag	3.57		4/15/11
L21-30-10	Gem28	13.01		4/15/11	L21-30-15	ADPPlag		5.66	4/15/11
L21-30-10	Gem28	13.14		4/15/11	L21-30-16	ADPPlag	6.06	3.00	4/15/11
L21-30-12	Gem28	13.19		4/15/11	L21-30-17	ADPPlag	6.06		4/15/11
L21-30-13	Gem28	12.93		4/15/11	L21-30-18	ADPPlag	6.05		4/15/11
L21-46-9	Gem28	13.32		4/28/11	L21-46-14	ADPPlag	6.09		4/28/11
L21-46-10	Gem28	13.31		4/28/11	L21-46-15	ADPPlag	6.02		4/28/11
L21-46-11	Gem28	13.01		4/28/11	L21-46-16	ADPPlag	6.07		4/28/11
L21-46-12	Gem28	13.10		4/28/11	L21-46-17	ADPPlag	5.96		4/28/11
L21-46-13	Gem28	13.13		4/28/11	L21-46-18	ADPPlag	6.01		4/28/11
Average		13.15			Average		6.05		
2SD		0.29			2SD		0.09		
L21-30-21	MES-4	7.76		4/15/11	L21-30-26	FCS	7.08		4/15/11
L21-30-22	MES-4	8.01		4/15/11	L21-30-27	FCS	7.05		4/15/11
L21-30-23	MES-4	7.86		4/15/11	L21-30-28	FCS	7.13		4/15/11
L21-30-24	MES-4	8.02		4/15/11	L21-30-29	FCS	6.92		4/15/11
L21-30-25	MES-4	8.03		4/15/11	L21-30-30	FCS	7.11		4/15/11
Average		7.94			Average		7.06		
2SD		0.24			2SD		0.17		

^{*}Book # represents lab notebook number, page number, and analysis number on that page

 $^{^{\}dagger}$ During reaction of L21-10-8 a grain of feldspar was ejected from the sample pile. L21-30-14 was heated without adding BrF₅ and no sample gas was analyzed, because of this the sample chamber was not "pre-conditioned" before L21-30-15. These three samples are not used in calculating averages.

Table A2.3. Analytical conditions used for electron probe microanalyses

Element and x-ray line	Crystal used	Standard	Peak counting time (sec)	High and low background counting time (sec)
Al Kα	TAP	Microcline	10	5
Si Kα	TAP	Microcline	10	5
ΚΚα	PET	Microcline	10	5
Να Κα	TAP	Albite	10	5
Са Ка	PET	Plagioclase (An49)	10	5
Βα Lα	LIF	Barite	10*	5*
Fe Ka	LIF	Hematite	10	5

^{*} Data were collected in two sessions; in the second session Ba peak counting time was 20 seconds and background-counting time was 10 seconds on each side of peak

Measurements were made using a 10 nA electron beam and an accelerating voltage of 15 kV with a 10 μm spot size

Data repository (DR2)

Large data tables and figures for individual chapters are included in the supplementary files available with the online version of this dissertation.

Table DR2.1. Major element composition of potential feldspar standards measured by electron microprobe.

Table DR2.2. Oxygen isotope data for standards and clastic samples measured on the WiscSIMS ims-1280 ion microprobe.

Table DR2.3. Major element composition of clastic samples measured by electron microprobe.

Chapter 3

Silicon isotope composition of diagenetic quartz:

A record of Precambrian weathering

Quartz cements modify the porosity and permeability of many rocks including sandstones and mudstones. Although the genesis of these cements is widely studied to determine the origin, flux, pathways and timing of water-rich fluids, cementation is actually controlled by the availability of silicon. The source of silicon during diagenesis is often uncertain. Sources of silicon can be either internal to the rock such as from pressure solution or recrystallization, or external from fluid flow. Stable isotope ratios may provide evidence of fluid/rock interactions. The oxygen isotope fractionation between quartz and water is large and has been used to calculate temperatures of diagenesis and fluid compositions (e.g., Graham et al., 1996; Chen et al., 2001; Kelly et al., 2007; Pollington et al., 2011; Harwood et al., 2013; Hyodo et al., 2013). While aqueous fluid dominates the source of oxygen during precipitation, the source of silicon available for quartz precipitation is an open question. Silicon isotope values of diagenetic quartz reflect the source of dissolved chemical components; if δ^{30} Si values of overgrowth quartz (OQ) are the same as for neighboring detrital quartz (DQ) the cations may be locally sourced from detrital grains. Alternatively, if the δ^{30} Si of OQ is significantly different than that of nearby DQ, then the silicon in those overgrowths is dominated by material derived from outside the formation. In this paper we present high-resolution silicon isotope data for the Mt Simon Sandstone, the basal Cambrian unit in sections of the Midcontinent of North America, with values as low as -5.4% in diagenetic quartz and a range of single overgrowth zonation from -6 to +5%. Terrestrial values of δ^{30} Si this low have only been reported from one other location $(\delta^{30}\text{Si}(OQ)=+0.7 \text{ to } -7.5\%$, Basile-Doelsch et al., 2005) and are interpreted to represent silicon dominated by weathered material. We also present oxygen isotope data of quartz and feldspar from outcrops of the same formation. The low δ^{30} Si values and paired δ^{18} O values may preserve a record of Precambrian weathering.

The Mt Simon Sandstone (Ss) is a mature to supermature feldspathic or subfeldspathic arenite (Hoholick et al., 1984), which unconformably overlies the Precambrian basement across much of the mid-continent of North America from Nebraska to Ohio and from Kentucky to Minnesota. The lower parts of the unit contain alluvial, coastal and tidal deposits and are more feldspathic than the upper part (Templeton, 1951; Buschbach, 1964). The majority of the formation was deposited in a marine setting (Willman et al., 1975). The Mt Simon ranges in thickness in the Illinois Basin from less than 91 m to 792 m (Hoholick et al., 1984). The formation has an overall dip to the southeast, outcropping in Wisconsin and reaching a maximum current burial depth of ~4500 m in southern Illinois. The formation in the Illinois Basin has been interpreted to have been buried up to 1 km deeper than its current depth; whereas sections of the formation currently exposed in Wisconsin were never buried more than ~0.5 km (Mai and Dott, 1985). This has led to interesting differences in the hydrologic and thermal histories of different parts of the Paleozoic sediments in the mid-continent (e.g., Kelly et al., 2007; Pollington et al., 2011). Recent studies have been driven by the exploration of the Mt Simon Ss as a potential reservoir for geologic CO₂ sequestration. A pilot project is currently underway near Decatur, IL, which will inject one million metric tons of CO2 into the formation (Gollakota and McDonald, 2012).

The Mt Simon Ss has been the subject of numerous studies to describe and interpret its depositional and cementation histories (e.g., Driese, 1979; Hoholick et al., 1984; Chen et al., 2001; Bowen et al., 2011; Pollington et al., 2011). The dominant diagenetic cements are quartz and feldspar overgrowths on detrital grains, as well as some interstitial clays and carbonates. At a broad scale, quartz overgrowths are distributed throughout the formation. However, at the centimeter to meter scale, there can be large differences in cement distribution. Some hand

samples have layers with almost complete cementation as well as layers with fully open pore spaces. This may be due to slight variability in permeability and consequently fluid available for cement formation, as well as secondary porosity.

The samples used in this study were collected from drill cores in Illinois and outcrops in Wisconsin (Fig. 3.1). Samples from drill cores are from the north, central, and southern parts of Illinois and cover depth ranges of 394-664 m, 1648-1982 m and 2579-2581 m respectively. Samples from outcrops can be broken up into two broad groups: four samples from two outcrops near Stevens Point, WI (outcrop set A); and nine samples from five outcrops from the sand plains of central Wisconsin (outcrop set B). The outcrops in set A are stratigraphically within a few meters of the contact with the Precambrian-Cambrian unconformity although the contact is not exposed at these outcrops. Two outcrops from set B have an exposure of the contact.

Detrital quartz (DQ) and overgrowth quartz (OQ)were cathodoluminescence (CL) and analyzed for δ^{18} O and δ^{30} Si in situ by secondary ionization mass spectrometry (SIMS) in each sample. Multiple generations of cement are present in samples from outcrop set A and are distinguishable by different CL response (appendix Figure A3.1). There is an early, bright CL domain (Q1) present in many overgrowths from this outcrop set followed by a second dark CL domain that is present in all overgrowths and represents the majority of OQ from these samples. In two overgrowths, there is a final generation (Q3) of bright CL OQ near the overgrowth boundary. The Q2 domain is observed in all overgrowths, but O1 and O3 are present in a much smaller subset of overgrowth quartz.

The DQ from all samples of the Mt Simon sandstone has δ^{30} Si values close to 0% NBS-28 (Fig. 3.2a, average δ^{30} Si = 0.15 ± 0.53% 2SD, n = 105). The δ^{30} Si(OQ) from drill core samples (average δ^{30} Si = 0.01 ± 0.45% 2SD, n = 60) are virtually identical to the detrital values.

The majority of outcrops in Wisconsin (set B) have $\delta^{30} Si(OQ)$ values indistinguishable from detrital quartz (average $\delta^{30} Si = 0.26 \pm 0.73\%$ 2SD, n = 41). Strikingly however, $\delta^{30} Si(OQ)$ from the samples from outcrop set A are considerably lower and more variable (average $\delta^{30} Si = -2.90 \pm 3.14\%$ 2SD, n = 120) than values from any other samples in this study. This distinct difference in diagenetic values is clearly shown in the histograms in Fig. 3.2b-d.

Oxygen isotope values of detrital quartz (DQ; average $\delta^{18}O = 9.7 \pm 4.2\%$ 2SD, n = 72) and K-feldspar (DK; average $\delta^{18}O = 8.7 \pm 2.8\%$ 2SD, n = 10) from outcrops of the Mt Simon Ss are consistent with and similar to those published for DQ and DK from the Illinois Basin (Pollington et al., 2011; Hyodo et al., 2013; Pollington et al., 2013). Overgrowths of quartz (OQ) and K-feldspar (OK) from outcrop set B have $\delta^{18}O$ which are high (OQ average $\delta^{18}O = 30.5 \pm 2.9\%$ 2SD, n = 59; OK average $\delta^{18}O = 22.6 \pm 1.7\%$ 2SD, n = 12) and are similar to $\delta^{18}O(OQ)$ values measured in outcrop samples of the St. Peter Ss (Kelly et al., 2007). The ~8% difference between OQ and OK in these samples is similar to the difference measured for shallowly buried samples in northern Illinois and southern Wisconsin (Pollington et al., 2013). Both the measured values of $\delta^{30}Si(OQ)$ and $\delta^{18}O(OQ)$ from outcrop set A, are strikingly low (Fig. 3.3; average = $21.50 \pm 5.24\%$ 2SD, n = 156). Samples from outcrop set A are not observed to contain K-feldspar. All $\delta^{18}O$ and $\delta^{30}Si$ data are included in data repository tables DR3.1, DR3.2 and DR3.3.

In overgrowths large enough for two analyses (OQ thickness 20-200 μ m), the difference in δ^{30} Si between the earliest spot and the latest spot (Δ^{30} Si(early-late)) provides an indicator of changing δ^{30} Si values over time and with progressive growth. As is to be expected given the rather small total range of δ^{30} Si values, Δ^{30} Si is close to 0% for overgrowths from core samples

(Fig. 3.2e) and samples from outcrop set B (Fig. 3.2g) indicating no systematic variation during progressive precipitation. Samples from outcrop set A, which have a wider range of $\delta^{30} \text{Si}(\text{OQ})$ also are much more variable in $\Delta^{30} \text{Si}$ (Fig. 3.2f). High positive values of $\Delta^{30} \text{Si}$ correlate with high values of $\Delta^{18} \text{O}$ from the same overgrowths (Fig. 3.4). Values of $\Delta^{18} \text{O}$ and $\Delta^{30} \text{Si}$ are controlled by the early Q1 cement, which has $\delta^{30} \text{Si} \sim 0$ % and $\delta^{18} \text{O} \sim 28$ % compared to Q2, which has low $\delta^{30} \text{Si}$ and $\delta^{18} \text{O}$. The few highly negative $\Delta^{30} \text{Si}$ values are controlled by the difference between Q2 and Q3, which has $\delta^{30} \text{Si} \sim 0$ % and $\delta^{18} \text{O}$ higher than the average for these rocks.

During weathering of feldspars, 28 Si is preferentially fractionated into the precipitated clay minerals leaving the solid fraction lower in δ^{30} Si and the aqueous fluid higher in δ^{30} Si (Ding et al., 1996; Ding et al., 2004; Ziegler et al., 2005a; Ziegler et al., 2005b). Ziegler et al. (2005a) reported results from precipitation experiments that show Si in solution is enriched in 30 Si by as much as \sim 1 to 4‰ compared to Si in precipitated minerals. Silicon isotopes are not expected to fractionate during quartz dissolution because quartz dissolves congruently. Little work has been done to quantify silicon isotope fractionation during quartz precipitation, although it has been suggested that negative values in diagenetic quartz are evidence of reprecipitation of Si fractionated during weathering (Basile-Doelsch et al., 2005).

Aqueous silicon (Si_{aq}) to precipitate quartz overgrowths can come from two sources: (I) Si derived from dissolution of detrital quartz and has a $\delta^{30}Si$ value $\sim 0\%$ and (II) Si derived from chemically weathered minerals that has been fractionated and has a $\delta^{30}Si$ value significantly different from 0%. The overgrowths in the majority of Mt Simon Ss samples (all basin samples, and outcrop set B) are consistent with source (I), having $\delta^{30}Si$ values $\sim 0\%$. This suggests that these overgrowths precipitated from Si_{aq} dominated by igneous quartz. The diagenetic quartz in

the samples from outcrop set A however appear to be dominated by Si_{aq} derived from weathering of other silicate minerals. The overgrowths in the Mt Simon Ss with $\delta^{30}Si \sim 0\%$ could contain Si that is locally derived from the sandstone, or transported from another source with primary igneous Si. Regardless of the source of Si in these samples, it is clear that it is distinctly different in $\delta^{30}Si$ than the source of Si in outcrop set A.

The $\delta^{18}O(OQ)$ values from Illinois Basin samples are interpreted to reflect growth during burial and heating of the basin (Pollington et al., 2011; Hyodo et al., 2013). The $\delta^{18}O(OQ)$ from outcrop set B are high and are consistent with growth at near-surface temperatures, similar to what has been observed for outcrops of the St. Peter Ss in southern Wisconsin (Kelly et al., 2007). However, $\delta^{18}O(OQ)$ from outcrop set A are ~9% lower than from outcrop set B (Fig. 3.3), likely due to precipitation from warmer fluids. The variability in $\Delta^{18}O$ and $\Delta^{30}Si$ in outcrop set A (Fig. 3.4) reflects changes in the conditions of precipitation between the three generations of cement. The early cement represents growth at conditions similar to overgrowths from outcrop set B whereas the majority of cement, which formed during Q2, reflects growth from warmer fluid. Finally, Q3 reflects a return to low temperature precipitation.

The sandstones at outcrop set A are within a few meters of the Precambrian-Cambrian unconformity, which acted as a conduit along which hydrothermal fluids have flowed in the past (Harper et al., 1995; Ziegler and Longstaffe, 2000). Where paleo-saprolites have been observed in the North American midcontinent, chemical and mineralogical indicators demonstrate weathering profiles (Driese et al., 2007; Driese and Medaris, 2008). Before deposition of the Mt Simon Ss in the area, the Precambrian rocks were exposed to chemical weathering and erosion, possibly creating horizons with residual clays low in δ^{30} Si. Parts of the saprolite closer to the surface would have undergone a higher degree of weathering and may have gone through

multiple cycles of Si-isotope fractionation. Later, after deposition of the sandstone and after a period of low temperature cementation, hydrothermal fluids flowing along the contact (Harper et al., 1995; Ziegler and Longstaffe, 2000) dissolved the low δ^{30} Si paleosols on basement rock leading to Si_{aq} with low δ^{30} Si values. The Si and O were then precipitated as overgrowths in the sandstone with low δ^{30} Si derived from weathered material and low δ^{18} O controlled by the relatively warm fluid (T \approx 100°C assuming δ^{18} O(H₂O) = -3‰). The majority of negative Δ^{30} Si values, which cluster around Δ^{18} O \approx 0% (Fig. 3.4), are controlled by progressive leaching of variably weathered basement rocks, or mixing with other sources of dissolved silica.

The detrital quartz from the Mt Simon sandstone δ^{30} Si values are close to 0‰, which is consistent with a source dominated by igneous quartz (Douthitt, 1982; Ding et al., 1996; Ziegler et al., 2005a; Ziegler et al., 2005b). The lack of variability in δ^{30} Si(OQ) in the majority of the Mt. Simon Ss indicates that the source of silicon for overgrowths in most samples studied is dominated by silicon that has not been significantly fractionated. The silicon for overgrowth formation may be locally derived from pressure solution of detrital grains, but the introduction of fluids dominated by unfractionated silicon cannot be ruled out on the basis of δ^{30} Si(OQ) alone. However, there is also evidence that in very localized settings hydrothermal fluids have leached fractionated silicon from a chemically weathered rock unit, which was then precipitated as quartz overgrowths. The δ^{30} Si(OQ) values of these overgrowths therefore illuminate a record of Precambrian weathering, which may not otherwise be available to study due to poor exposure. The extremely low δ^{30} Si values (<-5‰) suggest that the integrated history of weathering responsible was particularly intense.

ACKNOWLEDGEMENTS

The WiscSIMS laboratory is supervised by N. Kita and maintained by J. Kern. B. Hess prepared sample mounts. Samples from Illinois were provided by the Illinois State Geological Survey. Wisconsin sample 07WI-1 was provided by R. Dott, Jr. Preliminary analyses of similar samples were performed by A. Trzaskus and P. Heck. Funding was provided by DOE (93ER14389) and the UW-Madison Dept. of Geoscience. The WiscSIMS laboratory is partially funded by NSF (EAR-1053466).

REFERENCES CITED

- Basile-Doelsch, I., Meunier, J.D., and Parron, C., 2005, Another continental pool in the terrestrial silicon cycle: Nature, v. 433, p. 399-402.
- Bowen, B.B., Ochoa, R.I., Wilkens, N.D., Brophy, J., Lovell, T.R., Fischietto, N., Medina, C.R., and Rupp, J.A., 2011, Depositional and diagenetic variability within the Cambrian Mount Simon Sandstone; implications for carbon dioxide sequestration: Environmental Geosciences, v. 18, p. 69-89.
- Buschbach, T.C., 1964, Cambrian and Ordovician strata of northeastern Illinois: Illinois State Geological Survey Report of Investigations, 90 p.
- Chen, Z.S., Riciputi, L.R., Mora, C.I., and Fishman, N.S., 2001, Regional fluid migration in the Illinois Basin: Evidence from *in situ* oxygen isotope analysis of authigenic K-feldspar and quartz from the Mount Simon Sandstone: Geology, v. 29, p. 1067-1070.
- Ding, T., Jiang, S., Wan, D., Li, Y., Li, J., Song, H., Liu, Z., and Yao, X., 1996, Silicon Isotope Geochemistry, Beijing, Geological Publishing House, 125 p.
- Ding, T., Wan, D., Wang, C., and Zhang, F., 2004, Silicon isotope compositions of dissolved silicon and suspended matter in the Yangtze River, China: Geochimica et Cosmochimica Acta, v. 68, p. 205-216.
- Douthitt, C.B., 1982, The Geochemistry of the Stable Isotopes of Silicon: Geochimica et Cosmochimica Acta, v. 46, p. 1449-1458.
- Driese, S.G., 1979, Paleoenvironments of the Upper Cambrian Mt. Simon formation in western and west-central Wisconsin [M. S. thesis]: Madison, University of Wisconsin-Madison.
- Driese, S.G., Medaris, L.G., Ren, M.H., Runkel, A.C., and Langford, R.P., 2007, Differentiating pedogenesis from diagenesis in early terrestrial paleoweathering surfaces formed on granitic composition parent materials: Journal of Geology, v. 115, p. 387-406.
- Driese, S.G., and Medaris, L.G., 2008, Evidence for biological and hydrological controls on the development of a Paleoproterozoic paleoweathering profile in the Baraboo Range, Wisconsin, USA: Journal of Sedimentary Research, v. 78, p. 443-457.
- Gollakota, S., and McDonald, S., 2012, CO₂ capture from ethanol production and storage into the Mt Simon Sandstone: Greenhouse Gases-Science and Technology, v. 2, p. 346-351.
- Graham, C.M., Valley, J.W., and Winter, B.L., 1996, Ion microprobe analysis of ¹⁸O/¹⁶O in authigenic and detrital quartz in the St Peter Sandstone, Michigan Basin and Wisconsin Arch, USA: Contrasting diagenetic histories: Geochimica et Cosmochimica Acta, v. 60, p. 5101-5116.
- Harper, D.A., Longstaffe, F.J., Wadleigh, M.A., and Mcnutt, R.H., 1995, Secondary K-Feldspar at the Precambrian-Paleozoic Unconformity, Southwestern Ontario: Canadian Journal of Earth Sciences, v. 32, p. 1432-1450.
- Harwood, J., Aplin, A.C., Fialips, C.I.M., Iliffe, J.E., Kozdon, R., Ushikubo, T., and Valley, J.W., 2013, Quartz cementation history of sandstones revealed by high resolution SIMS oxygen isotope analysis: Journal of Sedimentary Research, v. 83, p. 522-530.

- Heck, P.R., Huberty, J.M., Kita, N.T., Ushikubo, T., Kozdon, R., and Valley, J.W., 2011, SIMS analyses of silicon and oxygen isotope ratios for quartz from Archean and Paleoproterozoic banded iron formations: Geochimica et Cosmochimica Acta, v. 75, p. 5879-5891.
- Hoholick, J.D., Metarko, T., and Potter, P.E., 1984, Regional Variations of Porosity and Cement St-Peter and Mount Simon Sandstones in Illinois Basin: American Association of Petroleum Geologists Bulletin, v. 68, p. 753-764.
- Hyodo, A., Kozdon, R., Pollington, A.D., and Valley, J.W., 2013, Evolution of quartz cementation and burial history of the Eau Claire Formation based on *in situ* oxygen isotope analysis of quartz overgrowths: Journal of Sedimentary Research, p. in review.
- Kelly, J.L., Fu, B., Kita, N.T., and Valley, J.W., 2007, Optically continuous silcrete quartz cements of the St. Peter Sandstone: High precision oxygen isotope analysis by ion microprobe: Geochimica et Cosmochimica Acta, v. 71, p. 3812-3832.
- Kita, N.T., Ushikubo, T., Fu, B., and Valley, J.W., 2009, High precision SIMS oxygen isotope analysis and the effect of sample topography: Chemical Geology, v. 264, p. 43-57.
- Mai, H., and Dott, J., R. H., 1985, A subsurface study of the St. Peter Sandstone in southern and eastern Wisconsin: Wisconsin Geological and Natural History Survey Information Circular, 26 p.
- Pollington, A.D., Kozdon, R., and Valley, J.W., 2011, Evolution of quartz cementation during burial of the Cambrian Mount Simon Sandstone, Illinois Basin: *In situ* microanalysis of δ^{18} O: Geology, v. 39, p. 1119-1122.
- Pollington, A.D., Hyodo, A.M., Kozdon, R., and Valley, J.W., 2013, A previously unrecognized episode of low temperature feldspar diagenesis in Cambrian Mount Simon and Eau Claire formations revealed by *in situ* microanalysis of δ^{18} O, Pollington Ph.D. dissertation.
- Templeton, J.S., Jr., 1951, The Mt. Simon Sandstone in Northern Illinois: Illinois Geological Survey Circular, v. 170, p. 151-159.
- Valley, J.W. and Kita, N.T., 2009, *In situ* oxygen isotope geochemistry by ion microprobe, *in* Fayek, M., ed., Secondary Ion Mass Spectrometry in the Earth Sciences: Gleaning the big picture from a small spot: Short Course Series 41, Mineralogical Association of Canada, p. 19-63.
- Willman, H.B., Atherton, E., Buschbach, T.C., Collinson, C., Frye, J.C., Hopkins, M.E., Lineback, J.A., and Simon, J.A., 1975, Handbook of Illinois stratigraphy: Illinois State Geological Survey Bulletin, 261 p.
- Ziegler, K. and Longstaffe, F.J., 2000, Clay mineral authigenesis along a mid-continental scale fluid conduit in Palaeozoic sedimentary rocks from southern Ontario, Canada: Clay Minerals, v. 35, p. 239-260.
- Ziegler, K., Chadwick, O.A., Brzezinski, M.A., and Kelly, E.F., 2005a, Natural variations of δ^{30} Si ratios during progressive basalt weathering, Hawaiian Islands: Geochimica et Cosmochimica Acta, v. 69, p. 4597-4610.

Ziegler, K., Chadwick, O.A., White, A.F., and Brzezinski, M.A., 2005b, δ^{30} Si systematics in a granitic saprolite, Puerto Rico: Geology, v. 33, p. 817-820.

Figures

Figure 3.1. Map showing location of samples from this and previous studies and surrounding area. Open circles represent locations of Mt Simon Ss drill cores, square represents outcrop set A (see text), triangles represent outcrop set B, diamonds represent samples from the Ordovician St. Peter Ss (Kelly et al., 2007), crosses represent drill core samples of the Eau Claire Formation (Hyodo et al., 2013). Sample locations for this study are listed in appendix Table A3.1.

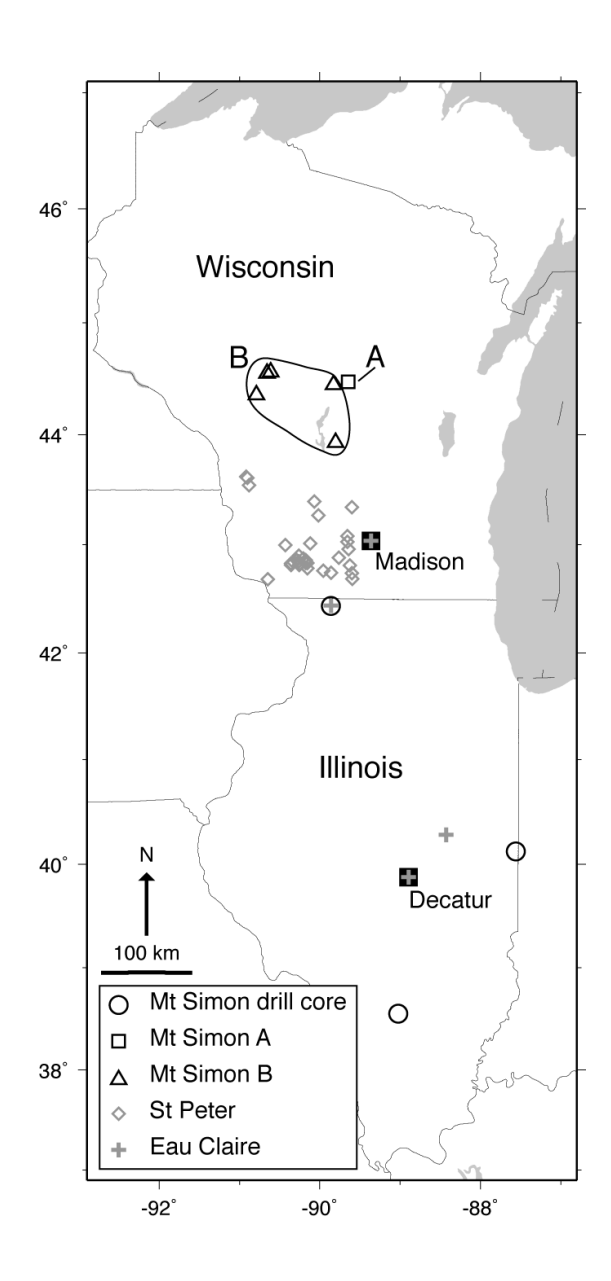


Figure 3.2. Histograms of $\delta^{30} Si(Qz)$ (a-d) and $\Delta^{30} Si(early OQ - late OQ)$ (e-g) for the Mt Simon Sandstone of Wisconsin and Illinois. Gray arrows represent the average value of each panel. a) $\delta^{30} Si(DQ)$ from all samples studied. b) $\delta^{30} Si(OQ)$ from Illinois Basin drill core samples. c) $\delta^{30} Si(OQ)$ from outcrop set A samples. d) $\delta^{30} Si(OQ)$ from outcrop set B samples. e) $\Delta^{30} Si(early-late)$ from Illinois Basin drill core samples. f) $\Delta^{30} Si(early-late)$ from outcrop set B samples. Note colors of bars from overgrowth data corresponds between b-d and e-g.

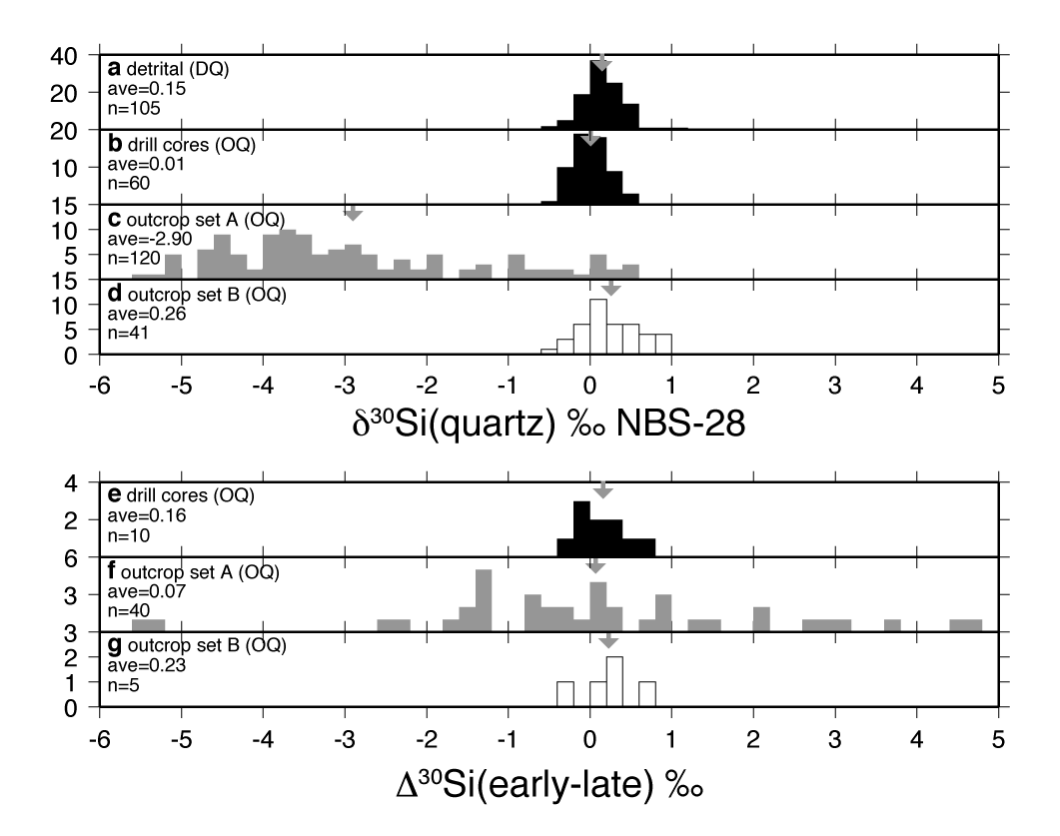


Figure 3.3. Crossplot of δ^{18} O and δ^{30} Si for quartz from the Mt Simon Sandstone. Symbols are the same as Figure 3.1: circles represent drill cores from the Illinois Basin, squares represent outcrop set A, triangles represent outcrop set B. Open symbols represent overgrowth quartz, filled symbols represent detrital quartz. Cross represents typical 2SD of 0.3‰ for both δ^{18} O and δ^{30} Si. Values of detrital grains from all datasets cluster around igneous values (δ^{18} O≈10‰, δ^{30} Si≈0‰) and are dominantly within the dashed oval. δ^{18} O values of basin samples represent growth over a range of temperatures (Pollington et al., 2011), δ^{18} O of outcrop set B samples indicate growth at low temperature similar to that measured by Kelly et al. (Kelly et al., 2007). Low values of δ^{30} Si and δ^{18} O of outcrop set A interpreted to represent growth from weathered material introduced to the rock under hydrothermal conditions. See also appendix figure A3.2.

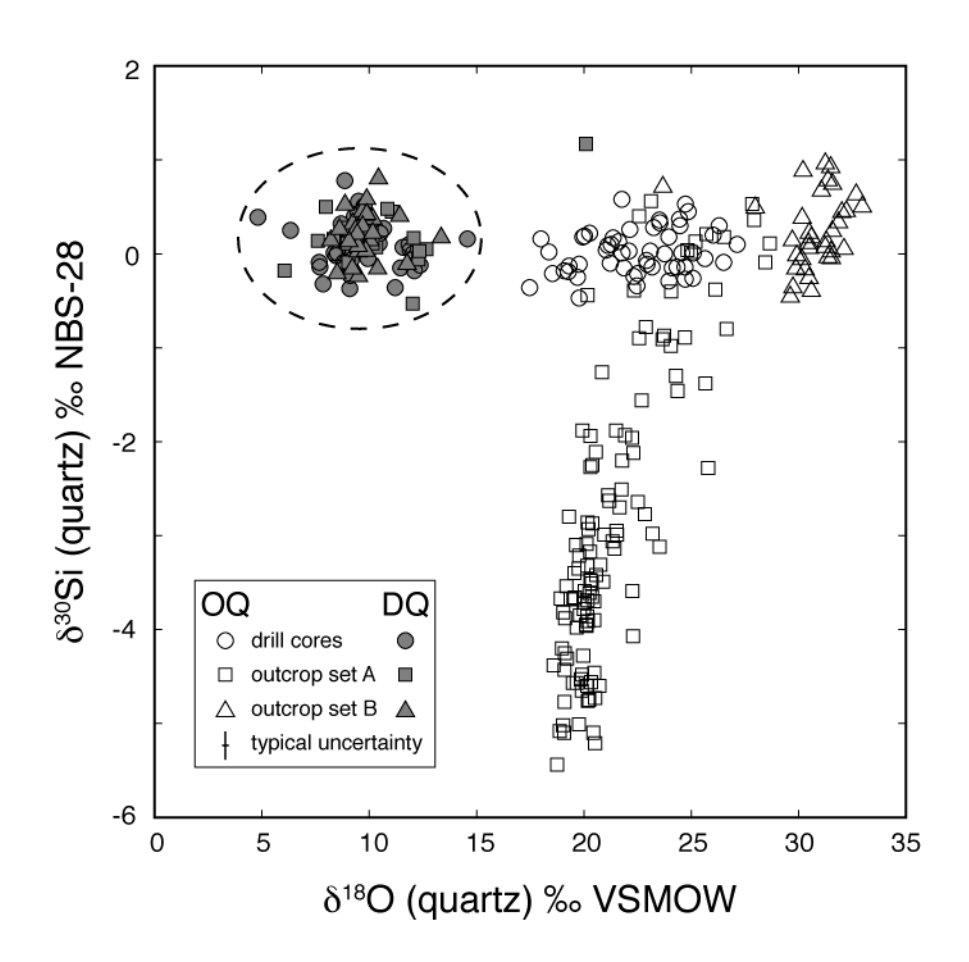
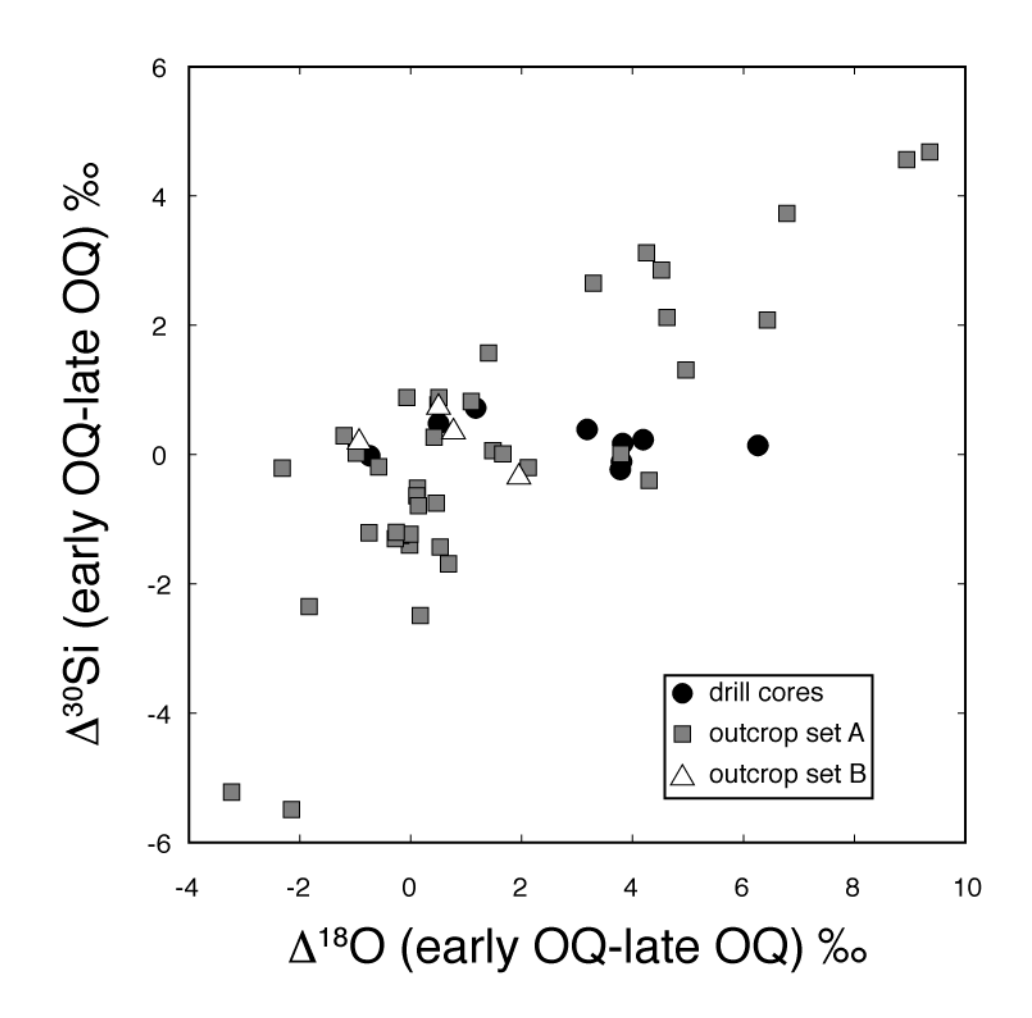


Figure 3.4. Crossplot of Δ^{18} O(early OQ-late OQ) vs. Δ^{30} Si(early OQ-late OQ). Symbols are the same as figures 3.1 and 3.2: circles represent drill cores from the Illinois Basin, squares represent outcrop set A, triangles represent outcrop set B. Positive trend of Δ^{18} O vs. Δ^{30} Si in outcrop set A is dominated by an early high δ^{18} O, high δ^{30} Si generation of cement. Flat trend in data from drill cores and outcrop set B reflect variability in δ^{18} O(OQ) due to temperature (IL Basin, Pollington et al., 2011) and a lack of variability in δ^{30} Si(OQ) values. See also appendix Figure A3.3.



Appendix A3

METHODS

Chips from rocks were either cast into one-inch epoxy mounts, or prepared as standard petrographic thin sections. Samples were imaged by secondary electron (SE), backscattered electron (BSE) and cathodoluminescence (CL) modes using a Hitachi 3400 SEM. Detailed descriptions of imaging techniques and criteria for selecting analysis locations are described in previous publications (e.g., Kelly et al., 2007; Pollington et al., 2011; Hyodo et al., 2013; Pollington et al., 2013). After imaging, samples were analyzed on a CAMECA ims-1280 secondary ion mass spectrometer (SIMS) using a 10 kV primary beam of ¹³³Cs⁺ ions. Analysis conditions of silicon isotopes have been previously published (Heck et al., 2011) and are similar to conditions for oxygen isotopes (Kelly et al., 2007; Kita et al., 2009; Valley and Kita, 2009). Silicon isotope values are reported as deviations in parts per thousand from the standard NBS-28 using delta notation:

$$\delta^{30} Si = \left[\left(\frac{R_{Sam ple}}{R_{NBS-28}} \right) - 1 \right] \times 1000$$
 (1)

where $R = {}^{30}\text{Si}/{}^{28}\text{Si}$. External precision of $\delta^{30}\text{Si}$ was evaluated by 4 consecutive measurements of quartz standard ($\delta^{30}\text{Si}(\text{UWQ-1}) = -0.03\%$ NBS-28, Heck et al., 2011) before and after each set of 4-17 measurements of unknown quartz. Precision on $\delta^{30}\text{Si}$ throughout the analytical period varied from 0.14‰ to 0.56‰ 2SD, precision on $\delta^{18}\text{O}$ varied from 0.13‰ to 0.61‰ 2SD. Samples were imaged after isotope analysis to determine whether pits were successfully aimed in either detrital grains or overgrowths. If analysis spots overlap the detrital/overgrowth boundary or contain irregularities (holes, inclusions, etc.) they are not considered in the discussion.

Appendix Figures

Figure A3.1 (next page). Photomicrographs of sample 09WI-17, outcrop set A. a) Backscattered electron (BSE) image. All grains and overgrowths in this image are quartz (Qz). b) Cathodoluminescence (CL) image of the same area as panel a. Detrital quartz (DQ) and overgrowth quartz (OQ), which appear the same by BSE, are distinguishable by CL. The distinct early, bright CL texture (Q1) followed by a later dark CL domain (Q2) in the same overgrowth is clearly visible in this image. This overgrowth has $\delta^{18}O(Q1) = 28.67\%$ & $\delta^{30}Si(Q1) = 0.11\%$ and distinctly different $\delta^{18}O(Q2) = 22.24\%$ & $\delta^{30}Si(Q2) = -1.96\%$. Scale bar in each panel is 200 μm.

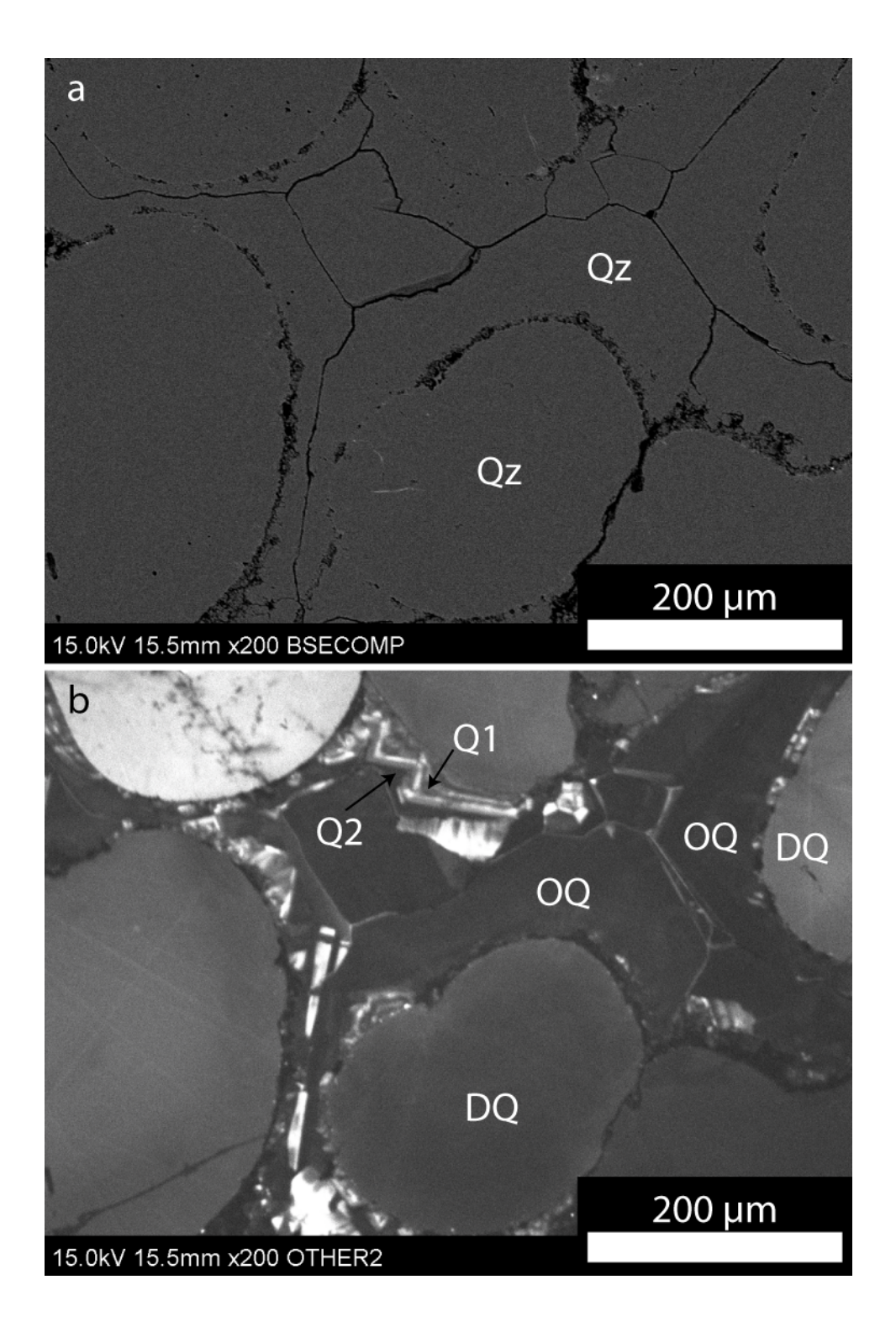


Figure A3.2. Crossplot of $\delta^{18}O$ and $\delta^{30}Si$ for quartz of individual samples from the Mt Simon Sandstone. Symbols are the same as Figure 3.1: circles represent drill cores from the Illinois Basin, squares represent outcrop set A, triangles represent outcrop set B. Open symbols represent overgrowth quartz, filled symbols represent detrital quartz. Sample 09WI-18, which is ~ 0.4 m stratigraphically higher than 09WI-17 in the same outcrop, has distinctly higher $\delta^{30}Si(OQ)$ and $\delta^{18}O(OQ)$ values than 09WI-17. The highest values from 09WI-17 and 09WI-18 are from early bright CL domains (Fig. A3.1).

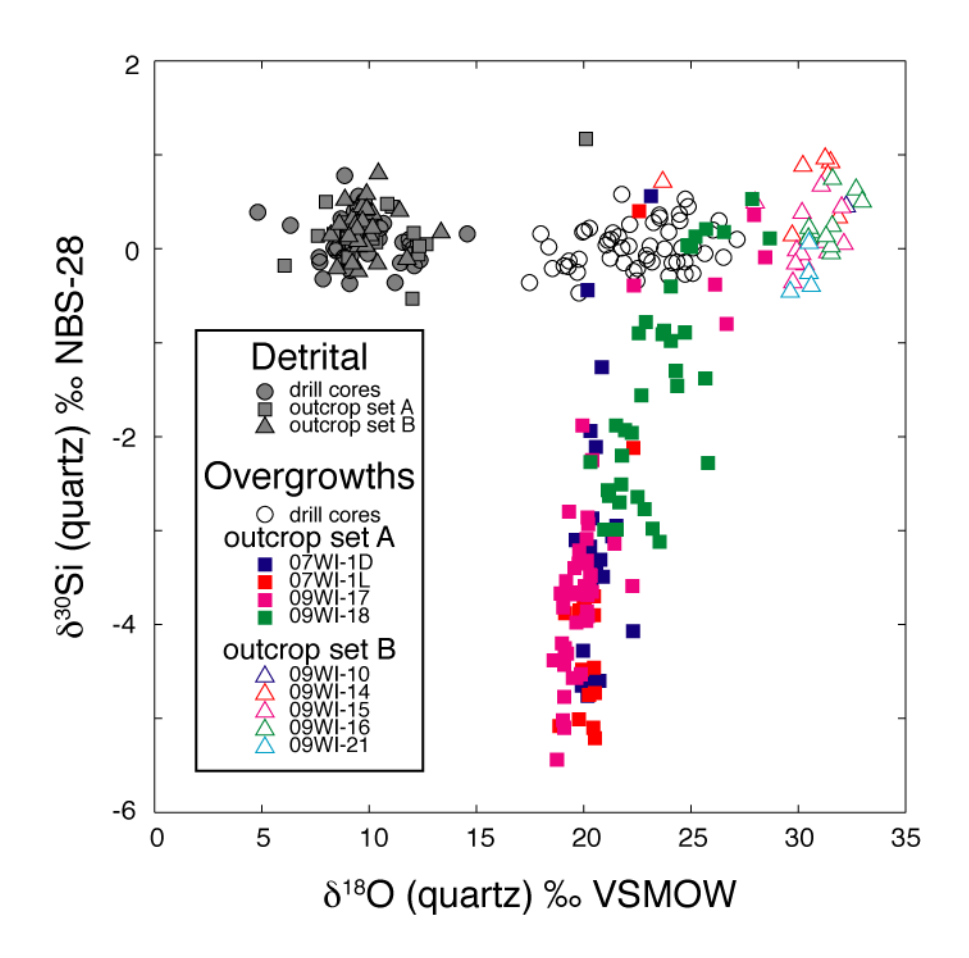
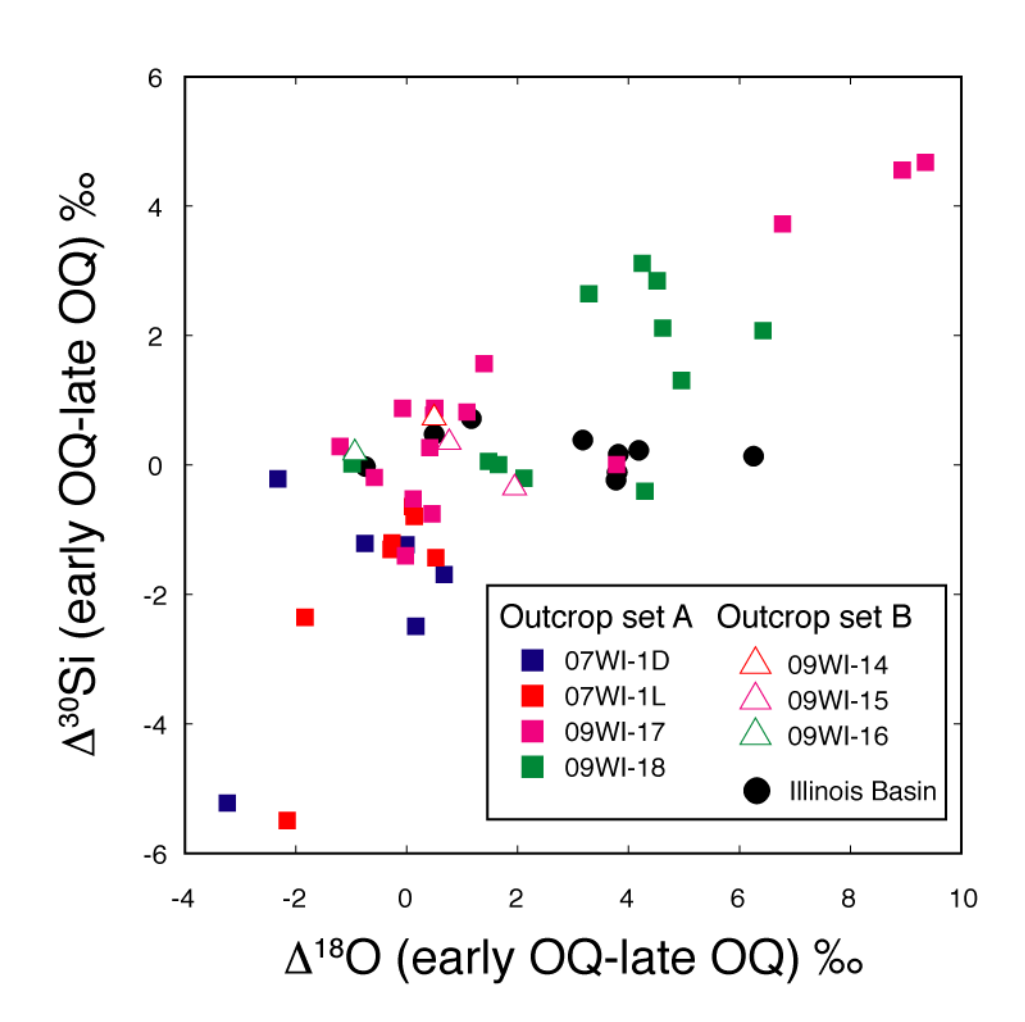


Figure A3.3. Crossplot of Δ^{18} O(early OQ-late OQ) vs. Δ^{30} Si(early OQ-late OQ) for individual samples. Symbols are the same as Figures 3.1 and 3.2: circles represent drill cores from the Illinois Basin, squares represent outcrop set A, triangles represent outcrop set B; colors are the same as Figure A3.2. Positive trend of Δ^{18} O vs. Δ^{30} Si in outcrop set A is dominated by an early high δ^{18} O, high δ^{30} Si generation of cement (Q1), particularly in samples 09WI-17 and 09WI-18. The two highly negative Δ^{30} Si values from 07WI-1D and 07WI-1L are controlled by a final generation of cement (Q3) with δ^{30} Si \sim 0%; the individual data points for these two spots are the highest of the respective rocks in Figure A3.2.



Appendix Table

Table A3.1. Locations of samples used in this study.

Sample ID	Drill core number*	Outcrop set or current burial depth (m)	Latitude N	Longitude W
Drill cores				
09IL-1	12996	434.52	42.437308	-89.857855
09IL-6	12996	434.52	42.437308	-89.857855
09IL-29	12996	663.42	42.437308	-89.857855
09IL-31	13639	1648.36	40.127100	-87.559575
09IL-33	13639	1652.63	40.127100	-87.559575
09IL-35	13639	1875.89	40.127100	-87.559575
09IL-39	13639	1980.90	40.127100	-87.559575
09IL-41	13639	1982.11	40.127100	-87.559575
09IL-46	4831	2579.37	38.552155	-89.022456
09IL-50	4831	2581.28	38.552155	-89.022456
Outcrops				
07WI-1 [†]	_	A	-	-
09WI-2	-	В	44.358066	-90.792633
09WI-10	-	В	44.551566	-90.657933
09WI-13	-	В	44.559866	-90.612683
09WI-14	-	В	44.449433	-89.827383
09WI-15	-	В	44.449433	-89.827383
09WI-16	-	В	44.449433	-89.827383
09WI-17	-	A	44.473283	-89.64765
09WI-18	-	A	44.473283	-89.64765
09WI-21	-	В	43.93015	-89.80395

^{*}All drill core numbers are Illinois State Geological Survey core ID numbers

[†]Sample 07WI-1 was donated by Prof. R. Dott, Jr., UW-Madison. The hand sample was cut into two pieces, 07WI-1L and 07WI-1D based on the dominant banding (light and dark). The exact sampling location of the sample is unknown, but it is likely from between the outcrop with samples 09WI-14,-15,-16 and that with 09WI-17,-18.

Data repository (DR3)

Large data tables and figures for individual chapters are included in the supplementary files available with the online version of this dissertation.

Table DR3.1. Oxygen isotope composition of detrital and diagenetic quartz from outcrop samples measured on the WiscSIMS ims-1280 ion microprobe.

Table DR3.2. Silicon isotope composition of detrital and diagenetic quartz measured on the WiscSIMS ims-1280 ion microprobe.

Table DR3.3. Paired oxygen and silicon isotope measurements of detrital and diagenetic quartz measured on the WiscSIMS ims-1280 ion microprobe. Each line represents one δ^{18} O and one adjacent δ^{30} Si analysis.

Chapter 4

Experimental calibration of silicon and oxygen isotope fractionation between quartz and water at 250°C: A new method using *in situ* microanalysis of experimental products

Planned for submission with the following authors: Anthony D. Pollington, Reinhard Kozdon, Lawrence M. Anovitz, R. Bastian Georg, Michael J. Spicuzza, John W. Valley

Abstract

Quartz is the most common mineral in the earth's crust. The oxygen isotope ratio of quartz provides important information restricting fluid and thermal conditions under which it precipitated. Recent analytical advancements have led to an increased interest in the silicon isotopes of many minerals, including quartz. Whereas oxygen isotopes may yield information about the fluid history of the mineral, silicon isotopes can contain information about sources of dissolved ions and fluids. However, interpretation of isotope data has been hampered by a lack of experimentally determined fractionation factors for silicon isotope fractionation between quartz and fluid. In addition to a lack of silicon isotope fractionation factors, there is a large spread in published oxygen isotope fractionation factors, largely due to experimental calibrations performed at high temperatures. In this study we present the first measurements of silicon isotope fractionation from experimentally precipitated quartz and a new measurement of oxygen isotope fractionation using a novel in situ analysis technique using secondary ion mass spectrometry to directly measure experimental products. Quartz overgrowths 235 µm thick were precipitated in a silica-H₂O-NaOH-NaCl solution, with a pH ~12, at a temperature of 250°C in 126 days. At 250°C, Δ^{30} Si(Qtz-fluid)=0.55 ± 0.10% and Δ^{18} O(Qtz-H₂O)=10.63 ± 0.07%.

1. Introduction

Since Urey (1947) first proposed the use of isotope fractionation as a method for determining temperatures, there have been hundreds of calibrations published for the light stable isotope fractionation of different elements between different phases (Chacko et al., 2001). Fractionation factors vary with element and the phases involved, so knowledge of the correct calibration for the system being studied is of great importance. Fractionation factors for a given isotope system and pair of phases can be determined experimentally, empirically, or derived theoretically.

There are relatively few published estimates for the fractionation of silicon isotopes between silica minerals and fluids (Douthitt, 1982; Li et al., 1995; De La Rocha et al., 1997; Ziegler et al., 2000; De La Rocha, 2003; Georg et al., 2007; Geilert et al., 2012), and there are no experimental determinations of the silicon isotope fractionation factors between quartz and aqueous silicon. Most estimates are based on measurements of natural samples (Douthitt, 1982; De La Rocha, 2003; Georg et al., 2007). The experimental calibrations are mostly for cultured diatoms (De La Rocha et al., 1997), which may be strongly influenced by vital effects. The calibrations that are experimental, abiogenic and involve a non-clay phase (Li et al., 1995; Geilert et al., 2012) consist of the precipitation of silica gel from a solution and, therefore, may have very different fractionation factors than precipitation of crystalline quartz due to differences in polymerization and bond strength.

Numerous experimental, empirical and theoretical studies have been performed to determine the magnitude of the oxygen isotope fractionation between quartz and water over a range of temperatures (e.g., Clayton et al., 1972; Shiro and Sakai, 1972; Bottinga and Javoy, 1973; Friedman and O'Neil, 1977; Kawabe, 1978; Matsuhisa et al., 1979; Zheng, 1993; Sharp

and Kirschner, 1994; Hu and Clayton, 2003). Experiments were performed at relatively high temperatures (200-800°C), with a calibration fit to the acquired data. In samples reacted at lower temperatures (200-400°C), calculations of the percentage of isotope exchange show that the runs did not achieve isotopic equilibrium throughout the solid (Clayton et al., 1972; Matsuhisa et al., 1979; Hu and Clayton, 2003). At high temperatures, individual calibrations are in relatively good agreement (<1‰ variability above 400°C). However, extrapolation of calibration curves to lower temperatures, which may be expected in diagenetic conditions, leads to differences in the fractionation factors that are up to 16‰ at 50°C and are even greater at lower temperatures. In addition to uncertainties introduced by extrapolation over large temperature ranges, the "salt effect" of dissolved species must be considered. The fractionation between a mineral and pure water is different from the fractionation between a mineral and water with dissolved species (e.g., Horita et al., 1993a; 1993b; 1995; Hu and Clayton, 2003). Different dissolved species and concentrations may account for the discrepancies between previous calibrations, both for oxygen and silicon isotopes.

Partial exchange at lower-temperatures potentially introduces uncertainty into the calculated fractionation factors. Previous studies have been conducted as exchange reactions of fine-grained powder, with the final product being measured as a bulk sample. If the quartz powder does not fully exchange during the experiment, then there will be a core of each grain that has an inherited value, potentially leading to large errors in the value of experimentally reacted quartz. Attempts to calculate the percent reaction and then extrapolate to the fractionation for 100% reaction have made use of measurements of three isotopes of oxygen (Matsuhisa et al., 1978; Matthews et al., 1983) and the kinetics of partial-exchange reactions (Northrop and Clayton, 1966; Clayton et al., 1989). However, by using a small-beam *in situ*

technique to analyze experimental products, it may be possible to measure only quartz precipitated during the experiment and completely avoid unreacted material.

In this paper, we present oxygen and silicon isotope data for quartz grown in a solution of pH ~12 in 126 days at 250°C on a seed crystal and for the fluid in equilibrium with that quartz. We show that *in situ* stable isotope measurement of experimentally precipitated material is a useful tool for the low-temperature calibration of fractionation factors. We also describe a method for the total reaction and oxygen isotope analysis of 5 µl of fluid, which avoids uncertainties associated with dissolved salts during analysis.

2. Methods

2.1 Quartz growth experimental setup

The reactions that control silica precipitation/dissolution are:

$$SiO_2$$
 (amorph. $silica$) + $2H_2O \Leftrightarrow Si(OH)_4$ ° (1)

$$SiO_2 (quartz) + 2H_2O \Leftrightarrow Si(OH)_4$$
° (2)

$$SiO_2$$
 (amorph. $silica$) + $OH^- + H_2O \Leftrightarrow Si(OH)_3^-$ (3)

$$SiO_2 (quartz) + OH^2 + H_2O \Leftrightarrow Si(OH)_3^2$$
 (4)

$$SiO_2$$
 (amorph. $silica$) + $2OH^- + H_2O \Leftrightarrow Si(OH)_2^{2-}$ (5)

$$SiO_2 (quartz) + 2OH^- + H_2O \Leftrightarrow Si(OH)_2^{2-}$$
 (6)

The equilibrium constants for these reactions vary depending on the solid phase. At pH values <~9, Si(OH)₄ dominates the dissolved Si concentration ([Si]) (Stumm and Morgan, 1981; Wesolowski et al., 2004). At pH values between ~9-11, there is less Si(OH)₄° than Si(OH)₃⁻ and at even higher pH, the dominant species is Si(OH)₂²⁻. The pH in the experiments was controlled by addition of NaOH and the dissolution of amorphous silica and precipitation of quartz (Fig. 4.1).

Three experimental solutions were used in this study: (A) 0.1 mol NaOH/kg water (0.1 m NaOH) with ground silica glass (SG-1) and NaCl; (B) 0.1 m NaOH with ground silica glass; and (C) concentrated sodium silicate solution. There is little temperature dependence on the solubility of silica in a 0.1 m NaOH solution below 300°C (Fig. 4.1A), meaning that the silica-saturated solution can be prepared at room temperature and heated to various working temperatures without affecting the precipitation and dissolution dynamics. For solution B, 50 ml of 0.1 m NaOH was heated in a Teflon beaker on a hotplate at ~80°C with 597 mg ground silica glass (<10 μ m) for 3 days to produce a solution saturated in amorphous silica. To prepare solution A, 16 ml of solution B was transferred to a separate Teflon beaker and 513 mg NaCl was added for a nominal concentration of 0.5 m NaCl. Solution C was prepared by diluting 1.4 g stock sodium silicate solution (Fisher number SS338-1, nominal concentration 13.6 wt% Si) with 98 g N₂-sparged purified, deionized (Milli-Q) water. All solutions were saturated with respect to amorphous silica at a concentration of ~1800 ppm Si (Table 4.1) and oversaturated with respect to quartz (Fig. 4.1B). Solutions A and B had pH ~12, and solution C had pH ~11.

At room temperature, the solutions were divided into individual experimental vessels, as well as aliquots for isotope measurements of reactants. Experiment vessels had a flat-bottomed open Teflon liner inside a stainless steel vessel modified from a VCR vacuum fitting (Anovitz et al., 2004). The dimensions of the metal vessel were 22 mm interior diameter, 47 mm tall (Fig. 4.2). The Teflon liner fit into the metal vessel and the volume of the Teflon liner was ~14 ml.

Each individual run contained 10 ml of fluid, as well as a piece of seed quartz, which acted as a substrate for the growth of new quartz. The quartz seeds used in all the experiments were wafers (5 mm thick, 2-5 mm diameter) cut from a single long crystal with parallel polished faces perpendicular to the C-axis (Fig. 4.3) because growth in the C-direction is much faster than

growth in other orientations (Lander et al., 2008). The parallel faces of each wafer were polished with diamond polishing pads and colloidal alumina to remove any interruptions to growth. Solutions A and B also contained ~100 mg excess ground glass in each reaction vessel. This was to ensure that as silicon was removed from solution as precipitated quartz, amorphous silica would dissolve maintaining the concentration of silicon in solution and decreasing the likelihood of changes to the δ^{30} Si of the fluid due to the precipitation of quartz. The amount of liquid used in each experiment was large in proportion to the amount of precipitated solid material.

Three vessels of each of the three starting solutions were prepared, for a total of nine reaction vessels. Multiple vessels were prepared so that the reaction progress could be monitored over the course of the experiments. After all reactants had been added and the reaction vessels sealed, the vessels were weighed and placed overnight in a vacuum oven at 60°C. The vessels were then cooled and weighed again to confirm that no leaks had occurred. The vessels were then placed in a furnace at 250°C with a digitally controlled temperature of ~±0.5°C. In addition to the nine experiments at 250°C, we also conducted nine experiments at 175°C and seven experiments at 100°C using the same three solutions. Upon inspection after 419 days for 100°C and 219 days for 175°C, no analyzable quartz had precipitated; these experiments are not considered further in this study.

The reaction vessels were left in the furnace for between 20 and 126 days (Table 4.1). At the end of each run, the vessel was removed from the furnace and cooled to room temperature in a water bath in ~45 minutes. When the vessel was cool, it was dried and again weighed to confirm no loss of fluid due to leakage. The vessels were opened and the fluids were immediately flame-sealed in multiple glass capillary tubes of 3-5 μ l each for δ^{18} O analysis. Aliquots were also prepared for δ^{30} Si analysis; because the [Si] of the solutions was much higher

than that needed for multi-collector inductively coupled plasma mass spectrometer (MC-ICP-MS) analysis, solutions were diluted to a nominal concentration of 10 ppm with 71 µl of experimental solution and 20 ml of N₂-sparged Milli-Q water. The remainder of the solution was flame-sealed in glass ampules. Solutions A and B had excess powder, which was also collected. The wafers of seed quartz were removed, rinsed and dried.

2.2 Experimental product characterization

Each wafer of seed quartz was examined in a scanning electron microscope (SEM) at the University of Wisconsin. Immediately after opening the reaction vessels, the wafers were examined in environmental mode (~50 Pa) to describe the morphology of any new growth. After all surfaces were imaged and characterized, the block was cast in epoxy, cut and polished parallel to the c-axis and re-examined to look at the cross-section of new quartz growth. The polished cross-sections were examined by electron backscatter diffraction (EBSD) to confirm the crystallography of the seed and precipitated quartz and to determine crystallographic orientation of both phases. Samples were then coated with a conductive layer of carbon and imaged by cathodoluminescence (CL), secondary electrons (SE) and backscattered electrons (BSE) under high-vacuum SEM. The powders removed from experimental vessels, as well as the ground glass starting material, were measured by X-ray diffraction (XRD) to determine the phases present.

2.3 Isotope analysis of solid material

The δ^{18} O and δ^{30} Si values of experimentally precipitated and seed quartz were measured using the CAMECA ims-1280 secondary ion mass spectrometer (SIMS) at WiscSIMS (Kita et

al., 2009; Valley and Kita, 2009; Heck et al., 2011). Both oxygen and silicon isotope ratios were analyzed using a primary beam of $^{133}\text{Cs}^+$ ions focused to a spot of $\sim \! 10~\mu m$ diameter and $\sim \! 2~\mu m$ deep.

Two different analytical settings were used: (I) a 1.6 nA ¹³³Cs⁺ primary beam with a spot size of $\sim 10 \,\mu m$ for $\delta^{18}O$ measurements and (II) a 2.2 nA $^{133}Cs^+$ primary beam with a spot size of \sim 10 µm for Si measurements. The mass resolving power (MRP, M/ Δ M), measured at 10% peak height, for δ^{18} O and δ^{30} Si analytical conditions was ~2200. The magnetic field strength was held at a stable value using a nuclear magnetic resonance (NMR) probe, which was readjusted every 12 hours. For $\delta^{18}O$ spot analyses, ${}^{16}O^{-}$ and ${}^{18}O^{-}$ ions were simultaneously collected in two Faraday cup detectors with an average ¹⁶O⁻ intensity of 2.7x10⁹ cps and ¹⁶O¹H⁻ was collected in an electron multiplier to monitor hydride interferences and check for traces of water in quartz. For δ^{30} Si spot analyses, 28 Si and 30 Si ions were simultaneously collected in two Faradav cup detectors with an average ³⁰Si⁻ intensity of 1.2x10⁸ cps. Each spot analysis took approximately 4 minutes, which includes 10 s of presputtering to penetrate the carbon coat, ~60 s to stabilize sputtering and automatically center the secondary ions in the field aperture and 80 s (20 cycles of 4 s each) of integrating secondary ions. Detailed descriptions of these analytical conditions and the instrument setup at WiscSIMS have been published previously (Kelly et al., 2007; Kita et al., 2009; Valley and Kita, 2009; Heck et al., 2011).

All data were collected with a standard-sample-standard bracketing procedure of four UWQ-1 standard measurements, 10-16 sample measurements and four UWQ-1 standard measurements. Bracketing standards were used to evaluate the reproducibility of a series of measurements as well as to correct for the instrumental bias. The external spot-to-spot reproducibility of bracketing standards averaged ±0.22‰ (2SD) for oxygen isotope analyses and

 $\pm 0.26\%$ (2SD) for silicon isotope analyses. Raw values of isotope ratios measured by SIMS were corrected to the VSMOW scale for oxygen and the NBS-28 scale for silicon based on values measured for the UWQ-1 bracketing standards (UWQ-1: δ^{18} O=12.33‰, δ^{30} Si=-0.03‰, Kelly et al., 2007; Heck et al., 2011).

The powders from experiment vessels with solutions A and B, as well as the ground-glass starting material, were analyzed for δ^{18} O by laser fluorination on the Finnigan/MAT 251 gassource mass spectrometer in the stable isotope laboratory at the University of Wisconsin using standard methods for the analysis of powders (Spicuzza et al., 1998a; Spicuzza et al., 1998b). These analyses were conducted to determine whether the isotope ratios of powders in the solution were the same as the oriented quartz precipitated on the seed crystal.

2.4 Isotope analysis of fluids

2.4.1 $\delta^{18}O$ analysis of fluids

The fluids to be analyzed for $\delta^{18}O$ were prepared and analyzed following methods similar to those first described by O'Neil and Epstein (1966) and modified by Jabeen and Kusakabe (1997), Barkan and Luz (2005) and Kusakabe and Matsuhisa (2008). Waters were reacted in previously evacuated nickel cylinders with BrF₅ at 230°C for 45 minutes to liberate O₂. The O₂ was converted to CO₂ by reaction with a hot carbon rod and analyzed on a Finnigan/MAT 251 gas source mass spectrometer. The fluorination of water, as opposed to a more traditional equilibration with CO₂ as in Epstein and Mayeda (1953) and Craig (1957), is necessary due to 1) the small volumes of water available (\sim 5 μ l per aliquot) and 2) the effects of NaOH, NaCl and Si(OH)₃ on the fractionation between H₂O and CO₂. The ratio of O in H₂O to O in Si(OH)_X phases in these experiments is large, so by reacting with BrF₅ and liberating all the oxygen in the

water, no fractionation occurs and the $\delta^{18}O$ value measured is a true representation of the $\delta^{18}O$ of the fluid. Measurements of $\delta^{18}O(H_2O)$ were performed for all experiments in which quartz had precipitated, as well as the starting solutions for those experiments. The precision on $\delta^{18}O$ measurements by this method was 0.12% 2SD. A detailed description of the method for these analyses and a diagram of the fluorination apparatus are included in appendix A4.

$2.4.2 \, \delta^{30}$ Si analysis of fluids

The δ^{30} Si of fluids from experiments that precipitated quartz and their starting solutions was measured at Trent University following methods described by Georg et al. (2006). Solutions for δ^{30} Si measurements were processed with a chromatographic column to concentrate Si and analyzed for δ^{30} Si on a Thermo Finnigan Neptune MC-ICP-MS and [Si] by quadrupole ICP-MS. The precision on δ^{30} Si measurements by this method was 0.1‰ 2SD.

3. Results

3.1 Experimental growth

The three solutions used in these experiments resulted in different amounts of quartz precipitation. Solution A (ground glass and NaCl solution) had the largest amount of precipitated quartz, with a maximum thickness of ~250 μ m new quartz after 126 days (Table 4.1, Fig. 4.4A-C). Overgrowths of new quartz precipitated on both polished parallel faces of the wafers in the two solution A experiments (250-2 and 250-3). Solution C (sodium silicate solution) had considerably less growth, with a maximum of ~8 μ m new quartz grown on the seed crystal after 126 days (Table 4.1A, Fig. 4.4D, E). This solution also had loose crystals of doubly terminated α -quartz, which precipitated in solution and settled onto the wafer of seed quartz

(Fig. 4.4F, G). Solution B (ground glass solution) had no measurable growth on any seed crystal face nor crystals precipitated in solution, even after the longest experimental time (126 days). All experimentally grown quartz that precipitated on the seed crystals were confirmed to be in the same orientation as the seed (Fig. 4.4A).

In addition to the experimentally grown quartz, some experiments were found to have precipitated analcime (Table 4.1, Fig. 4.4F, H, I). The sodium necessary for the precipitation of this mineral was readily available from the NaOH, NaCl or sodium-silicate in the solutions. The source of Al was initially puzzling, but it was later found that a small amount of aluminum had been smeared onto some of the wafers of seed quartz from a washer on the saw used to cut them. The identification of analcime was confirmed by spot XRD analysis of individual $\sim 100~\mu m$ crystals (Fig. 4.5).

Powders from solutions A and B and the starting ground glass were measured by powder XRD. A broad low-magnitude peak was observed at low 20, which is consistent with a glass (Fig. 4.6). Peaks consistent with crystalline quartz were measured in each powder that was removed from experimental vessels (Fig. 4.6). The XRD patterns from experimental samples also have a broad low-magnitude peak at low 20.

3.2 Isotope values of solid material

3.2.1 $\delta^{18}O$ values of quartz overgrowth and powders

Two experimental runs from this study (solution A, 86 and 126 days, 250-2 and 250-3, respectively) had macroscopic quartz precipitation that was analyzed by SIMS for δ^{18} O (Table 4.1B). The highest precision and accuracy is achieved in ims-1280 analyses that are within the inner 1 cm of a polished 25 mm mount and analyses from closer to the edge of the mount are of

questionable reliability (Kita et al., 2009; Peres et al., 2013). The wafer of seed quartz for 250-2 cast in epoxy for SIMS analysis was too large for the centrally ideal location, so only the data from the overgrowth of one polished face (end 1) of the wafer was used. The average for overgrowth spots measured in end 1 of 250-2 is $\delta^{18}O = 4.27 \pm 0.06$ % 2SE, n=18. The average for all overgrowth spots from both faces measured in 250-3 is $\delta^{18}O = 4.07 \pm 0.06$ % 2SE, n=87. All SIMS $\delta^{18}O$ values are reported in data repository Table DR4.1.

In addition to the overgrowths of quartz precipitated on the seed crystals, the experiments using solutions A and B had powder that had partially recrystallized to quartz, although the percent recrystallization compared to the original glass is unknown. The $\delta^{18}O$ values of these powders, as well as the ground glass starting material, were measured by laser fluorination and are reported in Table 4.1. The $\delta^{18}O$ of powder from 250-3 is the same within analytical uncertainty as values measured by SIMS for the macroscopic quartz (powder $\delta^{18}O = 4.30 \pm 0.22\%$, SIMS $\delta^{18}O = 4.07 \pm 0.06\%$). The $\delta^{18}O$ value of powder from 250-2 is higher than the SIMS value (7.3% vs. 4.5%). The $\delta^{18}O$ of the starting ground glass is 9.94%.

3.2.2 δ^{30} Si values of quartz overgrowth

The two experiments using solution A that had macroscopic quartz precipitation (250-2, 250-3) were also measured for δ^{30} Si by SIMS. The average δ^{30} Si for overgrowth spots measured in end 1 of 250-2 is 0.21 ± 0.14 ‰ 2SE, n=16. The average for all overgrowth spots measured in 250-3 is 0.43 ± 0.06 ‰ 2SE, n=68. All SIMS δ^{30} Si values are reported in data repository Table DR4.2.

3.3 Isotope values of fluids

3.3.1 $\delta^{18}O$ values of fluids

The $\delta^{18}O$ values of fluids from experiments with macroscopic quartz and the corresponding starting fluids were measured by fluorination (see section 2.4.1 and appendix A4). These values are reported in Tables 4.1B and 4.2. The $\delta^{18}O$ values of the solutions after the experiments are -6.5% and -8.5% for solutions A and C, respectively, and are ~0.5 and 0.3% higher in $\delta^{18}O$ than in the corresponding starting fluids.

$3.3.2 \, \delta^{30}$ Si values of fluids

The δ^{30} Si values of fluids from experiments with macroscopic quartz and the corresponding starting fluids were measured by MC-ICP-MS (see section 2.4.2). These values are reported in Table 4.1C. The δ^{30} Si(fluid) values of 250-2 and 250-3 are -0.30 and -0.15‰, respectively. Although there are no measurements of δ^{30} Si(Qtz) because the overgrowths are too thin, the δ^{30} Si(fluid) of experiment 250-9 is 0.22‰. The δ^{30} Si of the starting solutions A and C are 0.06 and 0.27‰, respectively.

4. Discussion

4.1 Quartz growth rates

It is clear from the amount of quartz precipitated (or lack thereof) in the various reaction vessels in this study that the solution chemistry has a major impact on the growth rate of quartz. Growth rates in previous studies are often quoted as moles/cm²s (e.g., Walderhaug, 1994; Lander et al., 2008). However given the availability of cross-sections of experimental quartz in this study, we report our findings in both μ m/yr (linear growth rate) and moles/cm²s for consistency.

Over the time scale of these experiments (maximum of 126 days), growth from a solution of ground glass and NaOH (solution B) is not observable. This is in sharp contrast to the rates measured in the solution of ground glass, NaOH and NaCl (solution A), where growth rates were as high as 680 µm/yr (235 µm in the 126 day experiment; 9.5 x10⁻¹¹ mol/cm²s). The fast growth rates measured in solution A are similar to those for other experimentally precipitated quartz (Lander et al., 2008) and are much higher than rates estimated for naturally precipitated quartz (Fig. 4.7; Walderhaug, 1994). Walderhaug et al. (1994) made the assumption that the growth of quartz is a continuous process, leading to a possible overestimation of the total duration of precipitation and a corresponding lowering of the growth rate; however, this is still an active debate. A discussion of this assumption is summarized in a review of diagenetic quartz by Worden and Morad (2000). Dove et al. (1994) interpreted fast dissolution rates in solutions with dissolved salts to be due to solvation shells, which can have a large effect on the chemistry of the solid-fluid interaction surface. This may be the same cause of the rapid growth rates in NaCl solutions.

4.2 Recrystallization of powders

In addition to the quartz that was precipitated in three of the reaction vessels, extra ground glass that was placed into the vessels as a source of silicon recrystallized to quartz during the runs is seen in XRD patterns (Fig. 4.6). The measurements were made with powder packed into glass capillaries, so it is unclear whether the broad glass signal for the starting material and in the experiments is from the powder itself or from the capillary tube. It is clear, however, that the experiments do contain sharp quartz diffraction peaks, whereas the starting material does not

(Fig. 4.6), indicating that a significant amount of quartz crystallized in the powder in these experiments.

4.3 $\delta^{18}O$ values of powders

The similarity between the $\delta^{18}O$ of macroscopic quartz and from residual powder in 250-3 suggests that both phases represent the same fractionation factors for quartz-water and that the powders may contain useful information for experiments that had no quartz growth. However it cannot be guaranteed that no original ground glass remained in the powdered samples, which would bias the measured values away from equilibrium precipitation.

The ground glass, which was included in solutions A and B, has a $\delta^{18}O$ of 9.94‰. The powder from experiment 250-2 (same starting solution as 250-3) has a $\delta^{18}O$ ~3‰ higher than the quartz measured by SIMS. Experiment 250-2 was in the furnace for 86 days, as compared to 250-3, which was in the furnace for 126 days. The fact that the powder from this experiment has a $\delta^{18}O$ value, which is intermediate between the precipitated quartz and the starting material, suggests that this experiment, which ran for a shorter amount of time, has a higher proportion of unreacted starting glass included in the bulk powder. This underlines the importance of measuring solid material, which is definitively precipitated in the experiment for use in calculating fractionation factors. Even fine grained (<10 μ m) amorphous silica in a reaction for 86 days at 250°C did not fully equilibrate with the fluid (Fig. 4.8).

4.4 $\delta^{18}O$ values of starting and ending fluids

The <0.5‰ increase in $\delta^{18}O$ from starting to ending liquid (Table 4.1B) may be due to minor corrosion of the stainless steel vessel with the vapor phase, minor evaporation and

condensation between the liner and vessel or the precipitation of quartz. The fact that the $\delta^{18}O$ and $\delta^{30}Si$ of precipitated quartz does not vary systematically from early to late quartz suggests that the isotopic values of the fluid did not change during, or due to, quartz precipitation. The shift in $\delta^{18}O$ during the experiment had little effect on the calculation of fractionation factors. The important phases for fractionation calibration are the final quartz and final fluid.

4.5 Quartz-water fractionation

The fractionation factor (α) for a pair of phases is defined as

$$\alpha_{i-j} = \frac{R_i}{R_j} \tag{7}$$

where i and j represent the phases of interest and R is the isotopic ratio (i.e., $^{18}\text{O}/^{16}\text{O}$ or $^{30}\text{Si}/^{28}\text{Si}$) in that phase. The temperature dependence of the fractionation can be simplified to

$$10^3 \ln \alpha = A \frac{10^6}{T^2} \tag{8}$$

where A is a constant and T is the temperature in Kelvin. For small differences in the values of measured species,

$$10^{3} \ln \alpha(i-j) \approx \Delta^{18} O(i-j) = \delta^{18} O(i) - \delta^{18} O(j)$$
 (9)

and

$$10^{3} ln\alpha(i-j) \approx \Delta^{30} Si(i-j) = \delta^{30} Si(i) - \delta^{30} Si(j) \qquad (10)$$

4.5.1 $\alpha^{18}O(Qtz-H_2O)$ calibration

The two vessels from this set of experiments that had macroscopic quartz precipitation can be used to calculate equilibrium fractionation factors between quartz and water at 250°C.

Experiments 250-2 and 250-3 have $\Delta^{18}O(\text{Qtz-H}_2O)$ values of 10.64 \pm 0.10‰ 2 σ ($\sqrt{\left(2SE_{Qtz}\right)^2 + \left(2SD_{H_2O}\right)^2}$) and 10.59 \pm 0.23‰ 2 σ , respectively (Fig. 4.9).

As seen in Figure 4.9, there is a large discrepancy between calibrations of 1000lnα¹⁸O(Qtz-H₂O) from different studies. Two calibrations of note that are in close agreement with this study are the lowest temperature experimental calibration (200-500°C calibration of Clayton et al., 1972) and a combined estimate from quartz-calcite and calcite-water (Sharp and Kirschner, 1994). At 250°C, Δ¹⁸O(Qtz-H₂O) is 9.45% calculated from Clayton et al. (1972) and 10.44% calculated from Sharp and Kirschner (1994). The close agreement between this study and that of Sharp and Kirschner (1994) is encouraging, but care must be taken because their calibration combines the calcite-water fractionation of O'Neil et al. (1969), for which the effect of dissolved carbonate vs. dissolved silicate may have a large impact. While the results of this study are only for a single temperature, the close agreement between the values calculated here and those for two previous calibrations shows that *in situ* measurement of solid material from low-temperature experiments will be a valuable tool for constraining fractionation factors.

$4.5.2 \ \alpha^{30}$ Si(Qtz-fluid) calibration

There are currently no experimental calibrations for Δ^{30} Si(Qtz-fluid). Estimates that exist for the silicon isotope fractionation between silica and water are based on empirical studies of natural quartz and fluid from various locations (e.g., Douthitt, 1982; Georg et al., 2007), on measurements of biogenic silica from sponges or diatoms (Douthitt, 1982; De La Rocha et al., 1997; De La Rocha, 2003) or on experimentally precipitated silica gel (Li et al., 1995) and amorphous silica (Geilert et al., 2012). One recent study has tried to constrain the fractionation

factors by measuring the δ^{30} Si of the starting fluid and the final fluid after it has passed through a flow reactor with seed crystals and assuming that the difference is due to the precipitation of amorphous silica. The largest Δ^{30} Si(silica-fluid) value from this experiment is -2.1‰ at 10°C, although these authors interpret their fractionation values as not representing equilibrium, (Geilert et al., 2012; Geilert, personal communication). The Si concentrations measured in the present study (Table 4.1) are very close to the equilibrium quartz curves plotted in Figure 4.1. To our knowledge, no studies have directly measured quartz grown experimentally and the fluid from which it precipitated.

The Δ^{30} Si(Qtz-fluid) values for experiments 250-2 and 250-3 are 0.47 ‰ and 0.58 ‰, respectively. These values are considerably different from previously published estimates, both in magnitude and the sign of fractionation (Fig. 4.10). One possible explanation for this difference is that the high pH values of the solutions in this study lead to the fractionation of silicon between quartz and highly dissociated aqueous silica polymers (H₂SiO₂²⁻, vs. H₃SiO₃⁻ or H₄SiO₄). The polymerization of aqueous silica at high pH evidently has a large effect on quartz growth rates (Fig. 4.1), but whether this affects fractionation is unknown. As silicic acid dissociates at high pH, OH molecules are lost, which may affect the Si-O bond that will exchange with the growing quartz lattice. Previous Δ^{30} Si calibrations have been performed at circumneutral pH. Another possibility is that the fast growth rates in this study may not allow isotopic equilibration between the quartz and water. If quartz precipitated in non-equilibrium growth, the quartz may be isotopically zoned due to changes in availability of Si and O during the experiment. However, the lack of zonation in $\delta^{30}Si$ and $\delta^{18}O$ within the quartz in these experiments suggests that the experiments were, in fact, in isotopic equilibrium. A third explanation for the difference between this and previous studies is that all previous experimental

studies have investigated precipitated amorphous silica or silica gel, where the bonding characteristics and therefore fractionation may be quite different for quartz.

5. Conclusion

Quartz was successfully precipitated under experimental conditions of high pH with NaCl and ground glass at 250°C in less than four months in a furnace. The new quartz was analyzed by SIMS and found to be homogenous in both $\delta^{18}O$ and $\delta^{30}Si$. The fluids from these experiments were also analyzed for oxygen isotope ratios using fluorination of water. Silicon isotope ratios for fluids were measured by MC-ICP-MS, and a quartz-fluid fractionation factor was calculated for each isotope system. The $\Delta^{18}O(Qtz-H_2O)$ at 250°C is 10.6‰, within uncertainty of previous calibrations. This difference may be due to the incomplete exchange or the incorporation of primary quartz cores in bulk measurements of previous experiments at low temperatures. The $\Delta^{30}Si(Qtz$ -fluid) value for these experiments is +0.55‰, which is between 0.5 and 6‰ higher than previously published values, which range from $\Delta^{30}Si(Qtz$ -fluid) = 0 to -5.5‰). No other studies have directly measured quartz and fluid from the same experiment.

While these experiments were only at a single temperature, the close agreement of Δ^{18} O successfully demonstrates the usefulness of analyzing experimental products with *in situ* measurements. All previous calibrations have relied on bulk measurements of fine material that was assumed to have fully equilibrated with a fluid, but might have some residual unreacted cores. By targeting only quartz that was definitively grown during the experiment using the *in situ* SIMS technique, confidence can be gained in the true phase being analyzed. The method described here can and should be applied to numerous systems of interest at low temperatures,

where fractionation calibrations have been hampered by slow growth rates and bulk measurement techniques.

Acknowledgements

The WiscSIMS laboratory is supervised by Noriko Kita and maintained by Jim Kern. Brian Hess prepared sample mounts and helped with preparation of quartz chips. Funding was provided by DOE (93ER14389) to JWV and Graduate Student Research grants from the MGPV Division of GSA and the GSA Foundation to ADP. Effort by LMA was supported by research sponsored by the Division of Chemical Sciences, Geosciences, and Biosciences, Office of Basic Energy Sciences, U.S. Department of Energy. The WiscSIMS laboratory is partially funded by NSF (EAR-1053466).

References Cited

- Anovitz, L.M., Elam, J.M., Riciputi, L.R., and Cole, D.R., 2004, Isothermal time-series determination of the rate of diffusion of water in Pachuca obsidian: Archaeometry, v. 46, p. 301-326.
- Barkan, E., and Luz, B., 2005, High precision measurements of $^{17}O/^{16}O$ and $^{18}O/^{16}O$ ratios in H₂O: Rapid Communications in Mass Spectrometry, v. 19, p. 3737-3742.
- Bottinga, Y., and Javoy, M., 1973, Comments on Oxygen Isotope Geothermometry: Earth and Planetary Science Letters, v. 20, p. 250-265.
- Chacko, T., Cole, D.R., and Horita, J., 2001, Equilibrium oxygen, hydrogen and carbon isotope fractionation factors applicable to geologic systems, *in* Valley, J.W., and Cole, D.R., eds., Stable Isotope Geochemistry, Volume 43: Reviews in Mineralogy and Geochemistry 43, Mineralogical Society of America, p. 1-81.
- Clayton, R.N., Mayeda, T.K., and O'Neil, J.R., 1972, Oxygen Isotope-Exchange between Quartz and Water: Journal of Geophysical Research, v. 77, p. 3057-3067.
- Clayton, R.N., Goldsmith, J.R., and Mayeda, T.K., 1989, Oxygen Isotope Fractionation in Quartz, Albite, Anorthite and Calcite: Geochimica et Cosmochimica Acta, v. 53, p. 725-733.
- Craig, H., 1957, Isotopic standards for carbon and oxygen and correction factors for mass-spectrometric analysis of carbon dioxide: Geochimica et Cosmochimica Acta, v. 12, p. 133-149.
- De La Rocha, C.L., Brzezinski, M.A., and DeNiro, M.J., 1997, Fractionation of silicon isotopes by marine diatoms during biogenic silica formation: Geochimica et Cosmochimica Acta, v. 61, p. 5051-5056.
- De La Rocha, C.L., 2003, Silicon isotope fractionation by marine sponges and the reconstruction of the silicon isotope composition of ancient deep water: Geology, v. 31, p. 423-426.
- Douthitt, C.B., 1982, The Geochemistry of the Stable Isotopes of Silicon: Geochimica et Cosmochimica Acta, v. 46, p. 1449-1458.
- Dove, P.M., 1994, The Dissolution Kinetics of Quartz in Sodium Chloride Solutions at 25°C to 300°C: American Journal of Science, v. 294, p. 665-712.
- Epstein, S., and Mayeda, T., 1953, Variation of O¹⁸ content of waters from natural sources: Geochimica et Cosmochimica Acta, v. 4, p. 213-224.
- Friedman, I., and O'Neil, J.R., 1977, Compilation of stable isotope fractionation factors of geochemical interest: United States Geological Survey professional paper 440-KK, Washington, D.C., 67 p.
- Geilert, S., van Bergen, M.J., Vroon, P.Z., and Van Cappellen, P., 2012, Si isotope fractionation during silica precipitation in flow-through experiments: Mineralogical Magazine, v. 76, p. 1746.

- Georg, R.B., Reynolds, B.C., Frank, M., and Halliday, A.N., 2006, New sample preparation techniques for the determination of Si isotopic compositions using MC-ICPMS: Chemical Geology, v. 235, p. 95-104.
- Georg, R.B., Reynolds, B.C., West, A.J., Burton, K.W., and Halliday, A.N., 2007, Silicon isotope variations accompanying basalt weathering in Iceland: Earth and Planetary Science Letters, v. 261, p. 476-490.
- Heck, P.R., Huberty, J.M., Kita, N.T., Ushikubo, T., Kozdon, R., and Valley, J.W., 2011, SIMS analyses of silicon and oxygen isotope ratios for quartz from Archean and Paleoproterozoic banded iron formations: Geochimica et Cosmochimica Acta, v. 75, p. 5879-5891.
- Horita, J., Cole, D.R., and Wesolowski, D.J., 1993a, The Activity-Composition Relationship of Oxygen and Hydrogen Isotopes in Aqueous Salt-Solutions .2. Vapor-Liquid Water Equilibration of Mixed Salt-Solutions from 50 to 100-Degrees-C and Geochemical Implications: Geochimica et Cosmochimica Acta, v. 57, p. 4703-4711.
- Horita, J., Wesolowski, D.J., and Cole, D.R., 1993b, The Activity-Composition Relationship of Oxygen and Hydrogen Isotopes in Aqueous Salt-Solutions .1. Vapor-Liquid Water Equilibration of Single Salt-Solutions from 50-Degrees-C to 100-Degrees-C: Geochimica et Cosmochimica Acta, v. 57, p. 2797-2817.
- Horita, J., Cole, D.R., and Wesolowski, D.J., 1995, The Activity Composition Relationship of Oxygen and Hydrogen Isotopes in Aqueous Salt-Solutions. 3. Vapor Liquid Water Equilibration of Nacl Solutions to 350°C: Geochimica et Cosmochimica Acta, v. 59, p. 1139-1151.
- Hu, G.X., and Clayton, R.N., 2003, Oxygen isotope salt effects at high pressure and high temperature and the calibration of oxygen isotope geothermometers: Geochimica et Cosmochimica Acta, v. 67, p. 3227-3246.
- Jabeen, I., and Kusakabe, M., 1997, Determination of $\delta^{17}O$ values of reference water samples VSMOW and SLAP: Chemical Geology, v. 143, p. 115-119.
- Kawabe, I., 1978, Calculation of Oxygen Isotope Fractionation in Quartz-Water System with Special Reference to Low-Temperature Fractionation: Geochimica et Cosmochimica Acta, v. 42, p. 613-621.
- Kelly, J.L., Fu, B., Kita, N.T., and Valley, J.W., 2007, Optically continuous silcrete quartz cements of the St. Peter Sandstone: High precision oxygen isotope analysis by ion microprobe: Geochimica et Cosmochimica Acta, v. 71, p. 3812-3832.
- Kita, N.T., Ushikubo, T., Fu, B., and Valley, J.W., 2009, High precision SIMS oxygen isotope analysis and the effect of sample topography: Chemical Geology, v. 264, p. 43-57.
- Kusakabe, M., and Matsuhisa, Y., 2008, Oxygen three-isotope ratios of silicate reference materials determined by direct comparison with VSMOW-oxygen: Geochemical Journal, v. 42, p. 309-317.

- Lander, R.H., Larese, R.E., and Bonnell, L.M., 2008, Toward more accurate quartz cement models: The importance of euhedral versus noneuhedral growth rates: American Association of Petroleum Geologists Bulletin, v. 92, p. 1537-1563.
- Li, Y., Ding, T., and Wan, D., 1995, Experimental study of silicon isotope dynamic fractionation and its application in geology: Chinese Journal of Geochemistry, v. 14, p. 212-219.
- Matsuhisa, Y., Goldsmith, J.R., and Clayton, R.N., 1978, Mechanisms of Hydrothermal Crystallization of Quartz at 250-Degrees-C and 15 Kbar: Geochimica et Cosmochimica Acta, v. 42, p. 173-182.
- Matsuhisa, Y., Goldsmith, J.R., and Clayton, R.N., 1979, Oxygen Isotopic Fractionation in the System Quartz-Albite-Anorthite-Water: Geochimica et Cosmochimica Acta, v. 43, p. 1131-1140.
- Matthews, A., Goldsmith, J.R., and Clayton, R.N., 1983, Oxygen Isotope Fractionations Involving Pyroxenes the Calibration of Mineral-Pair Geothermometers: Geochimica et Cosmochimica Acta, v. 47, p. 631-644.
- Northrop, D.A., and Clayton, R.N., 1966, Oxygen-Isotope Fractionations in Systems Containing Dolomite: Journal of Geology, v. 74, p. 174-196.
- O'Neil, J.R., and Epstein, S., 1966, A Method for Oxygen Isotope Analysis of Milligram Quantities of Water and Some of Its Applications: Journal of Geophysical Research, v. 71, p. 4955-4961.
- O'Neil, J.R., Clayton, R.N., and Mayeda, T.K., 1969, Oxygen Isotope Fractionation in Divalent Metal Carbonates: Journal of Chemical Physics, v. 51, p. 5547-5558.
- Peres, P., Kita, N.T., Valley, J.W., Fernandes, F., and Schuhmacher, M., 2013, New sample holder geometry for high precision isotope analyses: Surface and Interface Analysis, v. 45, p. 553-556.
- Sharp, Z.D., and Kirschner, D.L., 1994, Quartz-calcite oxygen isotope thermometry: A calibration based on natural isotopic variations: Geochimica et Cosmochimica Acta, v. 58, p. 4491-4501.
- Shiro, Y., and Sakai, H., 1972, Calculation of Reduced Partition-Function Ratios of α -, β -Quartzs and Calcite: Bulletin of the Chemical Society of Japan, v. 45, p. 2355-2359.
- Spicuzza, M.J., Valley, J.W., Kohn, M.J., Girard, J.P., and Fouillac, A.M., 1998a, The rapid heating, defocused beam technique: a CO_2 -laser-based method for highly precise and accurate determination of $\delta^{18}O$ values of quartz: Chemical Geology, v. 144, p. 195-203.
- Spicuzza, M.J., Valley, J.W., and McConnell, V.S., 1998b, Oxygen isotope analysis of whole rock via laser fluorination; an air-lock approach: Abstracts with Programs Geological Society of America, v. 30, p. 80.
- Stumm, W., and Morgan, J.J., 1981, Aquatic chemistry: an introduction emphasizing chemical equilibria in natural watersNew York, Wiley, 780 p.
- Urey, H.C., 1947, The thermodynamic properties of isotopic substances: Journal of the Chemical Society, p. 562-581.

- Valley, J.W., and Kita, N.T., 2009, *In situ* oxygen isotope geochemistry by ion microprobe, *in* Fayek, M., ed., Secondary Ion Mass Spectrometry in the Earth Sciences: Gleaning the big picture from a small spot: Short Course Series 41, Mineralogical Association of Canada, p. 19-63.
- Walderhaug, O., 1994, Precipitation Rates for Quartz Cement in Sandstones Determined by Fluid-Inclusion Microthermometry and Temperature-History Modeling: Journal of Sedimentary Research Section a-Sedimentary Petrology and Processes, v. 64, p. 324-333.
- Wesolowski, D.J., Ziemniak, S.E., Anovitz, L.M., Machesky, M.L., Bénézeth, P., and Palmer, D.A., 2004, Solubility and surface adsorption characteristics of metal oxides, *in* Palmer, D.A., Fernández-Prini, R., and Harvey, A.H., eds., Aqueous Systems at Elevated Temperatures and Pressures: Physical Chemistry in Water, Steam and Hydrothermal Solutions, Elsevier, p. 492-595.
- Worden, R.H., and Morad, S., 2000, Quartz cementation in oil field sandstones: a review of the key controversies, *in* Worden, R., and Morad, S., eds., Quartz cemenation in sandstones: International Association of Sedimentologists Special publication 29: Malden, MA, Blackwell Science, p. 1-20.
- Zheng, Y.F., 1993, Calculation of Oxygen Isotope Fractionation in Anhydrous Silicate Minerals: Geochimica et Cosmochimica Acta, v. 57, p. 1079-1091.
- Ziegler, K., Chadwick, O.A., Kelly, E.F., Brzezinski, M.A., and DeNiro, M.J., 2000, Silicon isotope fractionation during weathering and soild formation: Experimental results: Journal of Conference Abstracts, v. 5, p. 1135.

Figures

Figure 4.1. A) Concentration of dissolved silica calculated as a function of temperature for varying concentrations of NaOH in aqueous solution. Curves are based on equilibrium constants from Wesolowski et al. (2004) for equations (1) – (6). Solid lines represent the solubility of quartz in equilibrium with a given fluid; dashed lines represent the solubility of amorphous silica (in these experiments ground glass) with a given fluid. Note the independence of temperature and solubility for 0.1*m* NaOH compared to the other curves. B) Concentration of dissolved silica as a function of pH or NaOH concentration for varying temperatures. Temperature and pH conditions below a given curve will result in under saturation and dissolution of that phase, whereas conditions above the curve will result in over saturation and precipitation of that phase. For example, the grey shaded region between the quartz and amorphous silica curves at 250°C will result in precipitation of quartz, with amorphous silica in solution as the source of silicon for quartz precipitation. Boxes in each panel represent the approximate conditions of these experiments.

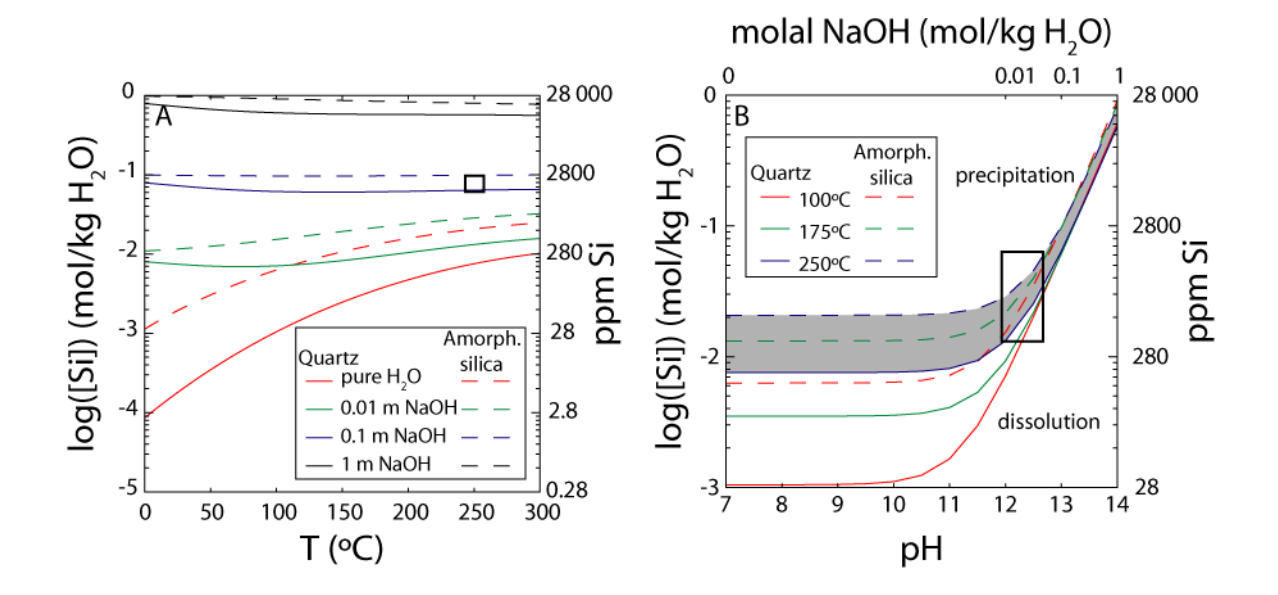


Figure 4.2. Photographs of experimental vessels. A) Fully assembled vessel. B) Individual pieces of vessel. The copper gasket is placed between the sealing surfaces of the main tube and the top threaded plug; the Teflon cup containing the quartz wafer, fluid and powder (solutions A and B) was placed inside the main tube and the nut was tightened onto the plug. The vessels were placed in the furnace in the orientation of panel A. Scale bar in each panel is 1 cm.





Figure 4.3. Photographs of the quartz crystal used as a growth substrate. A) The crystal was ~16 cm long and provided oriented individual wafers of quartz cut perpendicular to the c-axis. B) Quartz crystal mounted in epoxy and polished using colloidal alumina. C) After polishing, the crystal was sectioned to provide multiple seed blocks. Seed blocks that had large fractures, visible scratches or apparent inclusions were not used.

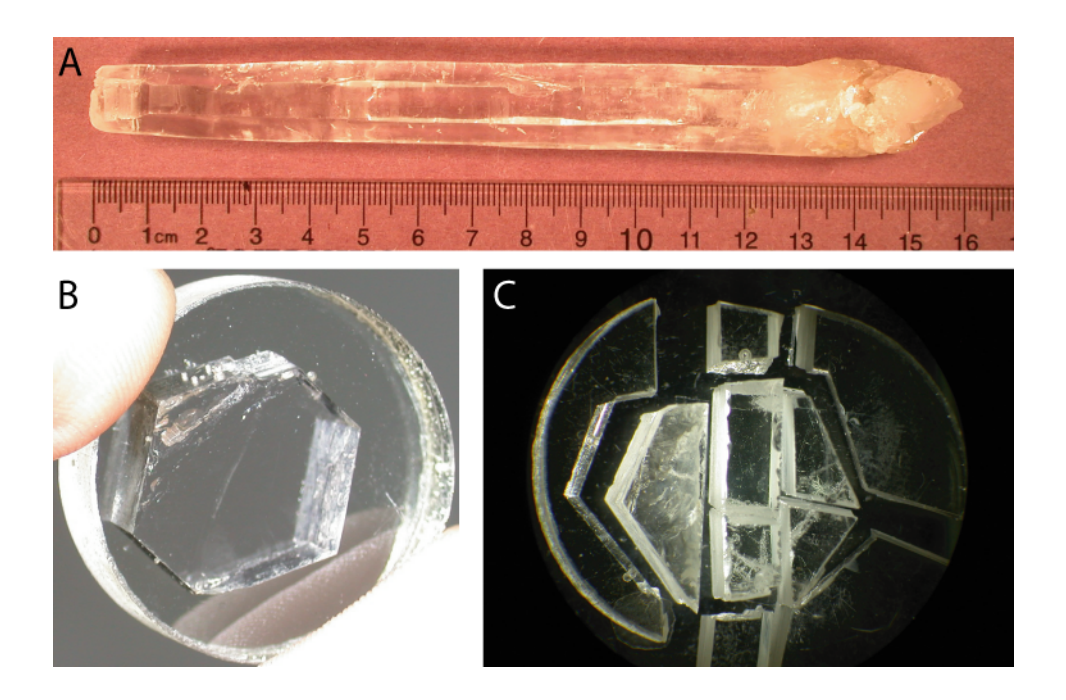


Figure 4.4 (next page). Photomicrographs of experimentally precipitated quartz and analcime. All photographs were taken using the scanning electron microscope (SEM). A) Surface of experimentally precipitated quartz from experiment number 250-3 (Solution A, 250°C, 126 days). Flat area in upper left of image is the polished surface of the seed crystal. Large area in center of image is experimentally precipitated quartz. Note the many individual peaks of quartz crystals with the same orientation, controlled by the orientation of the seed. The dashed line represents the approximate location of the cross-section shown in D and E. B and C) Cathodoluminescence (CL) and backscattered electron (BSE) images of a section of experiment number 250-3 polished cross-section (box in D and E). The bright, experimentally grown quartz is easily distinguished by CL from the dark seed crystal. Notches (N) between quartz peaks (P) appear to be controlled by "dust," which may be powder from the excess starting material. Quartz peaks are pyramidal terminations of individual quartz crystals parallel to the C-axis (also seen in A). D and E) CL and BSE images of cross-section along the dashed line shown in A. The maximum thickness of the new quartz is 235 µm. White boxes represent area shown in B and C. F and G) CL and BSE images of experiment number 250-9 (Solution C, 250°C, 126 days) polished cross-section. The seed crystal is distinguishable from the precipitated quartz in this image, but the thickness of new quartz is only 8 µm. F and G show only one corner of the seed crystal, but the growth is continuous across the entire originally polished surface. H) Surface image of the polished face perpendicular to the c-axis of 250-9 showing phases precipitated in solution. Q = doubly terminated quartz crystals; A = analcime. I) BSE image of 250-9 polished cross-section. This surface is perpendicular to the surface in F&G. The seed crystal is present, but in this orientation there is no quartz overgrowth seen. J) Surface of 250-9 showing clusters of analcime crystals. K) BSE image of 250-9 polished cross-section. A thin overgrowth in the same orientation as F and G is present in this image. Large analcime crystals are slightly darker than quartz seed.

Figure 4.4

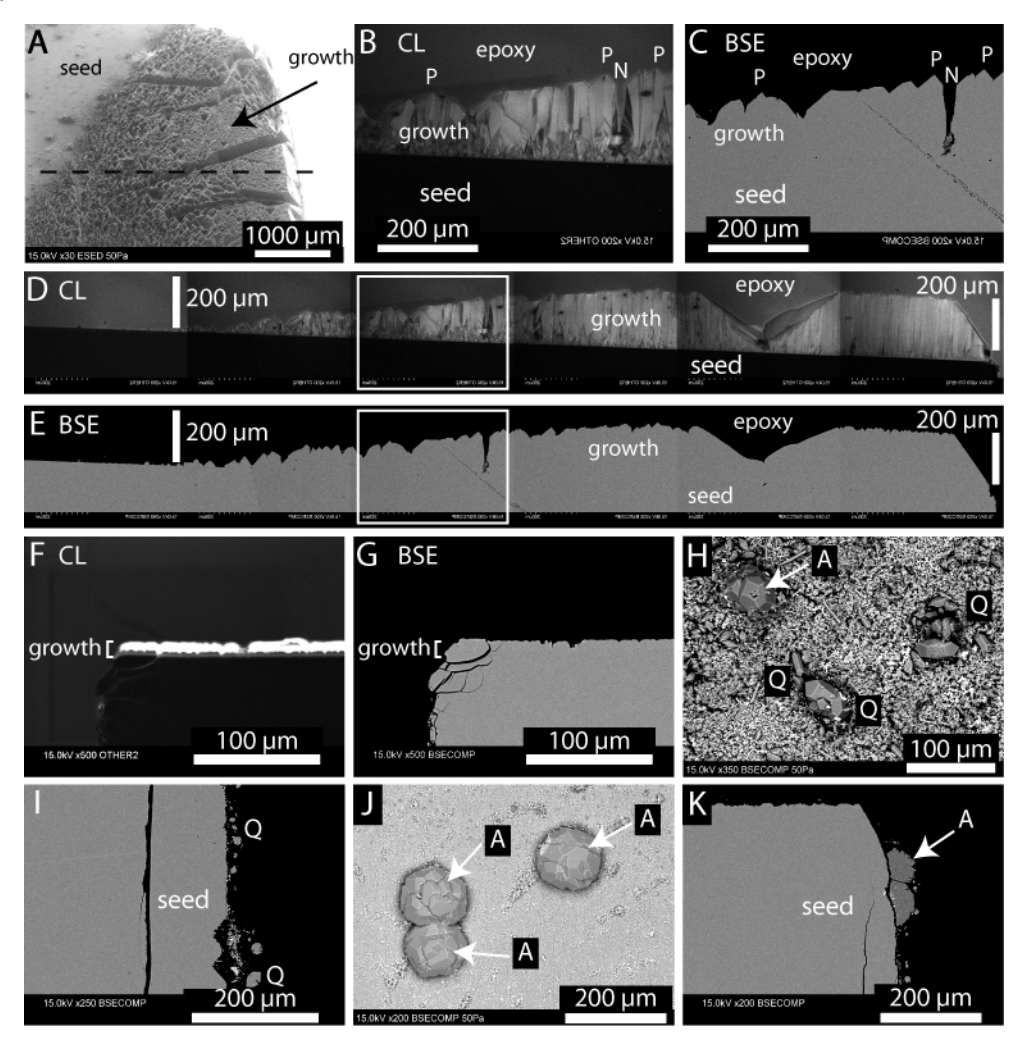


Figure 4.5. Spot X-ray diffraction (XRD) patterns of analcime clusters mounted in epoxy. Each curve is an analysis on a different crystal cluster from the same experiment, created by rotating epoxy mount. Peaks are labeled for crystallographic planes in analcime (A). Large broad peak between 5-10° 2 θ is due to samples being cast in epoxy; beam size (140 to 200 μ m) was much larger than individual crystal clusters (~100 μ m). Curves are vertically offset from each other, but have the same vertical scale.

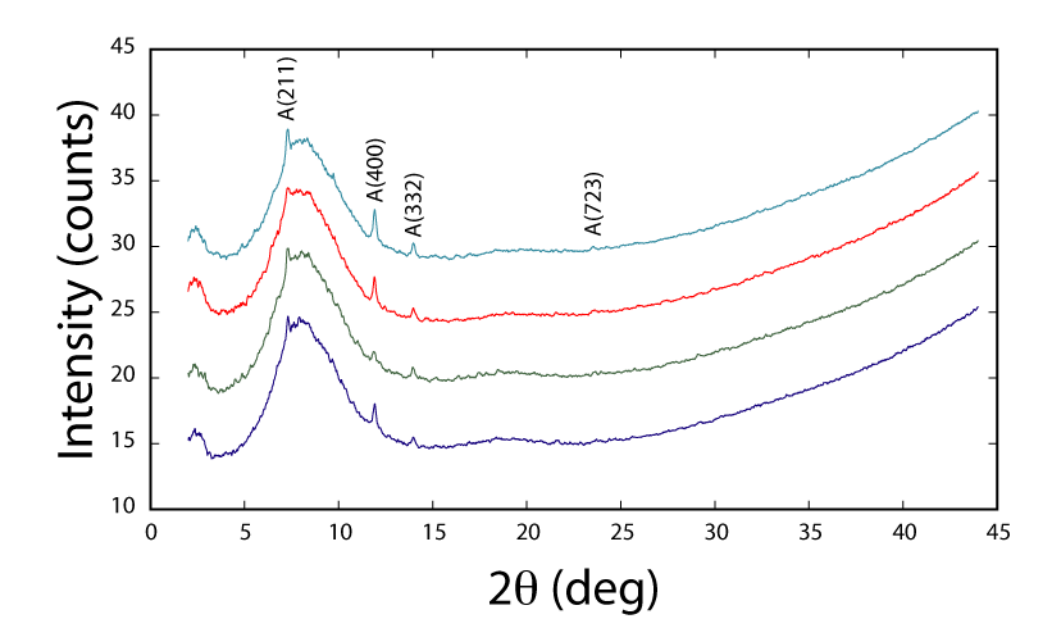


Figure 4.6. Powder XRD patterns for starting glass (SG-1) and powders after removal from experiments. Peaks are labeled for crystallographic planes in alpha-quartz (Q) and halite (H). SG-1 = silica glass ground for starting material. Note broad peak at low 2θ showing presence of glass as well as lack of sharp diffraction peaks for any phase. 250-2 and 250-3 are experiments from solution A, which has NaCl, leading to peaks for halite. A broad peak is present in the background of the experimental curves, but it is much lower magnitude than for the starting material. Curves are vertically offset from each other, but have the same vertical scale.

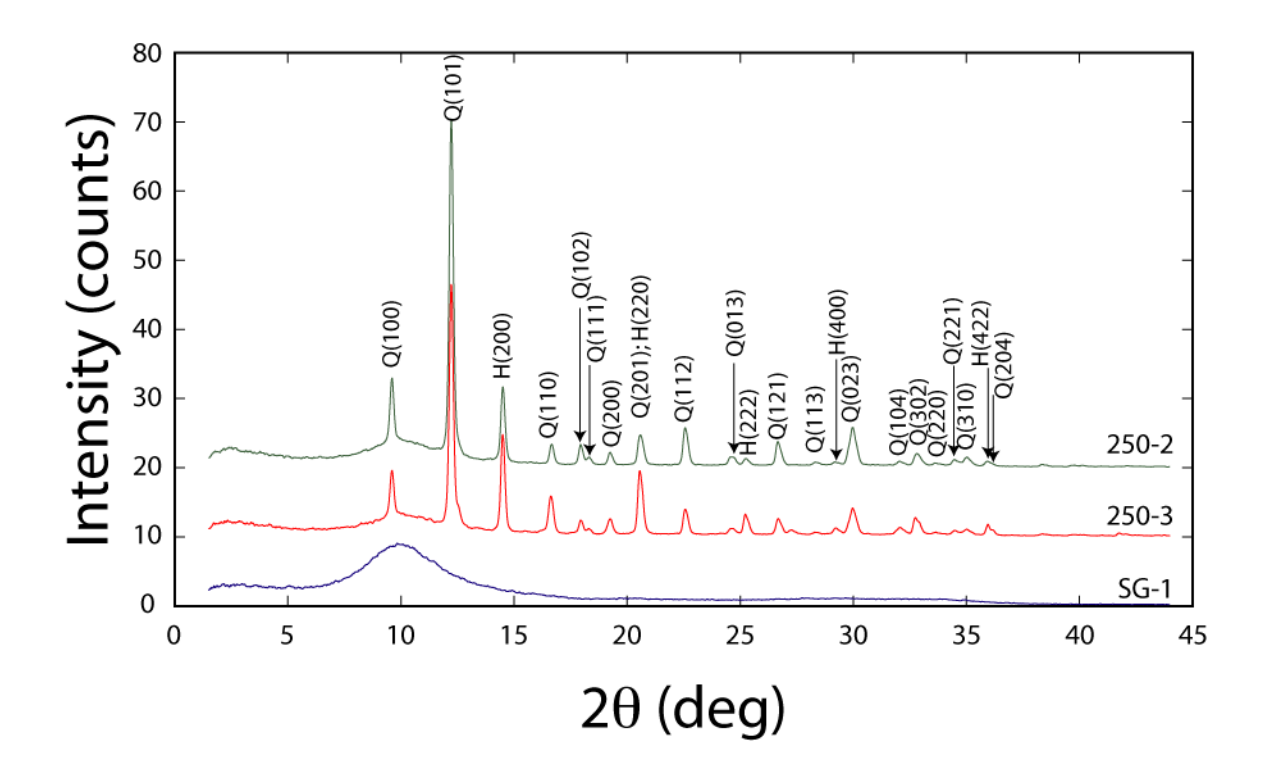


Figure 4.7. Comparison of growth rates estimated from natural quartz samples (Walderhaug, 1994) and experimentally precipitated quartz (this study; Lander et al., 2008) as a function of temperature. Solutions A and C are from this study. Growth rates for experiments are much higher than those derived for natural samples. See text for discussion.

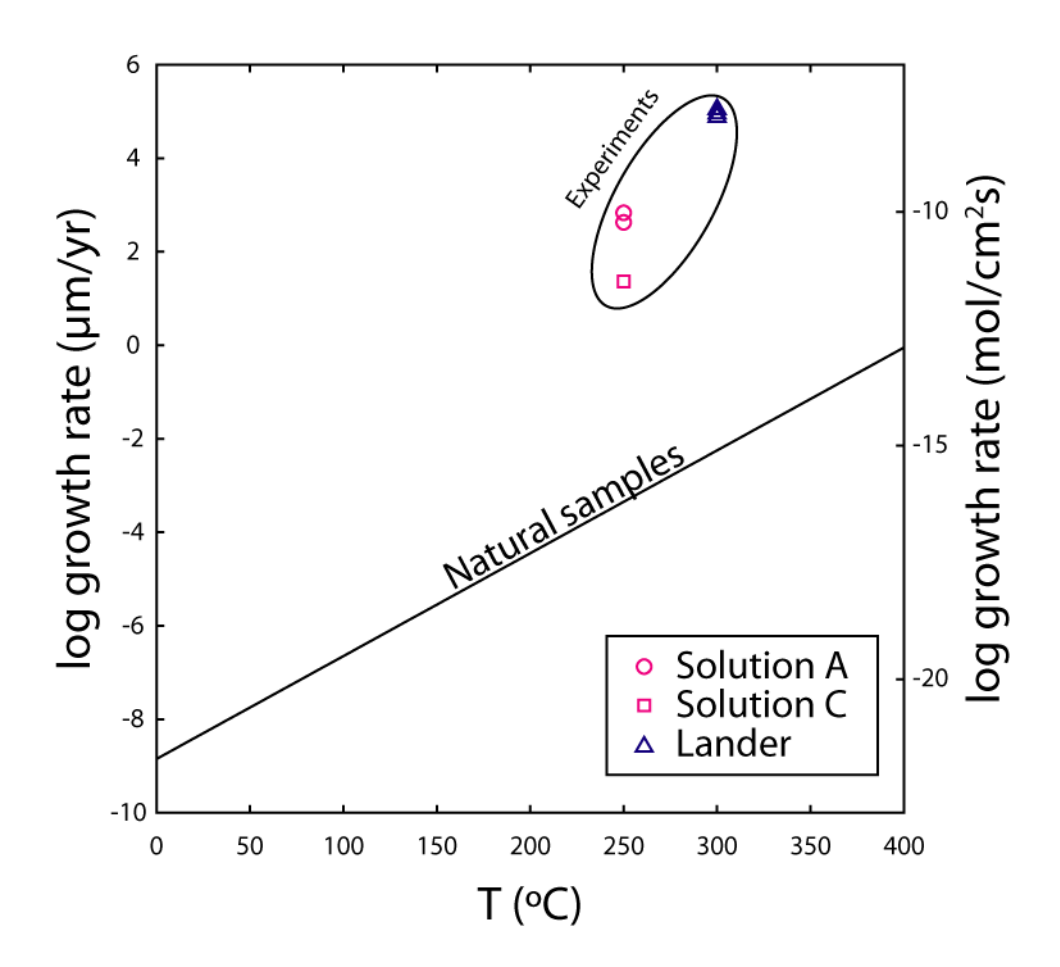
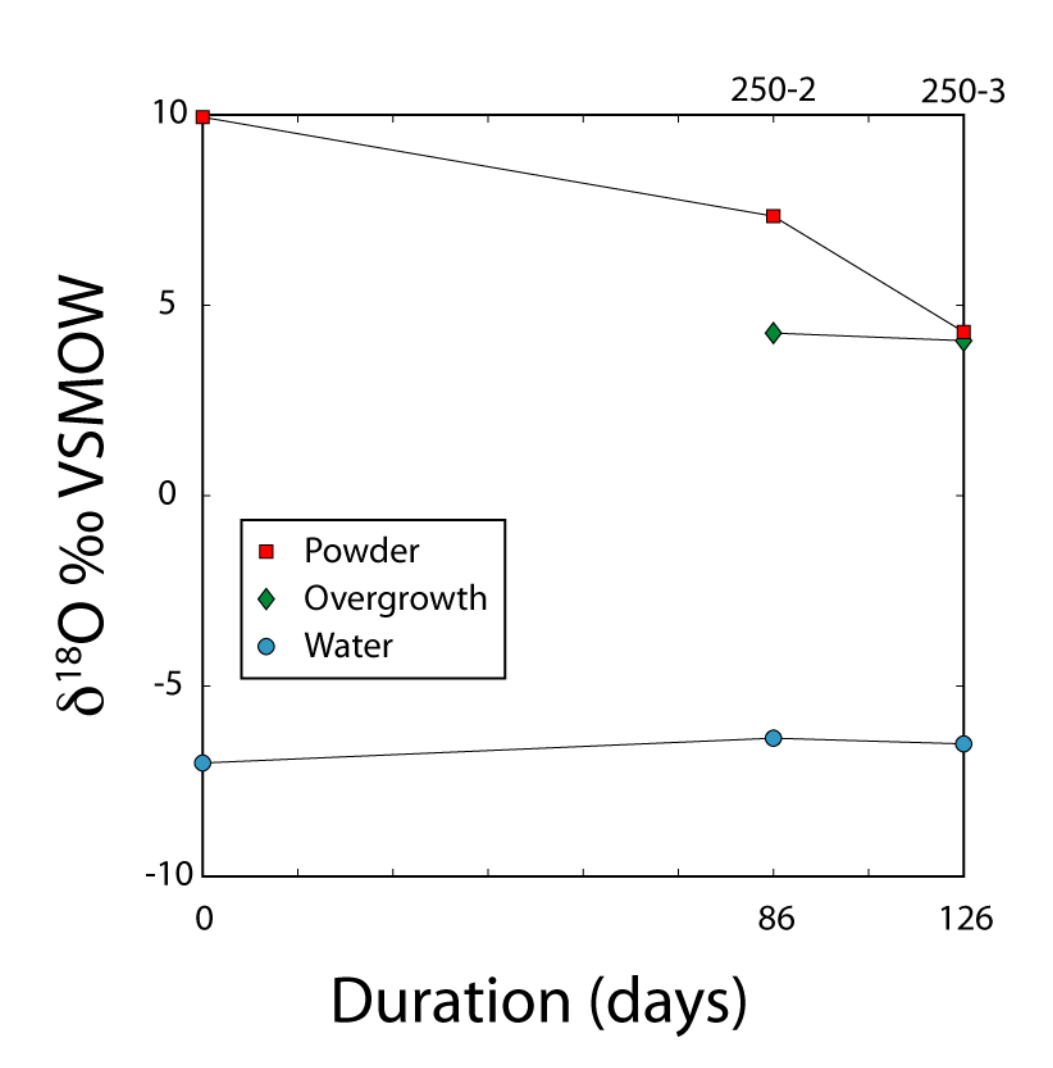


Figure 4.8. Oxygen isotope composition of experimental products and starting material from solution A as a function of experiment duration. Values at 0 days are the δ^{18} O of starting powder and solution A. Numbers above the top axis are experiment numbers. Overgrowth δ^{18} O is the value measured by SIMS; the difference between this and δ^{18} O(H₂O) reflects the equilibrium fractionation between quartz and water. The δ^{18} O of powder from experiment 250-2 shows an incomplete reaction intermediate between starting material of ~10‰ and the equilibrium value of ~4‰; the powder in 250-3 has fully reacted.



Comparison of calibrations of quartz-water oxygen isotope Figure 4.9 (next page). fractionation. Bold line segments for previous studies represent the temperature range over which experiments were conducted. Dashed lines are extrapolations representing experimental calibrations. Dashed-dotted lines are calibrations based on theoretical calculations of fractionation, or of recalculations of previously published experiments with different assumptions. Solid black line is fit through experimental data of this study and 0% at infinite temperature (10⁶/T²=0). Curves are plotted using fractionation factors published in each study and are extrapolated to 50°C, a temperature that may be of interest in the study of quartz At high temperatures (low 10⁶/T²), calibrations based on experiments are in diagenesis. relatively good agreement (<1‰ above 400°C), however at low temperatures, there is large variability and extreme disagreement between the extrapolated lines (16% at 50°C). Care must be taken in choosing appropriate fractionation factors for studies at low temperatures. The letters outside the right-hand axis correspond to the lettered curves (C1=200-500°C from Clayton et al. (1972); M1=250-500°C from Matsuhisa et al. (1979); C2=500-750°C from Clayton et al. (1972); HC=400-750°C from Hu and Clayton (2003); M2=500-800°C from Matsuhisa et al. (1979); BJ=Bottinga and Javoy (1973); SK=Sharp and Kirschner (1994); SS=Shiro and Sakai (1972); Z=Zheng (1993); K1=2 term fit from Kawabe (1978); K2=3 term fit from Kawabe (1978)). SS, K1, K2 are based on reduced partition function ratios; Z is calculated by the increment method. Calibrations from Clayton et al. (1972) use recalculated values from Friedman and O'Neil (1977). There is excellent agreement between the two solution-A experiments of this study and the calibration of Sharp and Kirschner (1994).

Figure 4.9

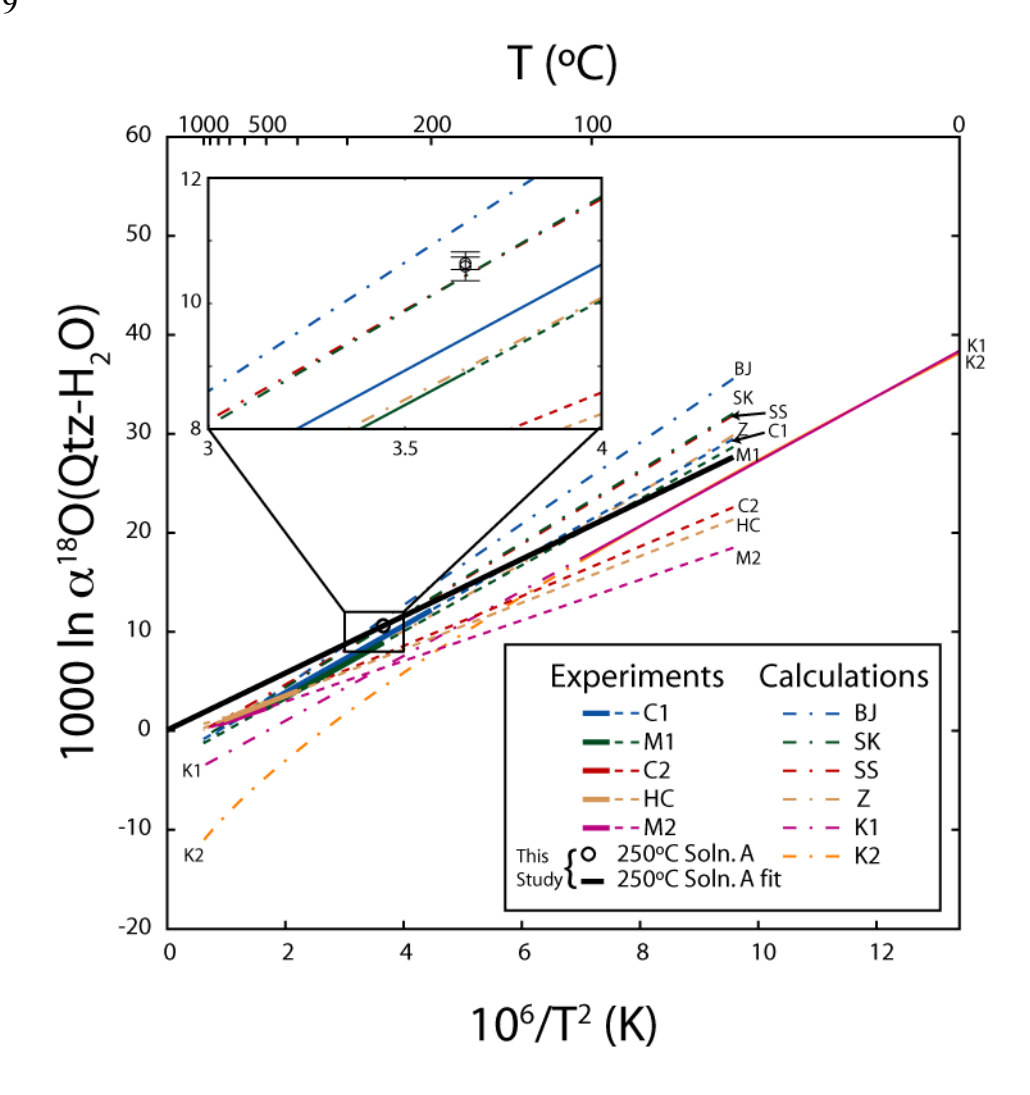
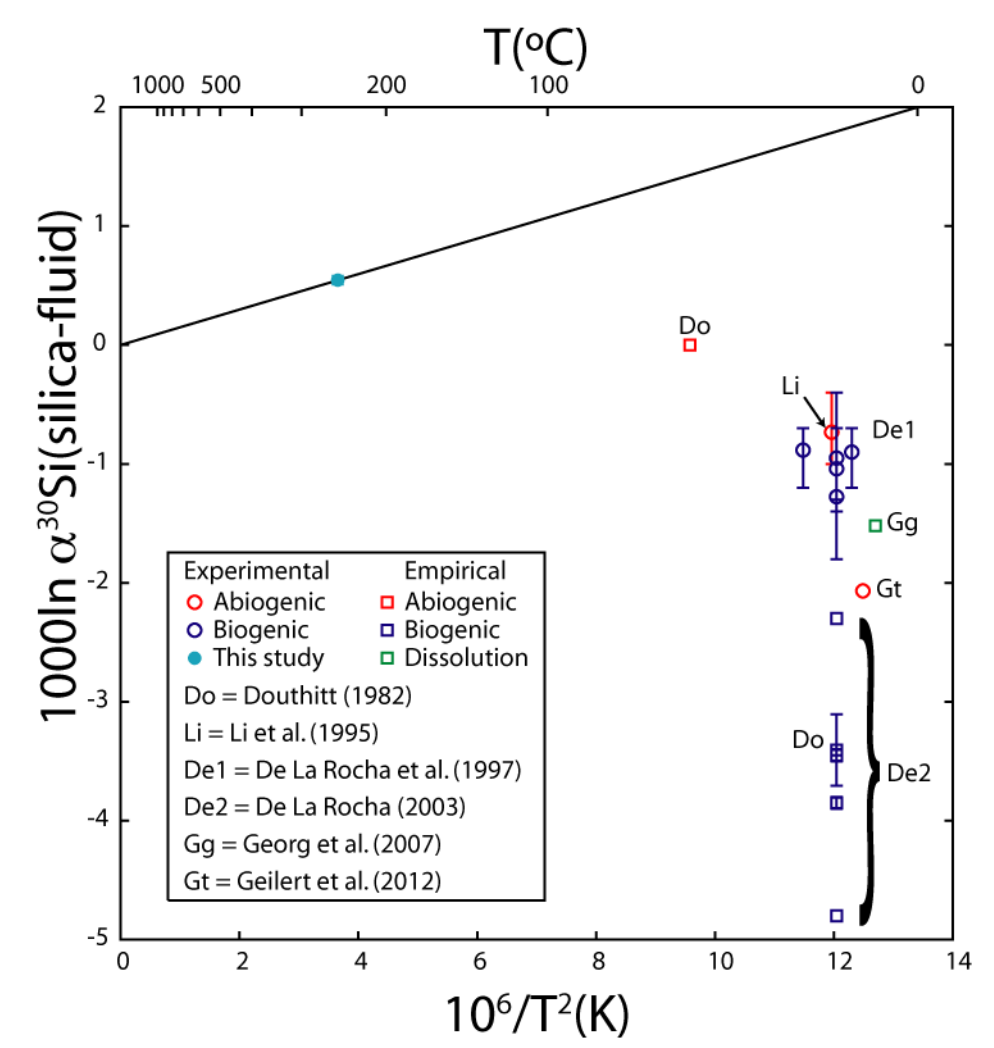


Figure 4.10. Comparison of estimates of silica-fluid silicon isotope fractionation factors at low temperatures. There is little agreement between the various values, many of which are empirical or for biogenic silica. See text for discussion of possible limitations of these data. Error bars represent the range of values measured in each study; range of 1000lnα³⁰si(Quartz-fluid) from this study is smaller than symbol. Black line is fit through experimental data of this study and 0‰ at infinite temperature (10⁶/T²=0). Abbreviations correspond to different studies (Do=Douthitt (1982); Li=Li et al. (1995); De1=De La Rocha et al. (1997); De2=De La Rocha (2003); Gg=Georg et al. (2007); Gt=Geilert et al. (2012)). All biogenic experimental data is based on cultured diatoms from De La Rocha et al. (1997), all biogenic empirical data is based on sponges from De La Rocha (2003) except one estimate from biogenic opal from Douthitt (1982).



Tables

Table 4.1A. Summary of quartz experiments at 250°C and starting materials.

Sample	Starting Solution	Days in furnace	Final solid after experiment	[Si] ppm [†]
Starting m	aterials			
SG-1*				
Soln. A	Ground glas	ss, NaOH, 1	NaCl	1768
Soln. B	Ground glas	ss, NaOH		
Soln. C	Concentrate	d sodium s	ilicate solution	1709
Experimen	its			
250-1	A	20	powder	
250-2	A	86	100 μm Qtz overgrowth; powder	1789
250-3	A	126	225 μm Qtz overgrowth; powder	1847
250-4	В	86	powder	
250-5	В	126	powder	
250-6	В	126	Analcime; powder	
250-7	C	22	1 μm Qtz overgrowth	
250-8	C	85	5 μm Qtz overgrowth	
250-9	С	126	8 μm Qtz overgrowth; doubly terminated Qtz (1-15 μm); Analcime	770

^{*}SG-1 is the ground silica glass for solutions A and B † Silicon concentration in solution measured by quadrupole ICP-MS. Values for experiments were measured after the experiments.

Table 4.1B. Oxygen isotope summary of quartz experiments at 250°C and starting materials. All quartz analyses are SIMS except powder $\delta^{18}O(Qtz)$

Sample	Powder δ ¹⁸ O(Qtz) ‰VSMOW [†]	Average SIMS δ ¹⁸ O(Qtz) ‰VSMOW	2SE SIMS δ ¹⁸ O(Qtz) ‰VSMOW	Average δ ¹⁸ O(H ₂ O) ‰VSMOW	2SD δ ¹⁸ O(H ₂ O) %•VSMOW [§]	Δ ¹⁸ O (Qtz- H ₂ O) ‰	2σ (Qtz- H ₂ O) ‰ [#]
G							
	materials						
SG-1*	9.94						
Soln. A				-7.02	0.20		
Soln. B							
Soln. C				-8.77	0.17		
Experim 250-1	nents						
250-2	7.34	4.27	0.06	-6.37	0.12	10.64	0.13
250-3	4.30	4.07	0.06	-6.52	0.22	10.59	0.23
250-4	5.11						
250-5	5.20						
250-6	29.68						
250-7							
250-8							
250-9				-8.48	0.17		

^{*}SG-1 is the ground silica glass for solutions A and B $^\dagger Precision$ on $\delta^{18}O$ powder analyses is \pm 0.22% 2SD based on 8 measurements of UWG-2 standard run at the same time as experimental powders

^{§2}SD on $\delta^{18}O(H_2O)$ is the higher of the analytical precision (0.12‰) or the 2SD based on replicate analyses of the given solution

 $^{^{\#}2\}sigma$ is calculated as $\sqrt{\left(2SE_{Qtz}\right)^{2}+\left(2SD_{H_{2}O}\right)^{2}}$

Table 4.1C. Silicon isotope summary of quartz experiments at 250°C and starting materials.

Sample	Average SIMS δ ³⁰ Si(Qtz) %NBS28	2SE SIMS δ ³⁰ Si(Qtz) %NBS28	Average δ ³⁰ Si(fluid) ‰NBS28	2SD δ ³⁰ Si(fluid) %NBS28	Δ ³⁰ Si (Qtz- fluid) ‰	2σ (Qtz- fluid) ‰#
	7001 \D 520	7001 \D 520			700	700
Starting	materials					
SG-1*						
Soln. A			0.06	0.10		
Soln. B						
Soln. C			0.27	0.10		
Experim	ents					
250-1						
250-2	0.21	0.14	-0.30	0.10	0.51	0.17
230 2	0.21	0.11	0.50	0.10	0.51	0.17
250-3	0.43	0.06	-0.15	0.10	0.58	0.12
250-4						
250-5						
250-6						
250-7						
250-8						
250-9			0.22	0.11		

^{*}SG-1 is the ground silica glass for solutions A and B $^{\#}2\sigma$ is calculated as $\sqrt{\left(2SE_{Qtz}\right)^{2}+\left(2SD_{H_{2}O}\right)^{2}}$

Table 4.2. $\delta^{18}O(H_2O)$ experimental products & starting fluids and standards measured by fluorination of water and by Finnigan/MAT251 at UW-Madison.

				_				0.18 0	0.18 0	δ ¹⁸ O
Analysis No.	Sample No.*	μl [†]	mm Hg	mmol CO ₂	mmol/ µl	% yield	$\delta^{13}C^{\S}$	δ ¹⁸ Ο (raw)	δ ¹⁸ Ο (VSMOW) [#]	(VSMOW -SLAP)**
FW-	110."	μι	ng	CO ₂	μι	76 yieiu	0 0	(raw)	(VSMOW)	-SLAF)***
120-1	UWDW-2	5	96.5	142.8	28.6	102.8	-27.71	-8.93	-9.08	-9.20
120-2	250-3	6	74.2	189.6	31.6	113.8	-27.72	-6.95	-7.10	-7.20
120-3	250-3	6	64.3	164.3	27.4	98.6	-27.68	-6.24	-6.39	-6.48
120-4	250-2	6	65.3	166.8	27.8	100.1	-27.70	-6.25	-6.40	-6.49
122-1	UWDW-2	5	96.9	143.4	28.7	103.3	-27.67	-8.88	-9.03	-9.15
122-2	250-2	6	66.5	169.9	28.3	102.0	-27.63	-6.19	-6.34	-6.43
122-3	A before	6	70.5	180.0	30.0	108.0	-27.70	-6.80	-6.95	-7.04
122-4	250-9	6	72.2	184.0	30.7	110.4	-27.71	-8.39	-8.54	-8.66
124-1	UWDW-2	5	96.3	142.5	28.5	102.6	-27.66	-9.03	-9.18	-9.30
124-2	250-3a	5	95.1	140.7	28.1	101.3	-27.69	-6.45	-6.60	-6.69
124-3	250-9	6	68.6	175.3	29.2	105.2	-27.67	-8.27	-8.42	-8.53
126-1	UWDW-2	5	93.1	137.8	27.6	99.2	-27.66	-8.90	-9.05	-9.17
126-2	250-3a	5	65.0	140.6	28.1	101.3	-27.69	-6.41	-6.56	-6.65
126-3	A after	6	107.8	159.5	26.6	95.7	-27.67	-6.94	-7.09	-7.19
126-4	C before	6	109.6	162.2	27.0	97.3	-27.68	-8.68	-8.83	-8.95
128-1	UWDW-2	5	96.5	142.8	28.6	102.8	-27.71	-8.95	-9.10	-9.22
128-2	C before	9		249.1	27.7	99.7	-27.58	-8.56	-8.71	-8.83
128-3	SMOW	5	94.3	139.6	27.9	100.5	-27.56	0.08	-0.07	-0.07
130-1	SMOW	5	93.8	138.8	27.8	100.0	-27.89	0.08	-0.07	-0.07
130-2	SMOW	5	93.4	138.2	27.6	99.5	-27.67	0.28	0.13	0.13
130-3 130-4	SLAP SLAP	5 5	97.1 95.5	143.7 141.3	28.7 28.3	103.5 101.8	-27.89 -27.85	-54.48 -54.73	-54.63 -54.88	-55.37 -55.63

^{*}Samples labeled before and after are starting solutions collected before and after placing material into reaction vessels. The time difference between the two is less than 15 minutes.

SMOW and SLAP samples were sealed in 5 μ l glass capillaries in 1994 and stored at UW-Madison. Measured values confirm that there was no exchange of these samples over the past 19 years.

Analysis FW-120-2 had an anomalously high yield and was not included in the calculation of average $\delta^{18}O(H_2O)$ for 250-3.

Precision is 0.12% 2SD based on measurements of the internal standard University of Wisconsin Distilled Water (UWDW-2) from each day of analysis (n=5, average = -8.94% raw)

 $^{^{\}dagger}$ Samples marked as 5 were 5 µl samples of fluid sealed in glass capillaries; other samples were 3 µl sealed in individual capillaries, which were then loaded together to yield enough oxygen to analyze.

 $^{^{\$}}$ Oxygen is reacted with a carbon rod and measured as CO_2 , $\delta^{13}C$ is simultaneously calculated for measured molecular ratios

 $^{^{\#}\}delta^{18}O(VSMOW)$ is calculated using the average raw value of +0.15 % for measured Standard Mean Ocean Water (SMOW) samples

^{**} δ^{18} O(VSMOW-SLAP) is calculated by multiplying the VSMOW value by (-55.5/-54.76). -54.76‰ is the average for the two Standard Light Antarctic Precipitation (SLAP) samples measured

Appendix A4

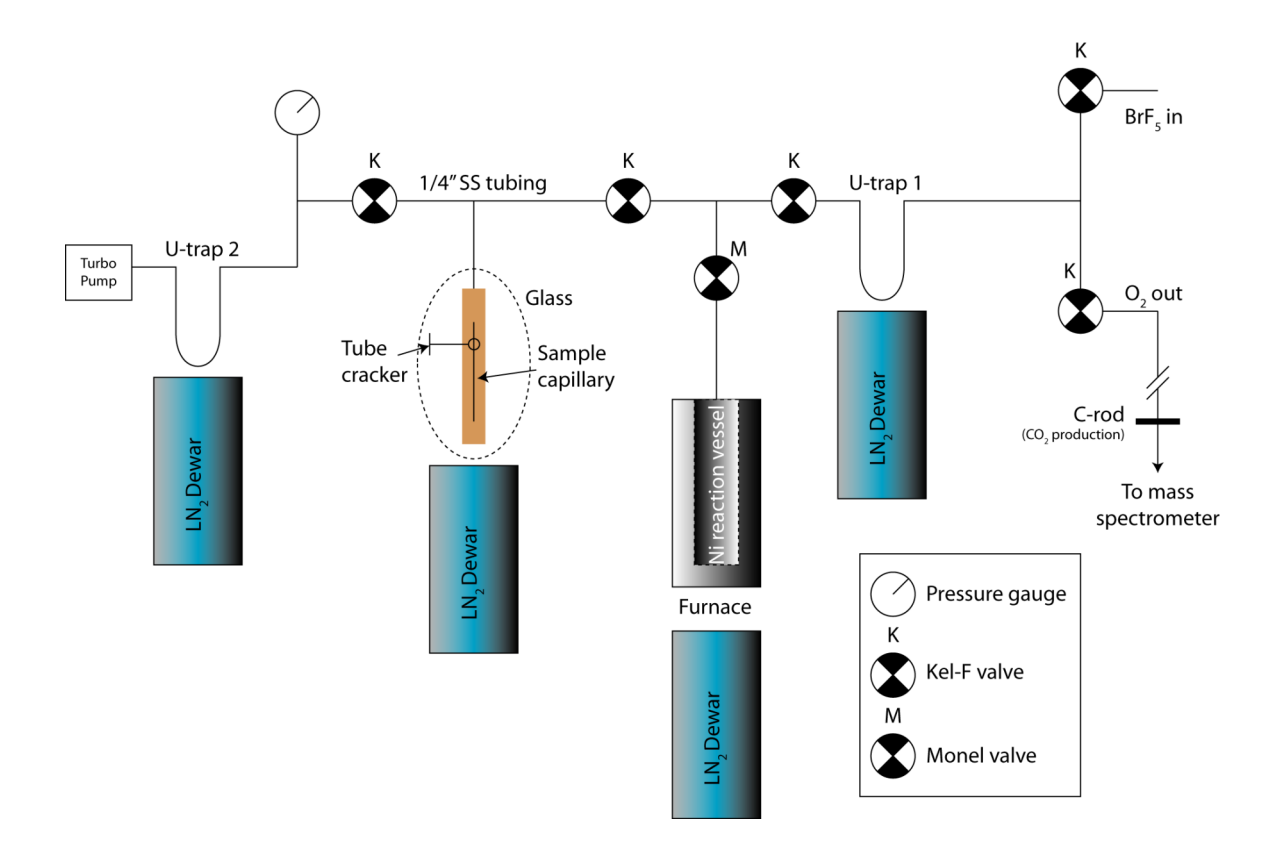
Water fluorination method

Water is sampled in 5 μ l glass capillary tubes, which are broken in an evacuated sample chamber. The water is then transferred to a nickel reaction vessel and reacted for 45 minutes at 230°C with bromine pentafluoride (BrF₅) to liberate oxygen (Fig. A4.1). The fluid is fully reacted by this method and all oxygen is recovered, converted to CO_2 and analyzed by gassource mass spectrometry. This method is modified by M. Spicuzza from a method developed by Kusakabe and Matsuhisa (2008) and is listed here as steps for analysis.

- 1) At beginning of day, heat and pump on Ni reaction vessel at 230°C and pump down sample capillary tube cracker
- 2) Close Ni reaction vessel valve; raise liquid nitrogen (LN₂) to shoulder of reaction vessel
- 3) Check line pressure with gauge
- 4) Isolate tube cracker, freeze bottom of tube cracker with LN₂, crack capillary
- 5) Open valves from tube cracker to Ni reaction vessel at LN₂ temperature, heat tube cracker, transfer fluid for 10 minutes, isolate Ni reaction vessel
- 6) Aliquot 1000 µmol BrF₅ to U-trap 1 and pump
- 7) Heat BrF₅ with heat gun, then quickly open and shut valve to LN₂ temperature Ni reaction vessel
- 8) Close valve on Ni reaction vessel
- 9) Heat with heat gun until hot to touch to remove frost from surface of reaction vessel
- 10) Place furnace at 230°C on Ni reaction vessel for 45 minutes
- Prepare to transfer to carbon rod, leave furnace on Ni reaction vessel, bleed O₂ sample slowly to carbon rod at ~650°C.
- 12) Transfer and analyze CO₂ by gas-source mass spectrometry
- 13) Pump on Ni reaction vessel for 45 minutes with rod furnace at 230°C in place
- 14) Repeat steps 2-13

Appendix Figure

Figure A4.1. Schematic diagram of water fluorination apparatus. O_2 out line is connected to the CO_2 production line of the Finnigan/MAT 251. The stainless steel tubing is wrapped with heat tape and kept at $\sim 60^{\circ}$ C to keep water from condensing on the tube interior during transfer. All valves are stainless steel bellows valves (Swagelok SS-4BKT) with Kel-F tips except the valve on the Ni reaction vessel, which is a stainless steel bellows valve (Swagelok SS-4BG) with a Monel tip.



Data repository (DR4)

Large data tables and figures for individual chapters are included in the supplementary files available with the online version of this dissertation.

Table DR4.1. Oxygen isotope data for experimentally grown quartz measured on the WiscSIMS ims-1280 ion microprobe.

Table DR4.2. Silicon isotope data for experimentally grown quartz measured on the WiscSIMS ims-1280 ion microprobe.

Sample Index

The natural samples described in this dissertation were donated by the Illinois State Geological Survey (ISGS), the Wisconsin Geological and Natural History Survey (WGNHS), the Midwest Geological Sequestration Consortium (MGSC), and R. Dott, Jr. (07WI-1) and collected by myself (all other Wisconsin outcrops). The experimental samples described in chapter 4 were precipitated in a laboratory at the Department of Geoscience. All specimens referenced in this thesis are in the collections of the Department of Geoscience, University of Wisconsin-Madison, under file number UW 2017 as defined in the table below. For the samples from ISGS, 1 cm³ blocks cast in epoxy are stored in the UW collection; the remainder of the sample was returned to ISGS.

UW Catalog number*	Published sample name	Sample type	Description	Location [†]	Latitude (N)	Longitude (W)	Described in
2017/1.1	09IL-1	1 cm ³ chip in epoxy	Quartz sandstone	12996	42.43731	-89.85786	Chapter 1, Chapter 2, Chapter 3
2017/1.1B	09IL-1	Back of 1 cm ³ chip in epoxy	Quartz sandstone	12996			
2017/2.1	09IL-2	1 cm ³ chip in epoxy	Quartz sandstone	12996	42.43731	-89.85786	Chapter 1, Chapter 2, Chapter 3
2017/2.1B	09IL-2	Back of 1 cm ³ chip in epoxy	Quartz sandstone	12996			
2017/3	09IL-3	Small slab	Quartz sandstone	12996	42.43731	-89.85786	
2017/4	09IL-4	Small slab	Quartz sandstone	12996	42.43731	-89.85786	
2017/5.1	09IL-5	1 cm ³ chip in epoxy	Quartz sandstone	12996	42.43731	-89.85786	Chapter 1, Chapter 2, Chapter 3
2017/5.1B	09IL-5	Back of 1 cm ³ chip in epoxy	Quartz sandstone	12996			
2017/6.1	09IL-6	1 cm ³ chip in epoxy	Quartz sandstone	12996	42.43731	-89.85786	Chapter 1, Chapter 2, Chapter 3
2017/6.1B	09IL-6	Back of 1 cm ³ chip in epoxy	Quartz sandstone	12996			
2017/7	09IL-7	Small slab	Quartz sandstone	12996	42.43731	-89.85786	
2017/8	09IL-8	Small slab	Quartz sandstone	12996	42.43731	-89.85786	
2017/9.1	09IL-9	1 cm ³ chip in epoxy	Quartz sandstone	12996	42.43731	-89.85786	Chapter 1, Chapter 2, Chapter 3

UW Catalog number*	Published sample name	Sample type	Description	Location [†]	Latitude (N)	Longitude (W)	Described in
2017/9.1B	09IL-9	Back of 1 cm ³ chip in epoxy	Quartz sandstone	12996			
2017/10	09IL-10	Small slab	Quartz sandstone	12996	42.43731	-89.85786	
2017/11.1	09IL-11	1 cm ³ chip in epoxy	Quartz sandstone	12996	42.43731	-89.85786	Chapter 1, Chapter 2, Chapter 3
2017/11.1B	09IL-11	Back of 1 cm ³ chip in epoxy	Quartz sandstone	12996			
2017/12	09IL-12	Small slab	Quartz sandstone	12996	42.43731	-89.85786	
2017/13.1	09IL-13	1 cm ³ chip in epoxy	Quartz sandstone	12996	42.43731	-89.85786	Chapter 1, Chapter 2, Chapter 3
2017/13.1B	3 09IL-13	Back of 1 cm ³ chip in epoxy	Quartz sandstone	12996			
2017/14	09IL-14	Small slab	Quartz sandstone	12996	42.43731	-89.85786	
2017/15.1	09IL-15	1 cm ³ chip in epoxy	Quartz sandstone	12996	42.43731	-89.85786	Chapter 1, Chapter 2, Chapter 3
2017/15.1B	09IL-15	Back of 1 cm ³ chip in epoxy	Quartz sandstone	12996			
2017/16.1	09IL-16	1 cm ³ chip in epoxy	Quartz sandstone	12996	42.43731	-89.85786	Chapter 1, Chapter 2, Chapter 3
2017/16.1B	09IL-16	Back of 1 cm ³ chip in epoxy	Quartz sandstone	12996			
2017/17	09IL-17	Small slab	Quartz sandstone	12996	42.43731	-89.85786	
2017/18	09IL-18	Small slab	Quartz sandstone	12996	42.43731	-89.85786	
2017/19.1	09IL-19	1 cm ³ chip in epoxy	Quartz sandstone	12996	42.43731	-89.85786	Chapter 1, Chapter 2, Chapter 3
2017/19.1B		Back of 1 cm ³ chip in epoxy	Quartz sandstone	12996			
2017/20	09IL-20	Small slab	Quartz sandstone	12996	42.43731	-89.85786	
2017/21.1	09IL-21	1 cm ³ chip in epoxy	Quartz sandstone	12996	42.43731	-89.85786	Chapter 1, Chapter 2, Chapter 3
2017/21.1B	8 09IL-21	Back of 1 cm ³ chip in epoxy	Quartz sandstone	12996			
2017/22	09IL-22	Small slab	Quartz sandstone	12996	42.43731	-89.85786	
2017/23	09IL-23	Small slab	Quartz sandstone	12996	42.43731	-89.85786	
2017/24.1	09IL-24	1 cm ³ chip in epoxy	Quartz sandstone	12996	42.43731	-89.85786	Chapter 1, Chapter 2, Chapter 3
2017/24.1B	3 09IL-24	Back of 1 cm ³ chip in epoxy	Quartz sandstone	12996			
2017/25	09IL-25	Small slab	Quartz sandstone	12996	42.43731	-89.85786	
2017/26.1	09IL-26	1 cm ³ chip in epoxy	Quartz sandstone	12996	42.43731	-89.85786	Chapter 1, Chapter 2, Chapter 3
2017/26.1B	3 09IL-26	Back of 1 cm ³ chip in epoxy	Quartz sandstone	12996			

UW Catalog number*	Published sample name	Sample type	Description	Location [†]	Latitude (N)	Longitude (W)	Described in
2017/27.1	09IL-27	1 cm ³ chip in epoxy	Quartz sandstone	12996	42.43731	-89.85786	Chapter 1, Chapter 2, Chapter 3
2017/27.1E	3 09IL-27	Back of 1 cm ³ chip in epoxy	Quartz sandstone	12996			
2017/28.1	09IL-28	1 cm ³ chip in epoxy	Quartz sandstone	12996	42.43731	-89.85786	Chapter 1, Chapter 2, Chapter 3
2017/28.1E	3 09IL-28	Back of 1 cm ³ chip in epoxy	Quartz sandstone	12996			
2017/29.1	09IL-29	1 cm ³ chip in epoxy	Quartz sandstone	12996	42.43731	-89.85786	Chapter 1, Chapter 2, Chapter 3
2017/29.1E	3 09IL-29	Back of 1 cm ³ chip in epoxy	Quartz sandstone	12996			
2017/30	09IL-30	Small slab	Granite	12996	42.43731	-89.85786	
2017/31.1	09IL-31	1 cm ³ chip in epoxy	Quartz sandstone	13639	40.12710	-87.55958	Chapter 1, Chapter 2, Chapter 3
2017/31.1E	3 09IL-31	Back of 1 cm ³ chip in epoxy	Quartz sandstone	13639			
2017/32	09IL-32	Small slab	Quartz sandstone	13639	40.12710	-87.55958	
2017/33.1	09IL-33	1 cm ³ chip in epoxy	Quartz sandstone	13639	40.12710	-87.55958	Chapter 1, Chapter 2, Chapter 3
2017/33.1E	3 09IL-33	Back of 1 cm ³ chip in epoxy	Quartz sandstone	13639			
2017/34.1	09IL-34	1 cm ³ chip in epoxy	Quartz sandstone	13639	40.12710	-87.55958	Chapter 1, Chapter 2, Chapter 3
2017/34.1E	3 09IL-34	Back of 1 cm ³ chip in epoxy	Quartz sandstone	13639			
2017/35.1	09IL-35	1 cm ³ chip in epoxy	Quartz sandstone	13639	40.12710	-87.55958	Chapter 1, Chapter 2, Chapter 3
2017/35.1E	3 09IL-35	Back of 1 cm ³ chip in epoxy	Quartz sandstone	13639			
2017/36	09IL-36	Small slab	Quartz sandstone	13639	40.12710	-87.55958	
2017/37.1	09IL-37	1 cm ³ chip in epoxy	Quartz sandstone	13639	40.12710	-87.55958	Chapter 1, Chapter 2, Chapter 3
2017/37.1E	3 09IL-37	Back of 1 cm ³ chip in epoxy	Quartz sandstone	13639			
2017/38.1	09IL-38	1 cm ³ chip in epoxy	Quartz sandstone	13639	40.12710	-87.55958	Chapter 1, Chapter 2, Chapter 3
2017/38.1E	3 09IL-38	Back of 1 cm ³ chip in epoxy	Quartz sandstone	13639			
2017/39.1	09IL-39	1 cm ³ chip in epoxy	Quartz sandstone	13639	40.12710	-87.55958	Chapter 1, Chapter 2, Chapter 3
2017/39.1E	3 09IL-39	Back of 1 cm ³ chip in epoxy	Quartz sandstone	13639			
2017/40	09IL-40	Small slab	Quartz sandstone	13639	40.12710	-87.55958	
2017/41.1	09IL-41	1 cm ³ chip in epoxy	Quartz sandstone	13639	40.12710	-87.55958	Chapter 1, Chapter 2, Chapter 3

UW Catalog number*	Published sample name	Sample type	Description	Location [†]	Latitude (N)	Longitude (W)	Described in
2017/41.1B		Back of 1 cm ³ chip in epoxy	Quartz sandstone	13639			
2017/42	09IL-42	Small slab	Quartz sandstone	4831	38.55216	-89.02246	
2017/43	09IL-43	Small slab	Quartz sandstone	4831	38.55216	-89.02246	
2017/44	09IL-44	Small slab	Quartz sandstone	4831	38.55216	-89.02246	
2017/45	09IL-45	Small slab	Quartz sandstone	4831	38.55216	-89.02246	
2017/46.1	09IL-46	1 cm ³ chip in epoxy	Quartz sandstone	4831	38.55216	-89.02246	Chapter 1, Chapter 2, Chapter 3
2017/46.1B	3 09IL-46	Back of 1 cm ³ chip in epoxy	Quartz sandstone	4831			
2017/47.1	09IL-47	1 cm ³ chip in epoxy	Quartz sandstone	4831	38.55216	-89.02246	Chapter 1, Chapter 2, Chapter 3
2017/47.1B	3 09IL-47	Back of 1 cm ³ chip in epoxy	Quartz sandstone	4831			
2017/48.1	09IL-48	1 cm ³ chip in epoxy	Quartz sandstone	4831	38.55216	-89.02246	Chapter 1, Chapter 2, Chapter 3
2017/48.1B	3 09IL-48	Back of 1 cm ³ chip in epoxy	Quartz sandstone	4831			
2017/49	09IL-49	Small slab	Quartz sandstone	4831	38.55216	-89.02246	
2017/50.1	09IL-50	1 cm ³ chip in epoxy	Quartz sandstone	4831	38.55216	-89.02246	Chapter 1, Chapter 2, Chapter 3
2017/50.1B	8 09IL-50	Back of 1 cm ³ chip in epoxy	Quartz sandstone	4831			
2017/51.1	09WI-1	Hand Sample	Phyllite	Outcrop	44.35807	-90.79263	Chapter 3
2017/51.2	09WI-1	Thin section Billet	Phyllite	Outcrop			
2017/51.3	09WI-1	Thin Section	Phyllite	Outcrop			
2017/52.1	09WI-2	Hand Sample	Quartz sandstone	Outcrop	44.35807	-90.79263	Chapter 3
2017/52.2	09WI-2	Thin section Billet	Quartz sandstone	Outcrop			
2017/52.3	09WI-2	Thin Section	Quartz sandstone	Outcrop			
2017/53.1	09WI-3	Hand Sample	Quartz sandstone	Outcrop	44.35807	-90.79263	Chapter 3
2017/53.2	09WI-3	Thin section Billet	Quartz sandstone	Outcrop			
2017/53.3	09WI-3	Thin Section	Quartz sandstone	Outcrop			
2017/54.1	09WI-4	Hand Sample	Quartz sandstone	Outcrop	44.35807	-90.79263	Chapter 3
2017/54.2	09WI-4	Thin section Billet	Quartz sandstone	Outcrop			
2017/54.3	09WI-4	Thin Section	Quartz sandstone	Outcrop			-
2017/55.1	09WI-5	Hand Sample	Quartz sandstone	Outcrop	44.71872	92.22078	Chapter 3

UW Catalog number*	Published sample name	Sample type	Description	Location [†]	Latitude (N)	Longitude (W)	Described in
2017/55.2	09WI-5	Thin section Billet	Quartz sandstone	Outcrop			
2017/55.3	09WI-5	Thin Section	Quartz sandstone	Outcrop			
2017/56.1	09WI-6	Hand Sample	Conglomerate	-	44.71880	92.22883	Chapter 3
2017/56.2	09WI-6 prl (Cut parallel to fractures)	Thin section Billet	Conglomerate	Outcrop			
2017/56.3	09WI-6 prl (Cut parallel to fractures)	Thin Section	Conglomerate	Outcrop			
2017/56.4	09WI-6 perp (Cut perpendicula to fractures)	Thin section r Billet	Conglomerate	Outcrop			
2017/56.5	09WI-6 perp		Conglomerate	Outcrop			
	(Cut perpendicula	Thin Section					
2017/57.1	to fractures) 09WI-7	Hand Sample	Quartz sandstone	Outcrop	44.71670	92.23108	Chapter 3
2017/57.2	09WI-7	Thin section Billet	Quartz sandstone	Outcrop			
2017/57.3	09WI-7	Thin Section	Quartz sandstone	Outcrop			
2017/58.1	09WI-9	Hand Sample	Quartz sandstone	Outcrop	44.71372	92.19815	Chapter 3
2017/58.2	09WI-9	Thin section Billet	Quartz sandstone	Outcrop			
2017/58.3	09WI-9	Thin Section	Quartz sandstone	Outcrop			
2017/59.1	09WI-10	Hand Sample	Quartz sandstone	Outcrop	44.55157	-90.65793	Chapter 3
2017/59.2	09WI-10	Thin section Billet	Quartz sandstone	Outcrop			
2017/59.3	09WI-10	Thin Section	Quartz sandstone	Outcrop			
2017/60.1	09WI-11	Hand Sample	Quartz sandstone	Outcrop	44.55157	-90.65793	Chapter 3
2017/60.2	09WI-11	Thin section Billet	Quartz sandstone	Outcrop			
2017/60.3	09WI-11	Thin Section	Quartz sandstone	Outcrop			
2017/61.1	09WI-12	Hand Sample	Quartz sandstone	Outcrop	44.55987	-90.61268	Chapter 3
2017/61.2	09WI-12	Thin section Billet	Quartz sandstone	Outcrop			
2017/61.3	09WI-12	Thin Section	Quartz sandstone	Outcrop			
2017/62.1	09WI-13	Hand Sample	Quartz sandstone	Outcrop	44.55987	-90.61268	Chapter 3
2017/62.2	09WI-13	Thin section Billet	Quartz sandstone	Outcrop			

UW Catalog number*	Published sample name	Sample type	Description	Location [†]	Latitude (N)	Longitude (W)	Described in
2017/62.3	09WI-13	Thin Section	Quartz sandstone	Outcrop			
2017/63.1	09WI-14	Hand Sample	Quartz sandstone	Outcrop	44.44943	-89.82738	Chapter 3
2017/63.2	09WI-14	1 cm ³ chip in epoxy	Quartz sandstone	Outcrop			
2017/63.3	09WI-14	Back of 1 cm ³ chip in epoxy	Quartz sandstone	Outcrop			
2017/64.1	09WI-15	Hand Sample	Quartz sandstone	Outcrop	44.44943	-89.82738	Chapter 3
2017/64.2	09WI-15	1 cm ³ chip in epoxy	Quartz sandstone	Outcrop			
2017/64.3	09WI-15	Back of 1 cm ³ chip in epoxy	Quartz sandstone	Outcrop			
2017/65.1	09WI-16	Hand Sample	Quartz sandstone	Outcrop	44.44943	-89.82738	Chapter 3
2017/65.2	09WI-16	Thin section Billet	Quartz sandstone	Outcrop			
2017/65.3	09WI-16	Thin Section	Quartz sandstone	Outcrop			
2017/66.1	09WI-17	Hand Sample	Quartz sandstone	Outcrop	44.47328	-89.64765	Chapter 3
2017/66.2	09WI-17	1 cm ³ chip in epoxy	Quartz sandstone	Outcrop			
2017/66.3	09WI-17	Back of 1 cm ³ chip in epoxy	Quartz sandstone	Outcrop			
2017/67.1	09WI-18	Hand Sample	Quartz sandstone	Outcrop	44.47328	-89.64765	Chapter 3
2017/67.2	09WI-18	1 cm ³ chip in epoxy	Quartz sandstone	Outcrop			
2017/67.3	09WI-18	Back of 1 cm ³ chip in epoxy	Quartz sandstone	Outcrop			
2017/68.1	09WI-19	Hand Sample	Quartz sandstone	Outcrop	43.93015	-89.80395	Chapter 3
2017/68.2	09WI-19	Thin section Billet	Quartz sandstone	Outcrop			
2017/68.3	09WI-19	Thin Section	Quartz sandstone	Outcrop			
2017/69.1	09WI-20	Hand Sample	Quartz sandstone	Outcrop	43.93015	-89.80395	Chapter 3
2017/69.2	09WI-20	Thin section Billet	Quartz sandstone	Outcrop			
2017/69.3	09WI-20	Thin Section	Quartz sandstone	Outcrop			
2017/70.1	09WI-21	Hand Sample	Quartz sandstone	Outcrop	43.93015	-89.80395	Chapter 3
2017/70.1	09WI-21	Thin section Billet	Quartz sandstone	Outcrop			
2017/70.1	09WI-21	Thin Section	Quartz sandstone	Outcrop			
2017/71.1	07WI-1	Hand Sample	Quartz sandstone	Outcrop	Near Steve	ens Point, WI	

UW Catalog number*	Published sample name	Sample type	Description	Location [†]	Latitude (N)	Longitude (W)	Described in
2017/71.2	07WI-1L (light banding)	Thin section Billet	Quartz sandstone	Outcrop			
2017/71.3	07WI-1L (light banding)	Thin Section	Quartz sandstone	Outcrop			
2017/71.4	07WI-1D (dark banding)	Thin section Billet	Quartz sandstone	Outcrop			
2017/71.5	07WI-1D (dark banding)	Thin Section	Quartz sandstone	Outcrop			
2017/72.1	1004.1	1 cm ³ chip in epoxy	Shale	12996	42.43731	-89.85786	Chapter 2
2017/72.1E	3 1004.1	Back of 1 cm ³ chip in epoxy	Shale	12996			
2017/73.1	1027.1	1 cm ³ chip in epoxy	Shale	12996	42.43731	-89.85786	Chapter 2
2017/73.1E		Back of 1 cm ³ chip in epoxy		12996			
2017/74.1	1040.5	1 cm ³ chip in epoxy	Shale	12996	42.43731	-89.85786	Chapter 2
2017/74.1E		Back of 1 cm ³ chip in epoxy		12996	42 42721	00.05707	Chautau 2
2017/75.1 2017/75.1E	1076.4	1 cm ³ chip in epoxy	Shale Shale	12996 12996	42.43731	-89.85786	Chapter 2
2017/76.1	1091	Back of 1 cm ³ chip in epoxy 1 cm ³ chip in	Shale	12996	42.43731	-89.85786	Chapter 2
2017/76.1E		epoxy Back of 1 cm ³		12996	12.13731	07.03700	Chapter 2
2017/77.1	1094	chip in epoxy 1 cm ³ chip in	Shale	12996	42.43731	-89.85786	Chapter 2
2017/77.1E	3 1094	epoxy Back of 1 cm ³	Shale	12996			
2017/78.1	1109.7	chip in epoxy 1 cm ³ chip in	Shale	12996	42.43731	-89.85786	Chapter 2
2017/78.1E	B 1109.7	epoxy Back of 1 cm ³	Shale	12996			
2017/79.1	1131.5	chip in epoxy 1 cm ³ chip in epoxy	Shale	12996	42.43731	-89.85786	Chapter 2
2017/79.1E	3 1131.5	Back of 1 cm ³ chip in epoxy	Shale	12996			
2017/80.1	1157	1 cm ³ chip in epoxy	Shale	12996	42.43731	-89.85786	Chapter 2
2017/80.1E	3 1157	Back of 1 cm ³ chip in epoxy	Shale	12996			
2017/81.1	1217.3	1 cm ³ chip in epoxy	Shale	12996	42.43731	-89.85786	Chapter 2

UW Catalog number*	Published sample name	Sample type	Description	Location [†]	Latitude (N)	Longitude (W)	Described in
2017/81.1B		Back of 1 cm ³ chip in epoxy	Shale	12996			
2017/82.1	1249.7	1 cm ³ chip in epoxy	Shale	12996	42.43731	-89.85786	Chapter 2
2017/82.1B	3 1249.7	Back of 1 cm ³ chip in epoxy	Shale	12996			
2017/83.1	1279	1 cm ³ chip in epoxy	Shale	12996	42.43731	-89.85786	Chapter 2
2017/83.1B	3 1279	Back of 1 cm ³ chip in epoxy	Shale	12996			
2017/84.1	3211	1 cm ³ chip in epoxy	Shale	4006	40.28181	-88.42741	Chapter 2
2017/84.1B	3 3211	Back of 1 cm ³ chip in epoxy	Shale	4006			
2017/85.1	3751-3801 #1	1 cm ³ chip in epoxy	Shale	4006	40.28181	-88.42741	Chapter 2
2017/85.1B	3 3751-3801 #1	Back of 1 cm ³ chip in epoxy	Shale	4006			
2017/86.1	3847	1 cm ³ chip in epoxy	Shale	4006	40.28181	-88.42741	Chapter 2
2017/86.1B	3 3847	Back of 1 cm ³ chip in epoxy	Shale	4006			
2017/87.1	3857	1 cm ³ chip in epoxy	Shale	4006	40.28181	-88.42741	Chapter 2
2017/87.1B		Back of 1 cm ³ chip in epoxy	Shale	4006			
2017/88.1	5476A	1 cm ³ chip in epoxy	Shale	ADM CCS1	39.87650	-88.89370	Chapter 2
2017/88.1B		Back of 1 cm ³ chip in epoxy	Shale	ADM CCS1			
	5476B	1 cm ³ chip in epoxy	Shale	ADM CCS1	39.87650	-88.89370	Chapter 2
2017/88.2B		Back of 1 cm ³ chip in epoxy		ADM CCS1	20.07420		
2017/89.1		1 cm ³ chip in epoxy	Quartz sandstone	ADM CCS1	39.87650	-88.89370	Chapter 2
2017/89.1B		Back of 1 cm ³ chip in epoxy	Quartz sandstone	ADM CCS1	20.07420		
2017/90.1	6765	1 cm ³ chip in epoxy	Quartz sandstone	ADM CCS1	39.87650	-88.89370	Chapter 2
2017/90.1B		Back of 1 cm ³ chip in epoxy	Quartz sandstone	ADM CCS1			
2017/91	277.9 A1	Thin Section	Shale	131467	43.03295	-89.36130	Chapter 2
2017/92 2017/93	277.9 B1 179.4	Thin Section Thin Section	Shale Shale	131467 131467	43.03295 43.03295	-89.36130 -89.36130	Chanter 2
2017/93	280.9	Thin Section	Shale	131467	43.03295	-89.36130	Chapter 2
2017/95	292.5 A1	Thin Section	Shale	131467	43.03295	-89.36130	Chapter 2

UW Catalog number*	Published sample name	Sample type	Description	Location [†]	Latitude (N)	Longitude (W)	Described in
2017/96.1	250-2	1 cm ³ chip in epoxy	Experimental quartz	Experimental product			Chapter 4
2017/96.2	250-2c	Powder in envelope	Experimental quartz	Experimental product			
2017/97.1	250-3	1 cm ³ chip in epoxy	Experimental quartz	Experimental product			Chapter 4
2017/97.2	250-3e	1 cm ³ chip in epoxy	Experimental quartz	Experimental product			
2017/97.3	250-3f	1 cm ³ chip in epoxy	Experimental quartz	Experimental product			
2017/97.4	250-3c	Powder in envelope	Experimental quartz	Experimental product			
2017/98.1	250-4	1 cm ³ chip in epoxy	Experimental quartz	Experimental product			Chapter 4
2017/98.2	250-4c	Powder in envelope	Experimental quartz	Experimental product			
2017/99.1	250-5	1 cm ³ chip in epoxy	Experimental quartz	Experimental product			Chapter 4
2017/99.2	250-5c	Powder in envelope	Experimental quartz	Experimental product			
2017/100.1	250-6	1 cm ³ chip in epoxy	Experimental quartz	Experimental product			Chapter 4
2017/100.2	250-6c	Powder in envelope	Experimental quartz	Experimental product			
2017/101.1	250-7	1 cm ³ chip in epoxy	Experimental quartz	Experimental product			Chapter 4
2017/101.2	250-7c	Powder in envelope	Experimental quartz	Experimental product			
2017/102.1	250-8	1 cm ³ chip in epoxy	Experimental quartz	Experimental product			Chapter 4
2017/102.2	250-8c	Powder in envelope	Experimental quartz	Experimental product			
2017/103.1	250-9	1 cm ³ chip in epoxy	Experimental quartz	Experimental product			Chapter 4
2017/103.2	250-9c	Powder in envelope	Experimental quartz	Experimental product			
2017/103.3	250-9 albite	Grains cast in epoxy	Experimental analcime	Experimental product			

^{*}Samples cast in epoxy were sawed so that the mount was 5 mm thick. The removed portions contain sample and are labeled with the suffix B in the UW catalog (e.g., 2017/1.1B).

[†]Samples from drill cores have core number listed. 12996, 13639, 4006, and 4831 are from ISGS. 131467 is from WGNHS. ADM CCS1 is from MGSC.